Interacting gases of ultracold polar molecules

Frauke Seeßelberg

München 2019

Interacting gases of ultracold polar molecules

Frauke Seeßelberg

Dissertation
an der Fakultät für Physik
der Ludwig–Maximilians–Universität
München

vorgelegt von
FRAUKE SEESSELBERG
aus Friedrichshafen

München, 11.02.2019

Erstgutachter: Prof. Dr. Immanuel Bloch
Zweitgutachter: Prof. Dr. Silke Ospelkaus
Tag der mündlichen Prüfung: 25.03.2019

Zusammenfassung

Ultrakalte Quantengase sind wandlungsfähige Modellsysteme zur Erforschung der Quantenphysik oder für die Simulation von Festkörpereigenschaften. Es gibt sie inzwischen aus den verschiedensten Atomen, von Alkalimetallen über Erdalkalis und seltene Erden. Erst in den letzten Jahren sind Quantengase aus verschiedenen polaren Molekülen hinzu gekommen. Die Erwartungen an Quantengase aus heteronuklearen Molekülen sind hoch: Mit Hilfe ihrer großen elektrischen Dipolmomente können diese Moleküle langreichweitig miteinander wechselwirken – nicht nur über Kontaktwechselwirkungen, wie die meisten Atome. Außerdem besitzen sie zusätzliche Vibrations- und Rotationsfreiheitsgrade, die neue Möglichkeiten für die Quantensimulation eröffnen.

Allerdings führen ebendiese Freiheitsgrade auch zu einige Herausforderungen. Sie erschweren beispielsweise die Herstellung des Quantengases, das im atomaren Fall in der Regel über eine Kombination von Laserkühlung und Verdampfungskühlen erzeugt werden kann. Moleküle haben aber zumeist keine geschlossenen Übergänge in ihren Spektren, die für das Laserkühlen nötig wären. Daher stellen wir unser molekulares Quantengas aus einer Mischung zweier ultrakalter atomarer Quantengase her.

Im Rahmen dieser Arbeit wurde dafür zunächst eine solche experimentelle Methoden für fermionische $^{23}Na^{40}K$-Moleküle entwickelt, die auf dem Zwei-Photonen-Prozess *Stimulated Raman Adiabatic Passage* (STIRAP) basiert. Die Hyperfeinstruktur des darin verwendeten Zwischenzustandes spielt dabei eine wichtige Rolle. Experimentell und mit Hilfe eines theoretischen Models, das den gesamten Prozess beschreibt, erkennen wir, dass wir die meisten Moleküle erzeugen können, wenn wir für den STIRAP eine große Ein-Photonen-Verstimmung wählen, sofern die Hyperfeinstruktur des Zwischenzustandes nicht aufgelöst ist.

In einem weiteren Projekt ging es um die Rotationsstruktur des durch den STIRAP bevölkerten Grundzustandes. Diese ist eng mit dem elektrischen Dipolmoment verknüpft. Insbesondere beinhaltet die Superposition des Grundzustandes mit dem ersten angeregten Rotationszustand ein Übergangsdipolmoment, das fast 60% des permanenten elektrischen Dipolmoments entspricht. Die Kohärenzzeit einer solchen Superposition ist allerdings kurz, da die unterschiedliche Polarisierbarkeiten der Rotationszustände zu Dephasierung in der optischen Falle führen. Mithilfe eines speziellen Polarisationswinkel und einem kleinen, statischen elektrischen Feld können wir diese Unterschiede ausgleichen und eine *Spin-entkoppelte magische Falle* realisieren. Wir messen mit dieser Technik einen neuen Kohärenzzeitrekord, allerdings nur für geringe Moleküldichten. Für größere Dichten beobachten wir erste Anzeichen für dipolare Wechselwirkungen in einem Gas polarer Moleküle, welche wir mithilfe der moving-average cluster expansion (MACE) auch modellieren.

Abstract

Ultracold quantum gases are versatile model systems for exploring quantum physics or for the simulation of solid state materials. Meanwhile, they have been created from various atomic species – from alkali metals over alkaline earths to rare earth elements. The latest addition are quantum gases of different kinds of polar molecules. Expectations for quantum gases of heteronuclear molecules are high: Due to their large electric dipole moments, these molecules can interact with each other via long-range interactions – not just via contact interactions as is the case for most atoms. Additionally, they have vibrational and rotational degrees of freedom, with open up new possibilities for quantum simulation.

But the same degrees of freedom also pose some challenges. For example, they make the preparation of the quantum gas more difficult, which is typically produced with a combination of laser cooling and evaporative cooling in the atomic case. Molecules mostly lack closed transitions in their spectra, which are required for laser cooling. Therefore, we create our molecular quantum gas from a mixture of two atomic quantum gases.

In this work, such an experimental method was developed for fermionic $^{23}Na^{40}K$ molecules, which is based on the two-photon process *Stimulated Raman Adiabatic Passage* (STIRAP). Within STIRAP, the hyperfine structure of the chosen intermediate state plays an important role. Experimentally, and with the help of a theoretical model describing the whole process, we find that we produce the most molecules when we use a large one-photon detuning, if the hyperfine structure of the intermediate state is unresolved.

In another project, we explored the rotational level structure of the molecular ground state populated by STIRAP. Rotation is closely linked to the electric dipole moment. The superposition of the ground state with the first excited rotational state, for example, has a transition dipole moment of almost 60% of the permanent electric dipole moment. Unfortunately, coherence times of such superpositions are typically short, as the different polarizabilities of the rotational states lead to dephasing in optical traps. However, using a special polarization angle and a small, dc electric field, we can compensate these differences and realize a *spin-decoupled magic trap*. With this new technique we obtain record coherence times, at least for small molecular densities. For larger densities we observe first indications for dipolar interactions in a bulk gas of polar molecules, which we also model using the moving-average cluster expansion (MACE).

Contents

On the one hand, molecules consisting of a small number of atoms represent the upper limit of complexity that we can hope at present to understand in complete detail, starting from quantum mechanics.
On the other hand, molecules are the building blocks from which more complex phenomena emerge, including chemistry, condensed matter, and life itself.

– J. Bohn, A. Rey, J. Ye

Chapter 1

Introduction

Ultracold quantum gases are an excellent experimental platform for realizing and observing quantum phenomena and are thus a rapidly growing field. After the first creation of Bose-Einstein Condensates (BEC) [1–3] for bosonic atoms and degenerate Fermi gases [4] for fermionic particles, many experimental tools and techniques have been developed to realize and study ever more complex quantum systems. Atoms with different level structures from alkali metals over alkaline earths or rare earths have been cooled to quantum degeneracy, which possess additional degrees of freedom, narrow linewidth transitions that can be utilized in atomic clocks, or magnetic dipole moments. In order to simulate models from solid state physics, ultracold atoms can be trapped in optical lattices [5], starting from simple cubic over hexagonal to quasi-crystalline structures [6] or superlattices, e.g. of double well structures. Imaging methods have been developed to study such gases to the single atom limit [7], even with the additional capability to record the spin-degree of freedom [8].

In the more recent years, people have also started to explore systems, that allow physics beyond the short-range contact interactions that so far governed the behavior of atoms in ultracold quantum gases, e.g. by implementing dipolar interactions. These ultracold dipolar gases promise exciting new opportunities for the research on ultracold quantum gases. Dipole-dipole interactions are long-range and anisotropic interactions. This gives rise to novel many-body physics ranging from rotons [9, 10] in systems with weak dipolar interactions to quantum droplets [11, 12], dipolar crystals, supersolids, and fractional Mott insulators [13], when the dipolar interaction dominates over the contact interaction. Also interesting are spin dynamics and quantum magnetism with dipolar interactions in optical lattices, for which new phases and bahviours are expected, compared to short-range interacting gases [14].

Systems exhibiting dipolar interactions include quantum gases of atoms with a magnetic dipole moment [15–17], ensembles of highly excited Rydberg atoms [18, 19] or of ultracold atoms inside cavities [20], and polar molecules [21–26]. Compared to these other systems, ultracold polar molecules feature strong, tunable dipole-dipole interactions as well as long single particle lifetimes [27, 28]. They possess many degrees of freedom, that can be manipulated by the researcher [29–33] and thus can

be used in quantum simulations. For example, nuclear spin states in the rovibronic ground state promise exciting possibilities for quantum computation [34] due to their extremely long coherence times [35]. In particular, interacting particles with long coherence times, e.g. superpositions of the rotational ground and and first excited state [36], are a key ingredient for entanglement generation and quantum engineering. Polar molecules are further an ideal platform to study ultracold chemistry and dipolar collisions [37, 38]. Also, first results towards quantum simulation using polar molecules in optical lattices [39, 40] or tweezer arrays [41] have been obtained, and the first quantum denegerate molecular gas [42] has been realized.

There has been impressive progress on cooling molecules down to cold and ultracold temperaturs recently [43–46]. In this thesis, however, we focus on the bottom-up approach, in which the ultracold molecular gas is assembled from two ultracold quantum gases of different species. Until today, this method allows to create the highest phase-space density molecular gases.

The bottom-up creation of a high phase-space density gas of polar molecules, proposed in [47], builds on two important previous achievements. The first was the creation of weakly bound Feshbach molecules, which will be discussed more in Chapter 2. The first homonuclear ones were created in 2002/2003 [48], heteronuclear molecules followed a few years later. The second is the application of the coherent two-photon process STIRAP [49, 50] in transferring such non-polar, heteronuclear molecules, predominantly of triplet spin-character, to the singlet electronic ground state in 2008 - first to an vibrationally excited state [51] and a few months later all the way to the singlet rovibronic ground state [21] - where a large permanent electric dipole moment can be induced. Earlier, in 2005, ultracold ground state polar molecules had been produced starting from an unbound quantum gas mixture and using a two-photon photoassociation scheme [52]. Compared to this, the new approach has several advantages: Starting out with Feshbach molecules enhances the wavefunction overlap for the pump transition to the intermediate state. Thus, less laser power is required to obtain the same coupling strength, which reduces the addressing of unwanted loss channels. Further, employing a coherent two-photon process and starting from a well defined initial state allows to populate only a single quantum state instead of several as in schemes relying on spontaneous emission, like photoassociation.

Ten years after the first experiments in dipolar KRb [21], this approach has been applied successfully to other dipolar molecules. LiNa [53] has been prepared in its triplet ground state and RbCs [22, 23], NaK [24, 26, 54] and NaRb [25] molecules are now readily available in the singlet ground state, with many more species on the way.

The first part of this thesis completes the experimental journey towards reaching the ground state of ^{23}Na^{40}K, that beginnings of which have been outlined in previous theses of the lab [55, 56]. In a second part, we use the rotational degree of freedom of

our molecules to induce strong, long-range and dipolar interactions in the quantum gas.

1.1 Outline of this Thesis

We begin with taking a close look at the electronic, vibrational, rotational and hyperfine level structure of heteronuclear diatomic molecules in Chapter 2, focusing on the example of $^{23}Na^{40}K$. In Chapter 3, the Polar Molecules Machine is introduced, the setup on which the experimental work discussed in this thesis has been carried out. Here we focus on new features of the apparatus, such as the narrow-linewidth dye laser system for molecule production, the high-voltage electric field setup for the dc polarization of the molecules and the microwave setup for rotational spectroscopy. Chapter 4 describes the first experimental result of the setup, the production of ultracold, fermionic ground-state molecules of $^{23}Na^{40}K$ using the two-photon process Stimulated Raman Adiabatic Passage (STIRAP). In addition to the experimental observations, we also provide a theoretical model for STIRAP, where an intermediate state with unresolved hyperfine structure is used. In Chapter 5, the first experiments exploring the rotational level structure are performed on the ground state molecules. The rotational degree of freedom is directly linked to the electric dipole moment and therefore, long rotational coherence is desired. We implement a novel spin-decoupled magic trapping technique, which allows us to extend the rotational coherence by an order of magnitude by using a small electric field and a suitable trap light polarization. We carefully characterize the rotational coherence in Chapter 6 using Ramsey- and spin-echo spectroscopy. Interestingly, we find a density dependence. We attribute it to the dipolar interaction due to the transition dipole moment of the rotational superposition and verify this with a simple moving-average cluster expansion (MACE) model.

1.2 List of Publications

The following articles have been published in refereed journals in the context of this thesis:

Modeling the adiabatic creation of ultracold polar $^{23}Na^{40}K$ molecules
F. Seeßelberg, N. Buchheim, Z.-K. Lu, T. Schneider, X.-Y. Luo, E. Tiemann, I. Bloch, C. Gohle
Phys. Rev. A 97, 013405 (2018)

Extending Rotational Coherence of Interacting Polar Molecules in a Spin-Decoupled Magic Trap
F. Seeßelberg, X.-Y. Luo, M. Li, R. Bause, S. Kotochigova, I. Bloch, C. Gohle
Phys. Rev. Lett. 121, 253401 (2018)

The following article has appeared in the Proceedings of the International School of Physics “Enrico Fermi" as summary of my science slam during the school:

Happy together: A molecular dating agency
F. Seeßelberg
Course 198 - Quantum simulators (2018)
Edited by T. Calarco, R. Fazio and P. Mataloni

Chapter 2

Heteronuclear Diatomic Molecules

Molecular structure gives raise to the sought-after electric dipole moment and the resulting anisotropic long-range interactions. But, due to its complexity, it also leads to challenges on the way to a long-range interacting, ultracold quantum gas. In this chapter, the relevant parts of the molecular structure for producing and working with diatomic molecules are highlighted. First, the general hierarchy of the electronic, vibrational, rotational and hyperfine structure of bi-alkaline polar molecules is introduced in Section 2.1. In Section 2.2, I focus on the properties of ^{23}Na^{40}K, the polar molecule we produce and experiment with in the laboratory. A discussion of various possibilities to polarize polar molecules concludes this chapter in Section 2.3.

2.1 Molecular Degrees of Freedom

Molecules have electronic and nuclear degrees of freedom, just as atoms do, and additionally vibrational and rotational ones. In general, all of these momenta can couple to each other and give rise to a rich molecular level structure. External fields further modify the level structure via Stark and Zeeman shifts. However, equipped with a good understanding of the molecular structure, full control over all degrees of freedom in polar molecules is possible and has been achieved. Sometimes, this even allows to mitigate or manipulate unwanted couplings, see Chapter 5.

In the following, I will briefly describe the key points of the molecular structure. If desired, find my more detailed summary in [57], or an extensive discussion in [58].

Each degree of freedom in molecules is associated with a typical energy scale. The electronic structure is the largest with optical transition frequencies, followed by vibration in the infra-red, rotation in the microwave regime and hyperfine structure on the kHz-level, see Fig. 2.1. All these degrees of freedom are already available for the simplest class of molecules, diatomic molecules. Heteronuclear diatomic molecules are the simplest molecules with a permanent electric dipole moment and therefore exhibit the desired long-range dipole-dipole interactions. In particular, we study bi-alkaline heteronuclear molecules that consist of two different alkali metal atoms. Al-

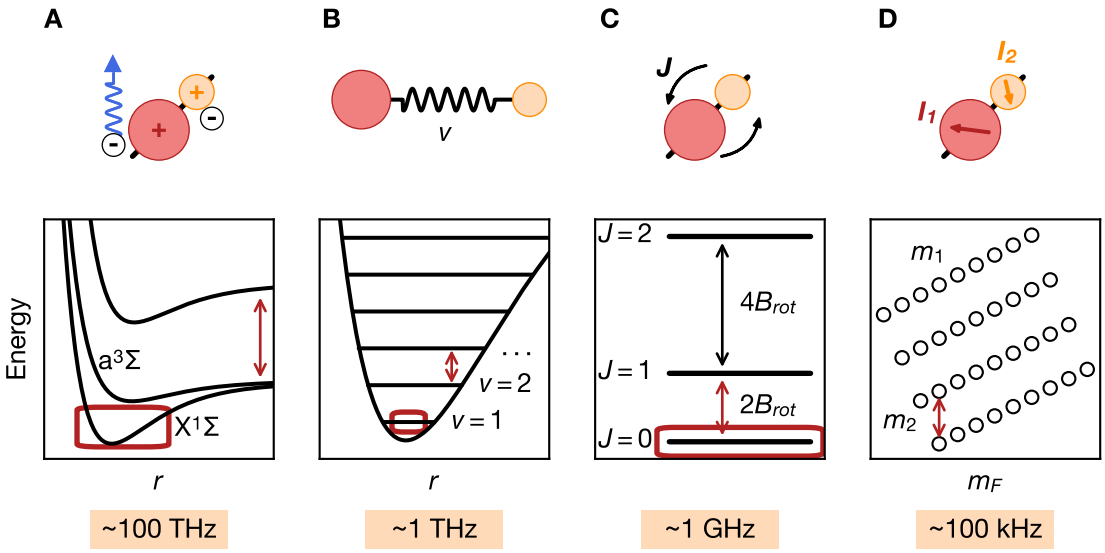

Figure 2.1: *Molecular structure of a bi-alkaline molecule reaching from several hundreds of THz to kHz. The corresponding transition energy scale for each structure is indicated by a red arrow and specified at the bottom of the plots. The electronic structure (**A**), consisting of singlet and triplet potentials, has the largest energy scale. Zooming in on the electronic, singlet ground state reveals the next-largest vibrational structure (**B**). On an even smaller energy scale, the rotation of the molecules becomes relevant (**C**). But an even smaller energy scale exists, the hyperfine structure (**D**). Note, that if not in the rovibronic groundstate, vibration, rotation and hyperfine structure generally cross-couple. This leads to the necessity of a magic trap, as will be discussed in chapter 5.*

kali metal atoms have been extremely well explored in recent years in the context of ultracold quantum gases, which makes is feasible to go one step further and combine two of them into a polar molecule.

The inner shells of electrons of the parent atoms remain largely undisturbed in a molecular binding. Therefore it is sufficient to consider only the two outer *valence* electrons that mediate the molecular binding, and the nuclei with their filled shells. Further, because the mass of the nuclei is many orders of magnitude larger than that of the electrons, their motion can be treated separately. This is the *Born-Oppenheimer approximation* [58]. The Hamiltonian of a diatomic molecule can then be expressed as

$$\mathcal{H} = T_N + T_e + V, \tag{2.1}$$

where T denotes the kinetic energy operators for nuclei (N) or electrons (e), respectively, and V is the potential energy of the system. The potential energy is given by

the sum of Coulomb interactions between the two electrons, the two nuclei or electrons and nuclei. Then, the electronic wave functions Φ_q, where q denotes an electronic state, can be obtained by solving the time-independent Schrödinger equation using only the electronic part of the Hamiltonian of Eq. 2.1. The total molecular wave function Ψ can then be expanded in terms of Φ_q, where the expansion coefficients F_q are wave functions that represent nuclear motion, i. e. rotation and vibration. It is convenient to treat the problem in polar coordinates with polar angles θ and ϕ and internuclear distance R. The Born-Oppenheimer approximation now consists of using that Φ_q varies only slowly with R, θ and ϕ, so that derivatives with respect to these quantities can be neglected. This allows to uncouple the Schrödinger equations and write them as

$$\left[-\frac{\hbar^2}{2\mu}\frac{1}{R^2}\frac{\partial}{\partial R}\left(R^2\frac{\partial}{\partial R}\right)+\frac{\langle\Phi_s|\,\mathbf{N}^2\,|\Phi_s\rangle}{2\mu R^2}+E_s(R)-E\right]F_s(\mathbf{R})=0, \tag{2.2}$$

where μ is the reduced mass of the nuclei, $E_s(R)$ is the eigenvalue of the electronic wave equation of electronic state $q = s$, and $\mathbf{N}^2$ is the orbital angular momentum operator for the relative angular motion of the nuclei. These are the nuclear wave equations, E denotes the corresponding eigenvalue.

Note, how $E_s(R)$ acts as a potential in the nuclear wave equations. A typical form of $E_s(R)$ is shown in Fig. 2.1 (A): If R is very large, the atoms essentially behave like free atoms and their potential energy is constant, the sum of the energies of the individual atoms. If, however, R becomes very small, the repulsive Coulomb force dominates the potential. In between these two extremes, molecular bound states can exist. Transitions between different electronic states occur in the visible or UV-range of the electromagnetic spectrum and constitute the largest energy scale in molecules. In the special case of bi-alkaline molecules, all electronic potentials are either singlet or triplet potentials. To label these potentials, a similar nomenclature as in atoms is used, the molecular term symbol $^{2\Sigma+1}\Lambda$. Here, Σ denotes the total spin of the molecule and Λ is the electronic, orbital angular momentum quantum number. In front of this term symbol, a letter is used to further distinguish states with the same term symbol. The absolute ground state is traditionally denoted as $X^1\Sigma$. Excited states with the same multiplicity as the ground state are labeled with capital letters $A, B, C, ...$, while states with a different multiplicity are labeled with lower case letters a,b,c and so forth. However, this notation is just one convention in the literature. Sometimes, numbers are used instead of letters, referring to the number of states with the same term symbol counting from the lowest potentials.

Each electronic potential energy curve is inhabited by a number of vibrational states, the next largest energy scale, see Fig. 2.1 (B). Molecular vibration is well approximated by treating it classically, assuming that the parent atoms are connected

through a spring with spring constant k_s. Close to the bottom of an electronic potential, it is valid to make a harmonic approximation. The energy of the vibrational states can then be written as

$$E_v = \left(v + \frac{1}{2}\right)\hbar\omega, \tag{2.3}$$

where v denotes the vibrational quantum number and ω is related to the spring constant k_s as

$$\omega = \sqrt{\frac{k}{\mu}}. \tag{2.4}$$

The spring constant, on the other hand, depends on the electronic potential E_s as

$$k_s = \left.\frac{\mathrm{d}^2 E_s(R)}{\mathrm{d}R^2}\right|_{R=R_0}, \tag{2.5}$$

where R_0 denotes position of the minimum of the potential s. Transitions between vibrational states of the same electronic potential may change v by $|\Delta v| = 1$ and are in the infra-red range [58]. If the electronic state is changed as well, there are no selection rules on Δv.

Zooming in on one vibrational state, e.g. the vibrational ground state of the $X^1\Sigma$-potential reveals the next smaller rotational structure. When we approximate the molecule as a rigid rotor, the rotational energy is given in terms of the rotational quantum number J as

$$E_r = B_{\mathrm{rot}} J(J+1) = \frac{\hbar^2}{2I} J(J+1), \tag{2.6}$$

B_0 is called *rotational constant* and is given as $B_{\mathrm{rot}} = \hbar^2/(2\mu R_0^2)$. Therefore it also depends on the specific electronic state s. The rotational constant is typically on the order of GHz and the condition $\Delta J = 0, \pm 1$ has to be fulfilled in any molecular transition.

As we will see in chapter 4 we are able to resolve an even smaller energy scale than rotation in the electronic, vibrational and rotational (rovibronic) ground state: hyperfine structure. The energy spacing between neighboring hyperfine levels is on the 10 kHz level. It is given as [26, 55]

$$\mathcal{H}_{hf} = (\mu_A \mathbf{I_A} + \mu_B \mathbf{I_B})\mathbf{B} + c_4 \mathbf{I_A} \mathbf{I_B}, \tag{2.7}$$

where μ_A (μ_B) denote the magnetic moments and $\mathbf{I_A}$ ($\mathbf{I_B}$) are the nuclear spins of the parent atoms A and B, respectively. The coefficient c_4 denotes the scalar spin-spin interaction constant.

With this hierarchy of molecular energy scales in mind we can now turn to the specific case of ^{23}Na^{40}K molecules.

2.2 Important States in NaK

In this work we study the ultracold, heteronuclear and bi-alkaline $^{23}Na^{40}K$ molecule, see Fig. 2.2. Due to the complexity of the molecular level structure outlined in the previous section, conventional laser cooling methods that allow the production of atomic quantum gases fail for $^{23}Na^{40}K$ molecules[1]. Therefore the first part of the work presented in this thesis consisted of assembling molecules from a mixed sodium and potassium quantum gas. In the following, I will briefly outline the involved states, which will then be discussed in detail below.

We first create weakly bound, so-called Feshbach molecules from the initial scattering state. Feshbach molecules are comparatively easy to make and are associated to the triplet $a^3\Sigma$ potential, but their lifetime is only milliseconds, and, worse, since their binding energy is on the order of 100 kHz, they do not possess a significant electric dipole moment. But they are an excellent starting point for a state transfer.

The target state is the rovibronic ground state in the singlet $X^1\Sigma$ potential. Since it is the most deeply bound state, molecules in it have very long lifetimes and a large permanent electric dipole moment of $d = 2.72$ D [60] in the case of $^{23}Na^{40}K$. But a single-photon transition between Feshbach and ground state molecules is impossible, due to their different spin character and a negligible Franck-Condon factor.

Therefore a third, mediating state is necessary. This electronically excited state needs to have mixed spin character, e.g. due to an accidental degeneracy between a singlet and a triplet level and have favorable transition matrix elements with both the initial and the final states. In $^{23}Na^{40}K$, two different excited states have been successfully employed for state transfer: the $v_c = 35$ state associated with the $B^1\Pi/c^3\Sigma$ system [61] and, in this work, the $v_d = 5$ state associated with the $d^3\Pi/D^1\Pi$ system. While our d/D scenario has the advantage of an one order of magnitude larger pump transition dipole moment, the B/c scenario has Fermi contact hyperfine interaction, which simplifies the transfer process. Details will be discussed in Chapter 4.

In the following, we will discuss the structural details of the Feshbach state $|\mathcal{F}\rangle$ and the excited-state and ground-state manifolds $\mathcal{E}$ and $\mathcal{G}$.

2.2.1 Feshbach State

Resonances in the scattering length, so-called *Feshbach resonances*, occur for colliding atoms whose scattering state is tuned close to resonance with a molecular bound state,

[1] There are, however, a few special classes of molecules that can be laser cooled and alternative cooling techniques for molecules have been developed [43–46]. Although this research is advancing rapidly, at the writing of this thesis the synthesis approach discussed here yielded the molecule samples with the highest phase space densities.

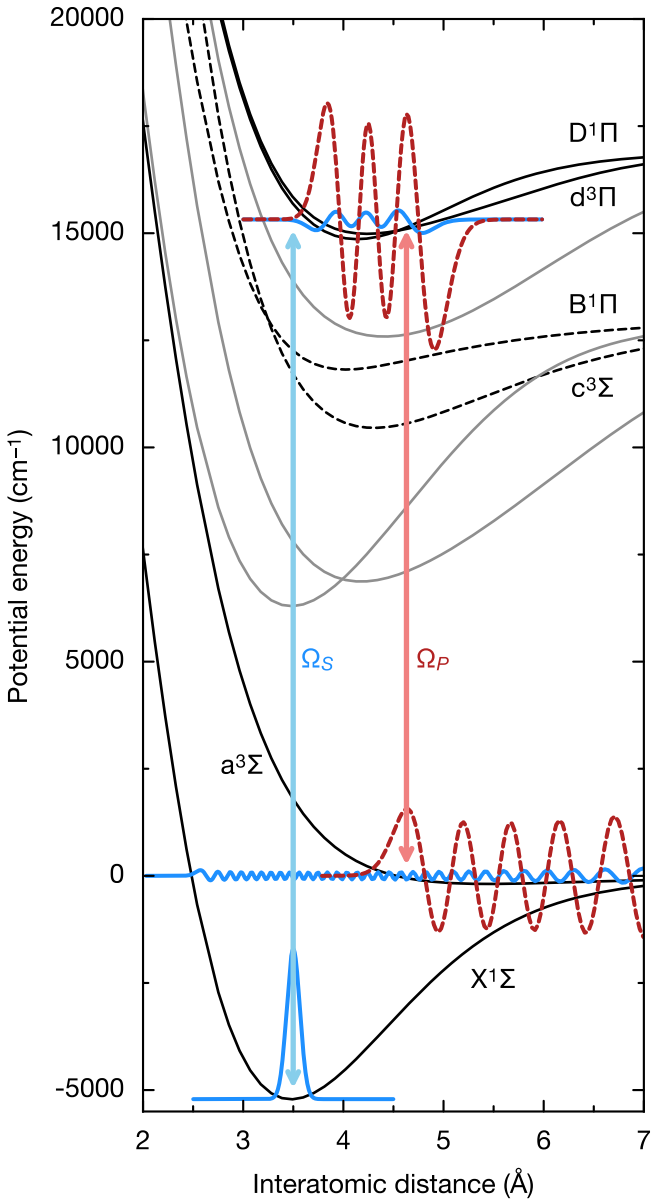

Figure 2.2: *Potential energy curves of $^{23}Na^{40}K$ according to [59]: The ground state potentials $X^1\Sigma$ and $a^3\Sigma$ and the excited state potentials $D^1\Pi$ and $d^3\Pi$, which are relevant for the present work, are indicated by black solid lines. The $B^1\Pi/c^3\Sigma$ system used as intermediate state in [24] is indicated with dashed lines. The vertical lines symbolize the pump- (P) and Stokes (S) lasers used to populate the rovibronic ground state by STIRAP, with the respective Rabi frequencies denoted as Ω_P and Ω_S. Exemplary, we show the singlet (solid) and triplet (dashed) component of one state in $\mathcal{E}$ and $\mathcal{G}$ and one spin projection for $|\mathcal{F}\rangle$ (scaled up by a factor of 100). Adapted from [26].*

e.g. with the help of an external magnetic field B, see [62]. They can occur between atoms of the same species, or of different species, and are a convenient tool to tune interactions in ultracold quantum gases. Also, they opened the door to the world of ultracold molecules: On the side of the resonance where the scattering length is large and positive, a weakly bound molecular state emerges. Molecules in this state are accordingly called *Feshbach molecules*. This state can then selectively be populated to create Feshbach molecules, see [48] for a comprehensive review.

Feshbach Association

Mainly two techniques are used for Feshbach association of molecules: magneto and radio-frequency (RF) association. In the first case, the magnetic field is swept from the negative to the positive side of the Feshbach resonance to populate the Feshbach state. In the second case, the magnetic field is set to a fixed value, on the positive side and close to the resonance, and an RF photon is used to transfer the binding energy to the atom pair. We use the latter technique. Note, that in any case a magnetic field will be present that adds Zeeman interactions to all molecular levels.

For ^{23}Na and ^{40}K mixtures, several Feshbach resonances have been explored [63, 64][2]. We use the Feshbach resonance at 88.9 G in the $|F,m_F\rangle = |1,1\rangle_{\mathrm{Na}}\ |9/2,-9/2\rangle_{\mathrm{K}}$ collision channel, where F denotes the total spin of the atom and m_F is the corresponding eigenvalue. Sodium and potassium are prepared in $|1,1\rangle_{\mathrm{Na}}$ and $|9/2,-7/2\rangle_{\mathrm{K}}$ state before we ramp the magnetic field up to 85.4 G. Using RF association, we create Feshbach molecules with a binding energy of 80 kHz. Fig. 2.3 (B) shows an RF association spectrum. Comparing the height of atomic and molecular peaks in the spectrum demonstrates the low efficiency of the process: Only 15 % of all potassium atoms become molecules. One reason for this might be bad overlap: In real space, the different masses and polarizabilities lead to different gravitational sag and different momentum distributions, and in phase space the different spin statistics of the bosonic ^{23}Na atoms and the fermionic ^{40}K mixture prevent perfect overlap. In the future, this will be remedied using a three-dimensional (3D) optical lattice. Currently, however, we routinely produce up to 15.000 Feshbach molecules in a bulk gas, which is sufficient for the studies presented in this thesis.

In contrast to the pulsed, fixed-frequency RF association technique discussed in [55, 56], we lately use a frequency sweep (50 kHz in 0.2 ms) starting from the higher frequency. As expected, this does not improve association efficiency, but leads to more stable Feshbach molecule numbers.

[2] For Feshbach resonances in the bosonic sodium-potassium mixture see [65].

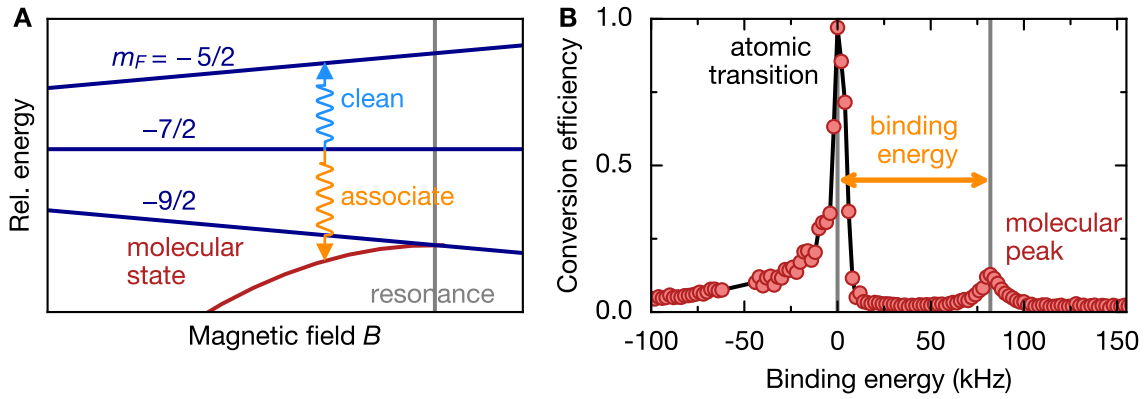

Figure 2.3: *RF association of Feshbach molecules. (**A**) RF association schematic. Potassium atoms are prepared in the $|F, m_F\rangle = |9/2, -7/2\rangle$ state and close to an interspecies Feshbach resonance (grey line). Sodium atoms are in the $|1,1\rangle$ state. With an RF photon (orange) the mixture is transferred to the Feshbach state (red). A cleaning pulse (blue) transfers remaining atoms in $|9/2, -7/2\rangle$ to further detuned hyperfine states. (**B**) RF association spectrum. When scanning the frequency of the RF photon, the atomic transition to $|9/2, -9/2\rangle$ (large peak) and the molecular bound state (small peak) appear. The conversion efficiency to Feshbach molecules is roughly 15 %. Adapted from [55].*

Feshbach Wavefunction

Coming from this experimental angle, it is intuitively clear what is meant when someone talks about a Feshbach molecule. However, determining the exact properties of such a Feshbach molecule mathematically quickly gets involved. For example, the Feshbach state $|\mathcal{F}\rangle$ depends critically on the binding energy of the molecule.

Previously we tried to gain insights regarding the spin state composition of $|\mathcal{F}\rangle$ using a *asymptotic bound state model* (ABM, see [56]). The advantage of such an approximate calculation is its relative computational simplicity: Instead of the full molecular potential, only the few closest molecular bound states are taken into account for setting up an ABM. The scattering continuum is completely neglected. This simplifies the Schrödinger equation and facilitates an exact diagonalization of the approximate Hamiltonian. However, the predictions of the ABM were not compatible with experimental results. The ABM neglects short-range effects, which are, however, relevant for STIRAP. Qualitatively, this can be understood by looking at Ref. [66]: The authors compare an ABM calculation with a full, numerical, coupled channels (CC) solution for ^{6}Li^{133}Cs. They find that they need to minimize free parameters and consider higher order couplings to reproduce the CC results with an ABM.

E. Tiemann, with whom we collaborated on this project, provided the CC results

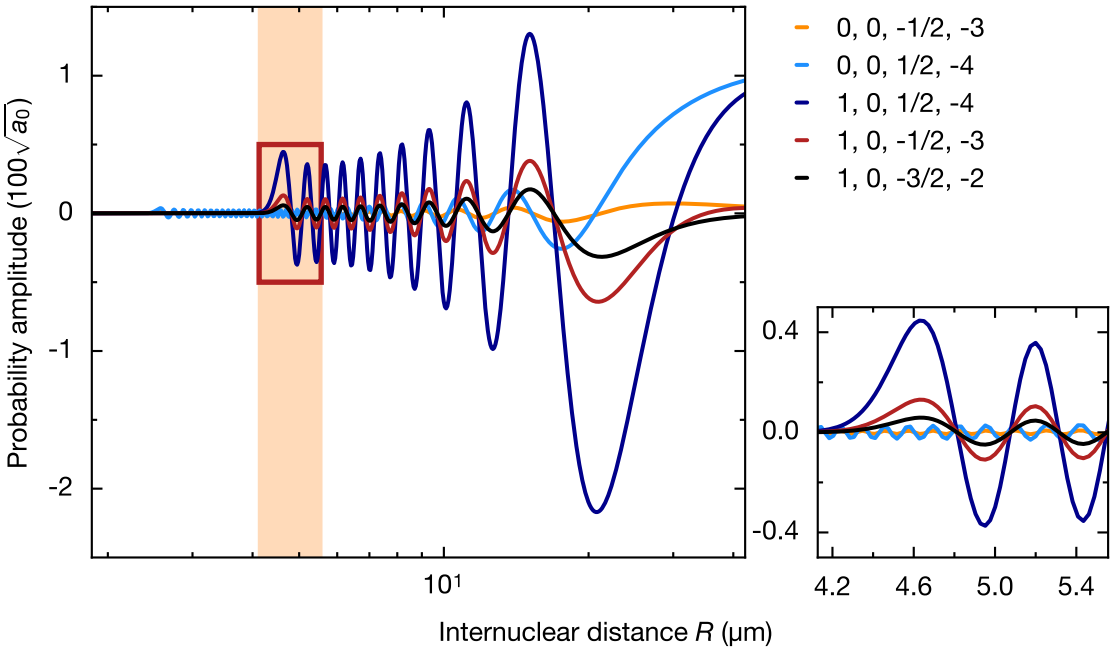

Figure 2.4: *A few spin projections of the wavefunction of the Feshbach state with quantum numbers J, m_J, m_{Na}, m_{K}. The singlet wavefunctions with $J = 0$ oscillate more frequently than the triplet wavefunctions with $J = 1$. The small plot is a zoom of the red box in the main figure.*

for our specific ^{23}Na^{40}K Feshbach molecule. Some spin projections of this wavefunction are displayed in Fig. 2.4. We expand the Feshbach state $|\mathcal{F}\rangle$ in terms of a nuclear-spin-decoupled basis $|J, m_J, m_{\mathrm{Na}}, m_{\mathrm{K}}\rangle$, where J is in the case of Feshbach molecules equal to the total electronic spin $S \in \{0,1\}$, with eigenvalues m_J. This is a convenient basis for all molecular states that we will encounter on the way to the ground state. The Feshbach state is then given as

$$|\mathcal{F}\rangle = \sum_{J, m_J, m_{Na}, m_K} |J m_J m_{Na} m_K\rangle \, |\psi_{\mathcal{F}, J m_J m_{Na} m_K}\rangle \,, \tag{2.8}$$

where $|\psi_{\mathcal{F}, J m_J m_{Na} m_K}\rangle$ are the radial parts of the projection of $|\mathcal{F}\rangle$ on to the respective spin states.

2.2.2 Intermediate State Manifold

The intermediate, excited state serves as the bridge between the weakly bound Feshbach molecules and the desired deeply bound ground state molecules. Therefore it needs to exhibit strong singlet-triplet mixing. States with mixed spin-character occur,

for example, due to accidental degeneracies between molecular levels of different potentials. Due to the sheer amount of molecular levels, this happens usually for several states. These can then be further categorized by their wavelength requirements and their transition matrix elements to Feshbach and ground states.

In ^{23}Na^{40}K, $v_d = 5$, $J = \Omega = 1$ seemed to be a promising intermediate state [67][3]. Strictly speaking, it is not a single state, but a manifold of excited states $\mathcal{E}$ (see note[4]), because it contains several hyperfine (HF) components that can be excited starting from $|\mathcal{F}\rangle$. $\mathcal{E}$ has significant spin-orbit coupling, that results in a 2% admixture of $D^1\Pi$, $v_D = 6$, and suitable transition dipole moments to $\mathcal{G}$ and $|\mathcal{F}\rangle$ with a magnitude on the order of 0.01 D. The *pump* transition dipole moments between $|\mathcal{F}\rangle$ and states in $\mathcal{E}$ in particular is about one order of magnitude larger than for the $v_c = 35$, $J = 1$ [59, 61], that has also successfully been used as intermediate state in molecule production. Typically, this pump transition matrix element limits the maximal coupling to $\mathcal{G}$ since it is smaller than the *Stokes* transition matrix element between $\mathcal{E}$ and $\mathcal{G}$. This is simply due to Franck-Condon factors, which are given by the square of the radial wave function overlap integral. However, in our d/D case the electronic spin projection $\Sigma = 0$ vanishes, which results in the absence of a Fermi contact HF interaction [55]. Therefore, and since the orbital interaction in Na is small [68], we can not spectroscopically resolve the HF structure in $\mathcal{E}$. This is consistent with the observations in our photoassociation experiments [55, 57], in which we illuminated unbound atom mixtures with the pump laser and observed atom loss whenever the laser was resonant with an excited state.

Finally we perform high resolution pump spectroscopy with Feshbach molecules. Instead of sweeping the pump laser frequency we now keep it fixed for each shot to resolve narrow spectral features. For the $J = \Omega = 1$ level it is clearly visible, see Fig. 2.5 (A), that the Feshbach field splits the transition line in three components due to the Zeeman effect. However, as expected, no finer structure can be resolved.

To learn more about the spin state composition of the individual components we repeat the high resolution pump spectroscopy for different polarizations of the pump laser. In the following, α denotes the angle of the laser polarization with respect to the axis defined by the applied Feshbach magnetic field. 0°corresponds to π-polarization, 90°corresponds to $\sigma^+ + \sigma^-$-polarization. The result of these measurements is shown

[3]The five Hund's cases labelled from a to e describe the relative strengths of the electrostatic coupling of the electronic angular momentum $\mathbf{\Lambda}$ to the internuclear axis, the spin-orbit coupling and the rotational coupling of Λ and electronic spin $\mathbf{\Sigma}$ to the total angular momentum $\mathbf{J}$ [58]. Case (a) is relevant here: The electrostatic interaction is strong, the spin-orbit coupling is intermediate and the rotational coupling is weak. Therefore, $\Omega = \Lambda + \Sigma$, the sum of the axial components of $\mathbf{\Lambda}$ and $\mathbf{\Sigma}$, is a useful quantum number. $\mathbf{\Omega}$ is defined as the vector of length Ω pointing along the internuclear axis.

[4]I use $\mathcal{E}$ and $\mathcal{G}$ without a surrounding ket symbol when I refer to the state manifolds of excited and ground states, in contrast to single states, like the Feshbach state $|\mathcal{F}\rangle$.

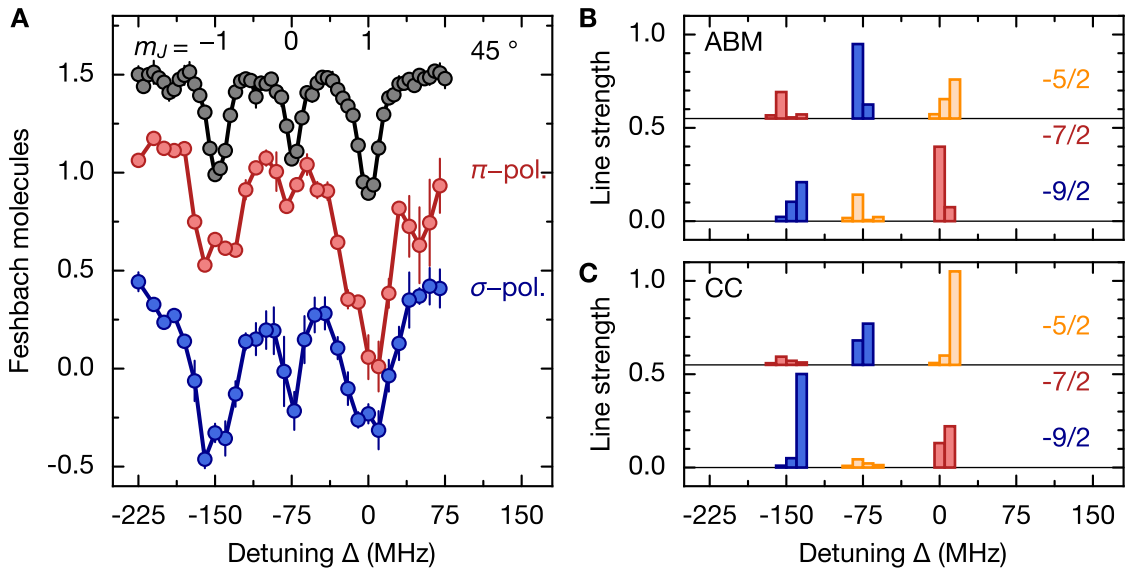

Figure 2.5: *(**A**) The excited state as observed by Feshbach loss spectroscopy with three different pump laser polarizations. The three Zeeman components $m_J = 0, \pm 1$ are clearly visible. In the case of π polarization (red), the central component is very small. For the $\sigma^+ + \sigma^-$-polarization case (blue), all three lines have a similar amplitude. For the black data set, the polarization was set to 45 °. The black and blue data sets have been offset by 0.5 for clarity. (**B**) The expected line strengths for all hyperfine components according to the ABM model [55, 56]. Note, that all these components are degenerate and they are just offset in y-direction for clarity here. For the same reason, half of the component's values are also offset in x-direction by 0.55. The m_F quantum number of each hyperfine state is color coded. (**C**) The expected line strengths according to the CC model.*

in figure 2.5 (A) (colored lines). While for the 90°case all transitions have a similar amplitude the central line is strongly suppressed for 0°. We assign the m_J-quantum numbers 0 and ± 1 to the three dips, as noted in the figure. Since the Feshbach molecule state has $m_F = 1 - 9/2 = -7/2$ and due to the selection rule $\Delta m_F = 0, \pm 1$ the $m_J = -1$ component must have $m_I = m_{I,Na} + m_{I,K} = -5/2$ and thus contain 4 hyperfine levels (due to m_I combinatorics). Likewise, $m_J = 0$ has $m_I = -7/2$ and contains 3 hyperfine levels and $m_J = 1$ has $m_I = -9/2$ and contains 2 hyperfine levels.

To describe $\mathcal{E}$ formally, we approximate the Hamiltonian by a Zeeman term and an imaginary damping term that models decay to other molecular states

$$\hat{H}_{\mathcal{E}}/\hbar = (\hat{J}_z - 1) g \mu_B B - \frac{i\gamma}{2} - \Delta', \tag{2.9}$$

$\hat{J}_z$ denotes the angular momentum operator along the magnetic field axis with eigen-

values m_J and μ_B is the Bohr magneton. For Hund's case (a) $g = \Omega(\Lambda + g_e\Sigma)/(J(J+1))$ [68], where g_e denotes the g-factor of the electron, so that we here obtain $g = 1/2$. The excited states decay with a rate γ and $\Delta' = \omega_P - E_{\mathcal{E}}/\hbar$ is the detuning of the pump laser from transition between $|\mathcal{F}\rangle$ and the upper Zeeman component $|\mathcal{E},m_J = 1\rangle$ with energy $E_{\mathcal{E}}$. The total number of states in this manifold with $J = 1$ is $36 \times 3 = 108$. No further molecular levels have to be considered, since even the nearest one $|v_d = 5,J = 2,\Omega = 1\rangle$ is already 7.2 GHz away. A damped Hamiltonian evolution is a good approximation to the full dynamics since spontaneous decay from this intermediate state ends almost exclusively in uncoupled states.

The excited states in $\mathcal{E}$ are given by

$$|\mathcal{E},Jm_Jm_{Na}m_K\rangle = |\mathcal{E},Jm_J\rangle\,|m_{Na}\rangle\,|m_K\rangle\,(|\psi_{\mathcal{E},0}\rangle + |\psi_{\mathcal{E},1}\rangle), \tag{2.10}$$

where $|\psi_{\mathcal{E},s}\rangle, s \in \{0,1\}$ are the electronic spin singlet and triplet components of the radial part of $\mathcal{E}$. In contrast to $|\mathcal{F}\rangle$, they essentially do not depend on the nuclear spin states because of negligible HF interaction compared to spin-orbit interaction.

Next we determine the coupling matrix elements relevant for the transfer. Let us assume a general coupling field $\mathbf{E}(t)$ of the form (see e.g. [69])

$$\begin{aligned}\mathbf{E}(t) &= \mathbf{E}_P(t)\sin(\omega_P t + \phi_P(t)) \\ &\quad + \mathbf{E}_S(t)\sin(\omega_S t + \phi_S(t)) \\ \mathbf{E}_P(t) &= \mathbf{E}_{0,P}\sin\left(\frac{\pi}{2}\frac{t}{\tau}\right), \quad \mathbf{E}_S(t) = \mathbf{E}_{0,S}\cos\left(\frac{\pi}{2}\frac{t}{\tau}\right)\end{aligned} \tag{2.11}$$

where $\mathbf{E}_{0,x}$ denotes the amplitude vector, $\phi_x(t)$ a time dependent phase (noise) term and ω_x the carrier frequency, the index x distinguishing between either pump (P) or Stokes (S) field. τ is the coupling light pulse duration. We work in the rotating frame of these laser fields and employ the rotating wave approximation (RWA). Using the expressions for the Feshbach state $|\mathcal{F}\rangle$ of Eq. 2.8 and the intermediate state $|\mathcal{E},Jm_Jm_{\mathrm{Na}}m_{\mathrm{K}}\rangle$ of Eq. 2.10 the coupling matrix element for the pump transition $|\mathcal{F}\rangle \to \mathcal{E}$ is proportional to

$$\begin{aligned}\langle\mathcal{F}|\mathbf{E}\cdot\hat{\mathbf{d}}|\mathcal{E},Jm_Jm_{\mathrm{Na}}m_{\mathrm{K}}\rangle \propto E_P \sum_{J'm_J'm_{Na}'m_K'q} &\alpha_q(2J+1)^{-1/2}\,\langle J'm_J'1q|Jm_J\rangle \\ &\times \langle\psi_{\mathcal{F},J'm_J'm_{\mathrm{Na}}'m_{\mathrm{K}}'}|\psi_{\mathcal{E},J}\rangle \\ &\times \langle m_{\mathrm{Na}}'|m_{\mathrm{Na}}\rangle\,\langle m_{\mathrm{K}}'|m_{\mathrm{K}}\rangle\end{aligned} \tag{2.12}$$

where q labels the polarization (0 corresponds to π-polarization and ±1 to σ^+/σ^-) and α_q is the polarization vector of $\mathbf{E}_P(t)$. In Eq. (2.12), the first factor is the conventional Clebsch-Gordan coefficient and represents the part of the Hönl-London factor which depends on the laboratory fixed quantum numbers. The second factor is

Table 2.1: *Overlap integrals for the pump transition for different spin components of the Feshbach molecule for $m_F = -7/2$ and $S = 1$. The sum of the squared values is normalized to 1. Adapted from [26].*

m_J	m_{Na}	m_{K}	overlap integral
-1	-3/2	-1	-0.095
-1	-1/2	-2	0.209
-1	1/2	-3	0.148
-1	3/2	-4	0.114
0	-3/2	-2	-0.100
0	-1/2	-3	-0.223
0	1/2	-4	-0.708
1	-3/2	-3	0.362
1	-1/2	-4	0.470

the radial function overlap integral, the square of which is the Franck-Condon (FC) factor. The last ones are matrix elements in the nuclear spin space yielding zero or one. We apply the Franck-Condon principle assuming that the electronic transition moment is constant over the needed internuclear separation. For the chosen intermediate state, the FC factors in the above expression originate mainly from the inner turning point of the triplet part of the Feshbach wavefunction, see Fig. 2.2. Since the singlet part with $J' = 0$ is rapidly oscillating, see Fig. 2.4, its FC factors are very small and thus all singlet terms will be neglected in the coupling between $|\mathcal{F}\rangle$ and $\mathcal{E}$. Overlap integrals for our specific $|\mathcal{F}\rangle$ and $\mathcal{E}$ are given in table 2.1. In figure 2.5 (**B**) and 2.5 (**C**) the transition amplitudes directly obtained by squaring the Franck-Condon factors for transitions from the Feshbach molecule to the excited state for various hyperfine states are visualized by bars for the ABM [55, 56] and the CC model. The lengths of the bars indicate the magnitude of the transition probability and they are grouped according to the m_J component that contains them. Different m_F values are color-coded according to their quantum number. An excited state spectrum is shown for reference. In the ABM model, one of the $m_F = -7/2$ components in $m_J = 1$ seems to be the most promising candidate level as intermediate state: It is addressable with π-polarization which can be realized in the current setup. According to the CC model, Table 2.1 shows that the largest coupling matrix elements belong to the $(J,m_J,m_{Na},m_K) = \{(1,0,1/2,-4),(1,1,-1/2,-4),(1,1,-3/2,-3)\}$ spin projections of $|\mathcal{F}\rangle$. For resonant driving ($\Delta' = 0$) the dynamics will therefore be dominated by couplings to $m_J = 1$ states in $\mathcal{E}$. the $m_F = -5/2$ component is a much better choice. Addressing it would require σ^+-polarized light. There is also an equally strong $m_F = -9/2$ transition, which could also be used. But we neglect it for the moment as it would lead to a higher energy hyperfine state in the rovibrational ground

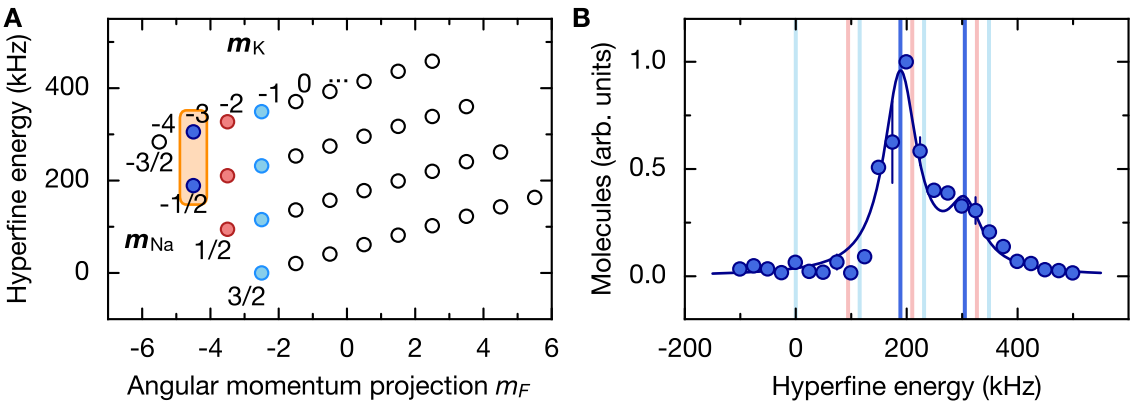

Figure 2.6: *Hyperfine structure of the rovibrational ground state. (**A**) All the hyperfine states of $^{23}Na^{40}K$. States, that are accessible with a two-photon transition from the current choice of Feshbach molecule, are colored. A spectrum of the states in the orange box is shown in (**B**). The line is a double-Lorentzian fit to the data and serves as a guide to the eye. Vertical lines belong to the states in (**A**) with the same color. This spectrum was recorded with π polarization on the Pump and $(\sigma^+ + \sigma^-)/\sqrt{2}$ polarization on the Stokes beam. The other hyperfine states can be addressed using different polarizations.*

state, as we shall see below.

Further, we can qualitatively compare the two calculations to the experimentally measured PA spectra with π and $\sigma^+ + \sigma^-$ polarization, see figure 2.5 (A), by adding up the respective transition amplitudes. Again we find better agreement with the CC model.

2.2.3 Ground State Manifold

In the rovibronic ground state, the nuclear spin is the only degree of freedom. Therefore, the Hamiltonian only contains nuclear Zeeman and nuclear spin-spin interaction terms. Since the nuclear spins for sodium $I_{\mathrm{Na}} = 3/2$ and $I_{\mathrm{K}} = 4$, the nuclear spin basis for $^{23}\mathrm{Na}^{40}\mathrm{K}$ contains $4 \times 9 = 36$ states. This is the ground state manifold $\mathcal{G}$, which is depicted in 2.6 (a). Since $\mathcal{G}$ is only accessed in the presence of the Feshbach field $B = B_F = 85.5$ G, the Hamiltonian can be approximated in the Paschen-Back limit for large magnetic fields, where the nuclear spins uncoupled from the electronic angular momentum. This is justified because hyperfine (HF) interactions are small. It is given as

$$\hat{H}_{\mathcal{G}}/\hbar = [(\hat{I}_{z,Na} - 3/2)\mu_{Na} + (\hat{I}_{z,K} + 4)\mu_K]B + c_4\hat{I}_{z,Na}\hat{I}_{z,K} - \delta', \tag{2.13}$$

where $\hat{I}_{z,Na/K}$ are the projections of the respective nuclear spin operators onto the magnetic field axis with eigenvalues $m_{Na/K}$, $\mu_{Na/K}$ denote the magnetic moments of the sodium and potassium nuclei, and $c_4 \approx 2\pi \times 0.4$ kHz is the scalar spin-spin interaction constant [24, 61]. The two-photon detuning of the coupling lasers, δ', is defined relative to the HF ground state at B_F with energy $E_\mathcal{G}$, i.e. $\delta' = E_\mathcal{G}/\hbar - (\omega_S - \omega_P)$. The HF states in $\mathcal{G}$ are then given by

$$|G, m_{\mathrm{Na}} m_{\mathrm{K}}\rangle = |G, J = 0, m_J = 0\rangle \, |m_{\mathrm{Na}}\rangle \, |m_{\mathrm{K}}\rangle \, |\psi_\mathcal{G}\rangle \,,$$

with $|\psi_\mathcal{G}\rangle$ being the radial part of the ground state wavefunction. Other molecular states can safely be ignored because they are detuned by at least twice the rotational constant in the ground state, $2B_{\mathrm{rot}} \approx 5.6$ GHz.

For this Stokes transition $\mathcal{E} \to \mathcal{G}$ the transition matrix element is then given by

$$\begin{aligned} &\langle \mathcal{E}, J m_J m_{\mathrm{Na}} m_{\mathrm{K}} | \, \mathbf{E} \cdot \hat{\mathbf{d}} \, | \mathcal{G}, m'_{\mathrm{Na}} m'_{\mathrm{K}} \rangle \\ &\propto E_S(t) \sum_q \beta_q \, \langle J m_J 1 q | 00 \rangle \, \langle m_{\mathrm{Na}} | m'_{\mathrm{Na}} \rangle \, \langle m_{\mathrm{K}} | m'_{\mathrm{K}} \rangle \, \langle \psi_{\mathcal{E},1} | \psi_\mathcal{G} \rangle \,, \end{aligned} \tag{2.14}$$

where β_q is the polarization vector of the Stokes field $\mathbf{E}_S(t)$.

Although the details of the ground state transfer will be discussed later in Chapter 4, I want to mention our ground state spectroscopy results already here, because they validate the assumptions discussed before. By keeping the Stokes laser on resonance while scanning the pump laser, we effectively vary the two-photon detuning δ' and record a spectrum of the hyperfine states in the ground state. One such spectrum is shown in Fig. 2.6 (b). The π-polarized pump laser was one-photon detuned with respect to the $m_J = 1$ component of the $v = 5, J = \Omega = 1$ state by $\Delta = \Delta'/(2\pi) = 100$ MHz, the Stokes laser is $\perp \equiv (\sigma^+ + \sigma^-)/\sqrt{2}$-polarized In this configuration the dominant contributions to the ground state transfer originate from the two HF components contained in $m_J = 1$. Consequently, we observe two HF components that we attribute to $m_{I,Na} = {}^{-1}/_2$, $m_{I,K} = -4$ (left peak) and $m_{I,Na} = {}^{-3}/_2$, $m_{I,K} = -3$ (right peak). A energy difference of 118 kHz between the two components can be approximately obtained by fitting two Lorentzians to the data. This is consistent with Eq. 2.13.

2.3 Polarizing Molecules

Heteronuclear, diatomic molecules such as ^{23}Na^{40}K are colloquially referred to as being *polar* molecules. It is true that they possess a large, permanent electric dipole moment [70]. This is necessary, but not sufficient: Without an external field, a gas of ^{23}Na^{40}K molecules has zero net-dipole moment, because of the rotational symmetry

of the eigenstates. However, there is a variety of of options to polarize the molecules using ac or dc fields.

Molecules in their rovibronic ground state, trapped in a far-detuned dipole trap, and subject to ac microwave or dc electric fields can be described by the following Hamiltonian [71–73]

$$\mathcal{H} = \mathcal{H}_0 + \mathcal{H}_{ac} + \mathcal{H}_{\text{opt}} + \mathcal{H}_{hf}, \tag{2.15}$$

where

$$\mathcal{H}_0 = B_{\text{rot}}\mathbf{J}^2 - d_0 E, \tag{2.16}$$
$$\mathcal{H}_{ac} = -\mathbf{d}\cdot(E_{ac}\mathbf{e}_{ac}e^{-i\omega_{ac}t} + c.c.), \tag{2.17}$$
$$\mathcal{H}_{\text{opt}} = -\mathbf{E}^*_{\text{opt}}(\mathbf{r})\hat{\alpha}(\omega_L)\mathbf{E}_{\text{opt}}(\mathbf{r}), \tag{2.18}$$
$$\mathcal{H}_{hf} \approx \mathcal{H}_Q + \mathcal{H}_{sc} \tag{2.19}$$
$$= -\sum_{i=\text{Na,K}} e(\nabla\mathbf{E})_i \cdot \mathbf{Q}_i + c_4\mathbf{I}_{\text{Na}}\mathbf{I}_{\text{K}}. \tag{2.20}$$

Here, $\mathcal{H}_0$ denotes the rigid rotor coupled to a dc electric field E. $\mathbf{d}$ is the dipole moment operator, where $d_p = \hat{\mathbf{e}}_p \cdot \mathbf{d} = dC^1_p(\theta,\phi)$ are its spherical components, where d is the permanent dipole moment of the molecule, $p = 0, +1, -1$, and the spherical basis vectors are defined as $\hat{\mathbf{e}}_0 = \hat{\mathbf{z}}$ and $\hat{\mathbf{e}}_{\pm1} = \pm(\hat{\mathbf{x}} \pm i\hat{\mathbf{y}})/\sqrt{2}$. Here, $C^k_p(\theta,\phi) = \sqrt{4\pi/(2k+1)}Y_{k,p}(\theta,\phi)$, where $Y_{k,p}$ are spherical harmonics, and (θ,ϕ) the spherical coordinates describing the orientation of the rotor. $\mathcal{H}_{ac}$ describes the coupling of the rotor to an ac field, e.g. a microwave field, with amplitude E_{ac}, frequency ω_{ac} and polarization $\mathbf{e}_{ac}$, which is $0, +1, -1$ corresponding to σ^-, π or σ^+-polarization, relative to the applied dc field. Although the trap light Hamiltonian $\mathcal{H}_{\text{opt}}$ is of similar shape as $\mathcal{H}_{ac}$, it is useful to adapt a notation in terms of the dynamic polarizability tensor $\hat{\alpha}$ to take advantage of the large detuning of the trap light frequency ω_L from any molecular transitions. $\mathcal{H}_{hf}$ finally describes the hyperfine interaction, which is dominated by the electric quadrupole contribution $\mathcal{H}_Q$ and a scalar contribution $\mathcal{H}_{sc}$. In $\mathcal{H}_Q$, $(\nabla\mathbf{E})_i$ denotes the intra-molecular electric field gradient at nucleus i, where $e\mathbf{Q}_i$ is the respective nuclear electric quadrupole moment. The nuclear spin-rotation interaction and the nuclear dipole-dipole interaction were neglected because their contributions are negligible [31].

2.3.1 dc Electric Fields

In our setup, details of which will be discussed in Chapter 3, we use four rod electrodes within vacuum to apply dc electric fields to the molecules. We then measure the Stark shift of the ground state transition at different applied voltages when making ground state molecules, see Fig. 2.7. Neglecting hyperfine structure, we use the

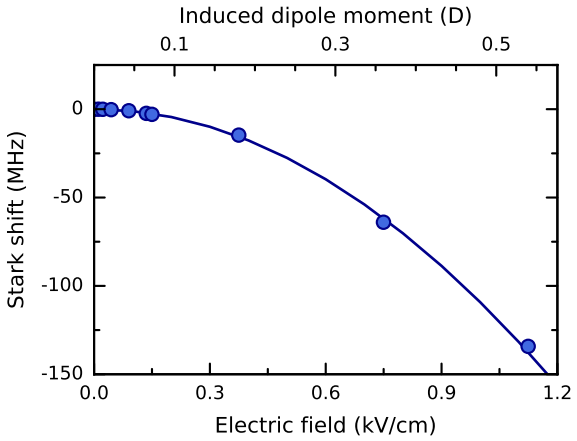

Figure 2.7: *STIRAP at high electric fields. Stark shift of the STIRAP transition for various applied electric fields (circles, lower axis). The applied electric field has been calibrated using a DC Stark shift model and the molecular dipole moment determined in [60]. The corresponding induced electric dipole moment is given on the upper axis, indicating that polar molecules with 0.54 D have been produced. Adapted from [26].*

eigenvalues of $\mathcal{H}_0$ (Eq. 2.16) and the previously determined dipole moment of 2.72 D for NaK [60] to calibrate our electric field. We further determine the induced dipole moments [74]. Thus we conclude that we can routinely produce polar molecules with dipole moments as high as 0.54 D in our setup. While Stark shift spectroscopy in dc electric fields has already been performed at fields corresponding to dipole moments up to 1.06 D in ^{23}Na^{87}Rb [25], actual polar molecules had so far only been produced with dipole moments of up to 0.3 D [24]. In this experiment, the maximally achievable dipole moment was limited by the stability of the high voltage supply, which becomes ever more important with increasing dipole moment. Therefore, we believe even higher dc dipole moments can be achieved with our setup in the future using a more stable high voltage source. Meanwhile, however, the dc-polarization record is held in ^{23}Na^{87}Rb at 0.7 D [75].

2.3.2 ac Electric Fields

Although many molecular species have been polarized using dc electric fields [22–25], using ac microwave (MW) fields to dress the rotational states directly might be even more promising to achieve large dipole moments in a gas of polar molecules. As illustrated in Fig. 2.8, molecules in the $J = 0$ manifold can be coupled to the first excited rotational manifold $|1,(0,\pm 1)\rangle$ via MW radiation with a frequency of $2B_{\mathrm{rot}}/h \approx 5.6$ GHz in the case of ^{23}Na^{40}K [31], B_{rot} denotes the rotational constant of

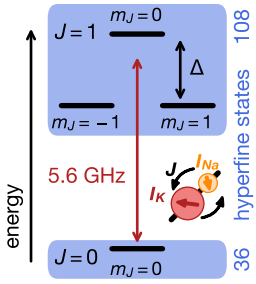

Figure 2.8: *The rotational ground and excited states $|J, m_J\rangle$ (black lines) are separated by a 5.6 GHz microwaves transition. Blue boxes denote the nuclear spin manifolds. In the $J = 1$ manifold they couple to rotation and mix. A dc Stark shift Δ can split $|1,0\rangle$ and $|1, \pm 1\rangle$, simplifying the hyperfine structure. Adapted from [36].*

the electronic ground state. Mathematically, this is described by $\mathcal{H}_{ac}$ of Eq. 2.17. Just as in the dc case in $\mathcal{H}_0$ of Eq. 2.16, the Hamiltonian is proportional to the electric field and the dipole operator.

A superposition of the rovibronic ground state $|J, m\rangle = |0,0\rangle$ and one component of the first excited state, $|0, 0\rangle$ or $|1, \pm 1\rangle$, carries a significant fraction of the dipole moment of $d/\sqrt{3}$ as the transition dipole moment [72, 73]. Figure 2.9 shows the evolution of the wavefunction probability distributions for different superpositions of rovibronic ground state and first excited state for various evolution times.

However, there is also hyperfine structure. In ^{23}Na^{40}K, there are $(2I_{\mathrm{Na}} + 1)(2I_{\mathrm{K}} + 1) = 36$ hyperfine states in the $J = 0$ manifold and 108 hyperfine states in the $J = 1$ manifold. The nuclear spins in the $J = 1$ manifold couple to rotation, predominantly via the nuclear electric quadrupole moment, see Eq. 2.20. Furthermore, the trapping light field couples different m_J-states [33, 76]. Therefore, also hyperfine state changing transitions to the excited state become possible. This is both a feature and a challenge. For one, this allows for hyperfine spin-changing MW two-photon transitions within the rovibronic ground state [29, 31]. But, on the other hand, this leads to rapid dephasing of rotational excitations. How this can be remedied will be discussed in Chapter 5.

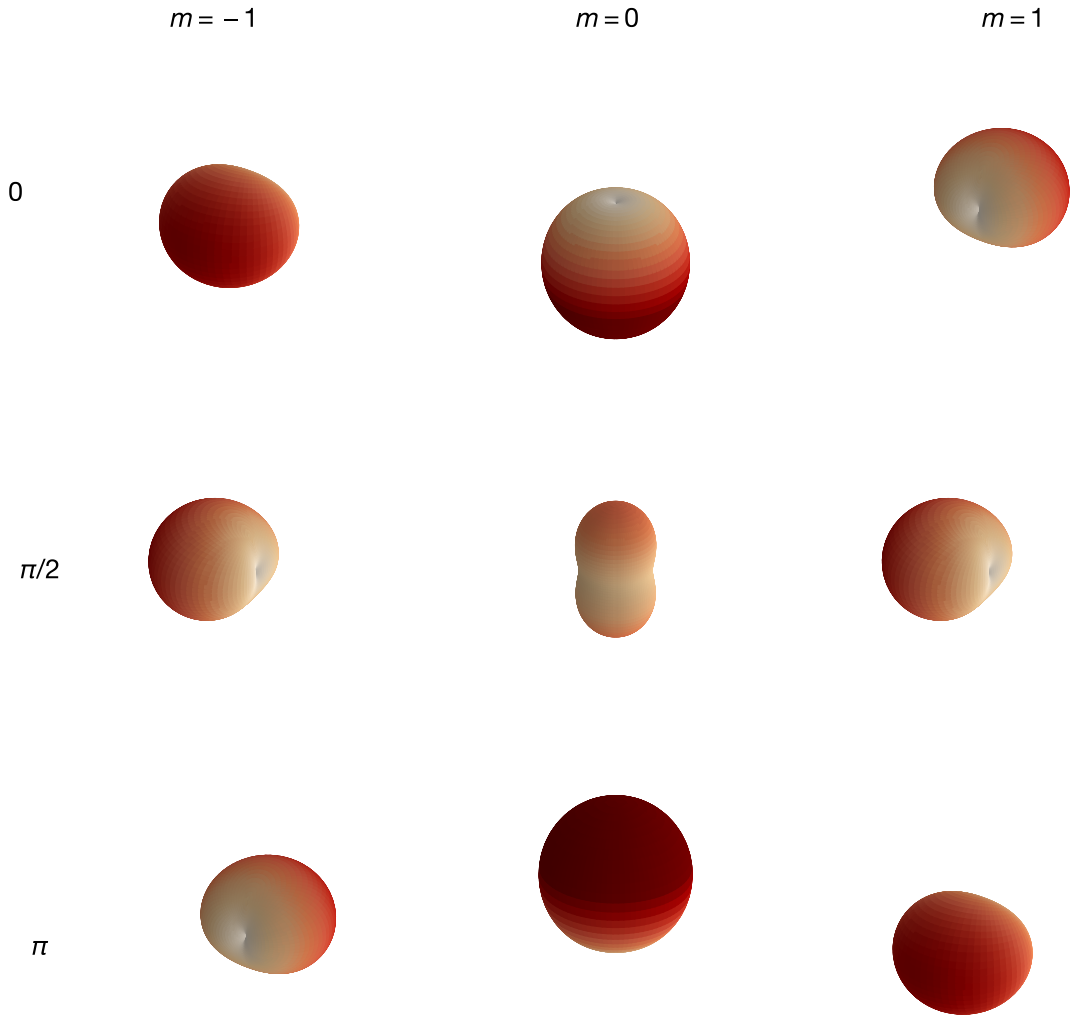

Figure 2.9: *Evolution of the probability distribution of the superposition wavefunctions* $|C_0^0 + C_m^1 e^{i\omega t}|^2$ *of* $|J,m\rangle = |0,0\rangle$ *with* $|1,-1\rangle$, $|1,0\rangle$ *and* $|1,1\rangle$ *for different values of* ωt. ω *denotes the angular transition frequency and* t *is the evolution time. The z-direction is chosen as the quantization axis for the* $|J,m\rangle$ *basis.*

Chapter 3

The Polar Molecules Machine

The Polar Molecules Machine is at the heart of the experiments performed in this thesis. Its mission is to facilitate the study of ultracold quantum gases of polar molecules with long-range interactions. In this chapter, the machine will be introduced. In Section 3.1, I will briefly summarize the key points of the base setup, which has already been described in detail in previous theses of the lab [55, 56]. Then I will move on to upgrades and additions that have since been made. These include dipole trapping of the molecules in two geometries (Section 3.2), an upgrade of the laser system for molecule production (Section 3.3) as well as electric and microwave (MW) field control (Sections 3.4 and 3.5).

At the time of writing of this thesis, the Polar Molecules Machine routinely produces 3000 ground state molecules at 300 nK. With the new tools and techniques, all parameters of the molecules, from hyperfine state over rotational level and up to the dipole moment, can now be precisely manipulated.

3.1 Overview over the Experimental Setup

In this section, the key functions of the Polar Molecules Machine are summarized. For further details, please refer to the previous theses of our lab [55, 56].

The Polar Molecules Machine is a dual species setup for the production of ultracold quantum gases of fermionic ^{23}Na^{40}K molecules. To this end, we make use of the one naturally occurring isotope of sodium, the bosonic ^{23}Na, and the only stable fermionic potassium isotope ^{40}K. The bosonic mixture of sodium and potassium ^{39}K is currently under study elsewhere [65].

The heart of the setup is the ultra-high vacuum system shown in Fig. 3.1 . It consists of two-chambers, the main chamber and the science cell, and two oven regions, one for each of the two species. Initially, both sodium and potassium are loaded into the magneto-optical-trap (MOT) in the main chamber of the vacuum system. Both species are already pre-cooled on their ways from the ovens. The sodium atoms travel through a Zeeman slower, while the potassium atoms are transversally cooled

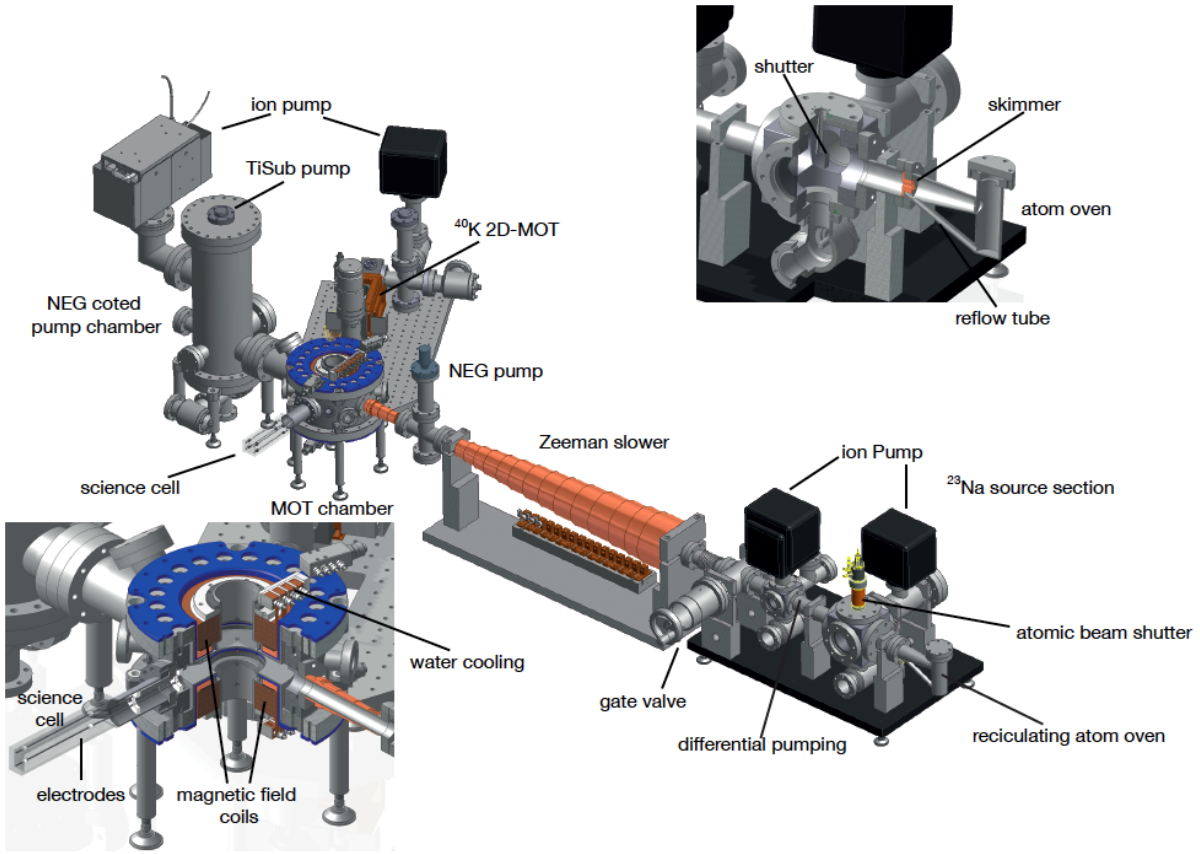

Figure 3.1: *Vacuum system of the Polar Molecules Machine. The potassium oven in the top of the central figure is connected to the MOT chamber via a 2D-MOT. The sodium atoms travel from their oven on the right through a Zeeman slower before being captured by the 3D-MOT. The upper inset shows a cut of the oven section. After the 3D-MOT, the atoms are further cooled evaporatively in a magnetic trap in the MOT-chamber. The lower inset shows a cut through the coil setup of the MOT-chamber and the science cell, to which the atoms are moved once sufficiently cool. There the molecules are created. To polarize them, four electrodes are mounted inside the corners of the science cell that allow to apply DC electric fields. Reproduced with permission from [55].*

by a 2D-MOT. After a typical MOT loading time of 4 s, both sodium and potassium are transferred to a plugged magnetic trap and prepared in their stretched, low-field seeking hyperfine states, $|F,m_F\rangle = |2,2\rangle$ and $|9/2,9/2\rangle$. Then, sodium is evaporated with MW radiation, while potassium is sympathetically cooled via elastic collisions. This essentially conserves the potassium number and thus allows us to work with small ^{40}K numbers, which is convenient because the fermionic isotope has very low abundance - even in the enriched sample we use only 3 % are ^{40}K atoms. Then we transfer the 6 µK cold mixture to a far-detuned optical dipole trap generated by a strong 1064 nm laser beam (power: 7.5 W, beam waist: $w_0 = 40\,\mu$m), that we send in through the front facet of the glass cell. We call it the *transport trap*, because in it we can move the atoms from the MOT chamber to the science cell, simply by shifting the focal point of the transport beam (28 cm in 0.75 s). The dipole force then drags the trapped atoms along. Due to the weak confinement along the beam axis the atomic cloud is elongated in this direction. To compress the mixture in the glass cell we add a second far-detuned optical dipole beam, this one at 1550 nm (power: 2 W, beam waist: $w_0 = 100\,\mu$m) horizontally. This beam and the transport trap form a “crossed trap", as they overlap under an angle. In the crossed trap, the potassium atoms are prepared in the pure spin state $|9/2,-7/2\rangle$ using an RF Landau-Zeener sweep [55] at a magnetic field of now 30 G. The sodium atoms remain in the $|1,1\rangle$ state, in which they were already prepared for transport.

The next step then depends on the experiment that shall be conducted: Either the atoms remain in the crossed trap or are loaded into a vertical 1D optical lattice that is operated at 1550 nm. Details of these two setups - which hold both atoms and molecules against gravity - will be discussed in the next section. Independent of the trap, the atomic mixture is then ready to be converted to Feshbach molecules (for details see Section 2.2.1). After Feshbach association, the molecules are transferred to the rovibronic ground state using the stimulated Raman adiabatic passage (STIRAP) technique, which will be discussed in chapter 4. The corresponding laser setup - in particular the highly stable, narrow linewidth dye laser setup - will be discussed in Section 3.3.

Once the molecules are in the ground state, we use resonant light to remove the remaining unbound atoms. This allows background free detection of the molecules and prevents collisional losses between atoms and molecules. Now experiments can be performed on the ground state molecules: To induce a dipole moment, they can be manipulated using DC electric or MW fields. Sections 3.4 and 3.5 discuss the setups to generate and control these fields with high precision.

In order to detect the remaining molecules after an experiment, we reverse the STIRAP and image the Feshbach molecules. Typically, we use high-field absorption imaging of ^{40}K at the Feshbach magnetic field in a time-of-flight measurement after all

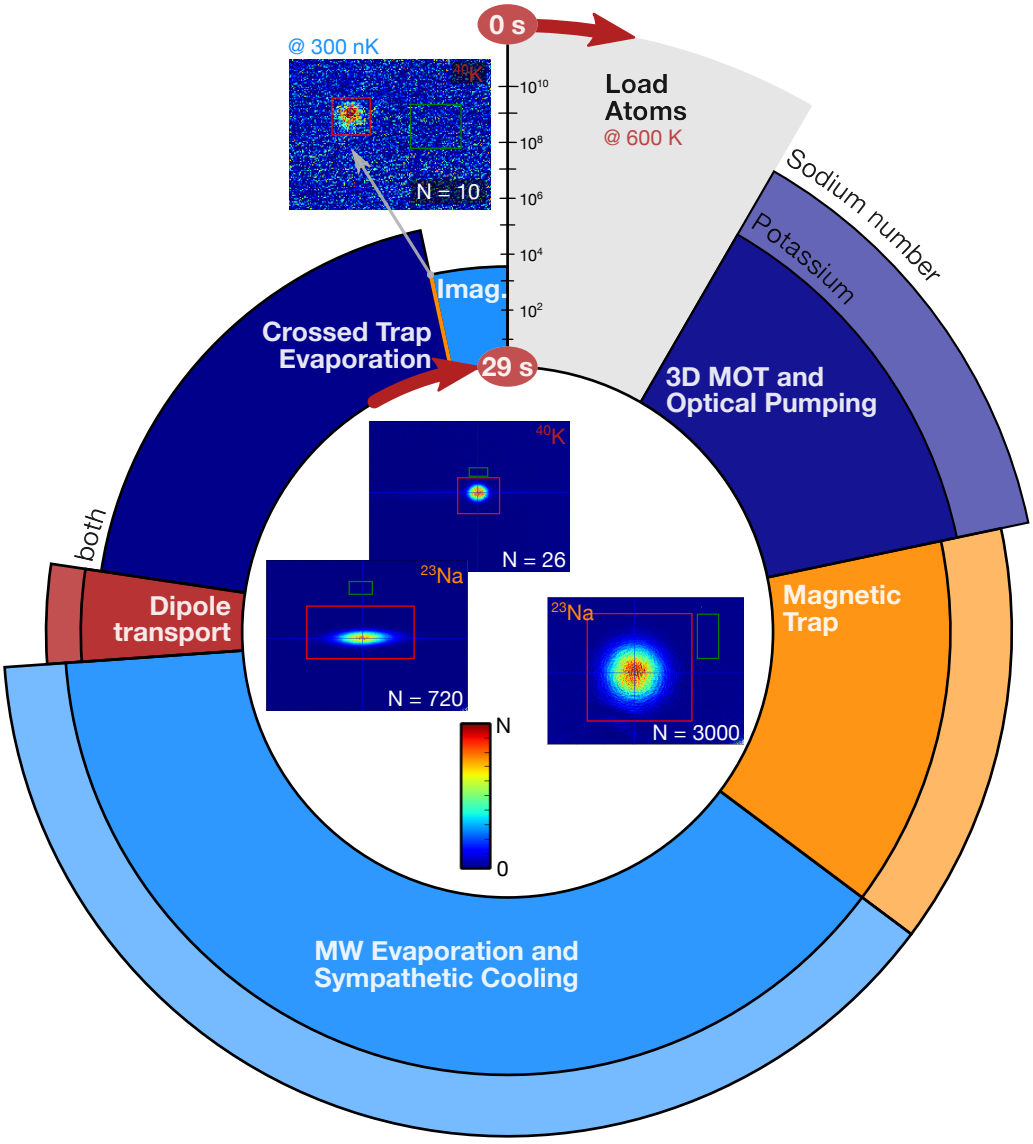

Figure 3.2: *A typical experimental cycle. The schematic illustrates the necessary steps from loading the still hot atoms (top), over cooling them up to creating molecules (going counter clock-wise). Such a cycle takes 29 s and can be divided into different experimental stages, symbolized by the colored slices. While the width of the slices indicates how long certain steps take, the amplitudes of the slices indicates first the atom and later the molecule numbers. Additionally, four absorption images of atoms or molecules illustrate the process. Here, the color denotes the amount of atoms or molecules per pixel, the normalization N is given in the bottom right corner of each image. The tiny, orange slice towards the end of the cycle indicates the creation and manipulation time of the molecules.*

traps have been turned off. The absorption cross section for our Feshbach molecules is essentially the same compared to bare atoms. From the shadow the atoms create in the near-resonant imaging beam, our image analyzer software can then extract the molecule numbers. Since the ultracold, molecular gas is destroyed in this process, the whole sequence needs to be repeated to obtain the next data point. Figure 3.2 schematically illustrates one experimental cycle with images, atom or molecule numbers and temperatures at different stages.

To ensure reproducible, exact timing of all experimental steps, we use an experimental control program developed by our group and a real time computer (ADWin-Pro). This computer is then programmed with the experimental sequences that we write in Python. It then controls the exact timing of the settings of digital and analog channels as well as direct digital synthesizers (DDS, based on AD9910) and other equipment.

3.2 Optical Dipole Traps

Ultracold atoms or molecules need to be trapped to prevent them from falling down due to gravity. The precise knowledge of their position is also required when manipulating them with other electromagnetic radiation or external fields - or for imaging.

In this thesis, experiments are performed in far-detuned optical dipole traps in two geometries, see Fig. 3.3. One is the two-color 1064 nm and 1550 nm crossed trap, the second is a purely 1550 nm 1D lattice.

Both trap types work for ^{23}Na and ^{40}K atoms and for ^{23}Na^{40}K molecules. However, due to their respective polarizabilities and masses, trap depths can differ. In the case of the molecules, the polarizability is even tunable, as will be demonstrated in Chapter 5.

3.2.1 Two-Color Crossed Dipole Trap

The beams for this trap propagate in the horizontal plane, see Fig. 3.3 A. Originally all dipole traps where planned for 1550 nm: The energy of a 1550 nm photon is far detuned from any atomic or molecular transition in ^{23}Na^{40}K, which results in similar polarizabilities for atoms and Feshbach or ground state molecules. But unfortunately it was impossible to find a reliable laser system that supplies enough power for all these purposes. Therefore, we use a 1550 nm beam for the crossed trap and a 1064 nm laser for the transport trap instead. In principle, a 1064 nm photon (corresponding to 9398 cm^{-1}) has enough energy to reach over the bottom of the lowest excited potential energy curves, not for a ground state, but for a Feshbach molecule, see Fig. 2.2. But

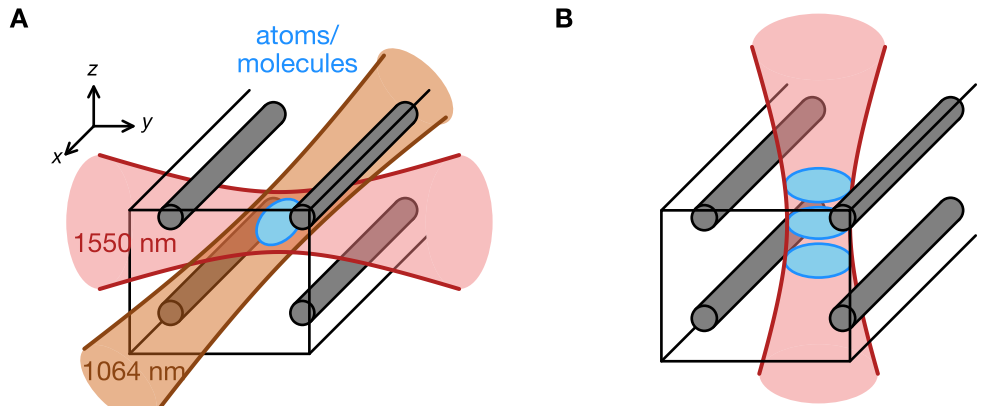

Figure 3.3: *Overview over the two trap geometries. (**A**) The crossed trap configuration in the science cell. The 1064 nm beam (red) and the 1550 nm beam (brown) cross in the x-y-plane. Due to the different beam properties, the atom or molecule cloud (blue) in the cross is elongated in the y-direction. (**B**) The lattice configuration in the science cell. A 1550 nm lattice beam along the z-direction can be loaded from the crossed trap configuration (A). The atoms or molecules then distribute over a stack of several 100 pancake-shaped planes (blue) along the z-direction. Adapted from [36].*

FC-factors for such a transition are small and since the trap wavelength is not resonant with any particular molecular transition, we use the trap without any problems. Further details about the crossed trap and how we operate it can be found in [55]. In a typical experiment, we prepare $\sim 1.3 \times 10^5$ atoms of each species in the crossed dipole trap at a temperature of 0.7 μK, the phase space density of the sample being about 0.5.

3.2.2 1D Lattice

Optical trapping frequencies depend on the polarizability of the trapped particles - which in turn depends on the wavelength of the beams. Therefore a one-color trap is advantageous to study polarizability of and identify ideal trapping conditions for rotating polar molecules as will be discussed in Chapter 5.

Therefore we have implemented a 1550 nm 1D optical lattice, see Fig. 3.3 (B). It is formed by a single, retro-reflected 1550 nm beam along the vertical direction. The beam is sent off-axis through our high-resolution objective and focused onto the atomic clouds. After traveling through the atomic or molecular cloud once, the beam is retro-reflected onto it under a small angle. Then a standing wave forms, a 1D-optical lattice, in which the atoms or molecules are confined to pancake-like 2D

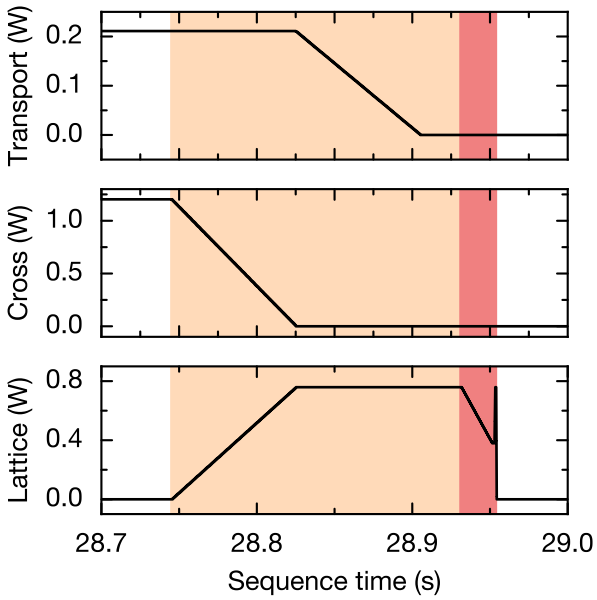

Figure 3.4: *Lattice loading and experiments in the lattice. After the Feshbach optimized evaporation of the atomic mixture in the trap formed by the transport and crossed beam, the mixture is loaded into the lattice (orange shaded area). The power in each beam is specified. Once the mixture is transferred to the lattice, molecules are created, experimented with and transferred back for imaging (red shaded area). Note that the lattice power must be the same for the two STIRAP processes at the beginning and the end of the red shaded area to avoid transfer losses through Stark shifts, but it can change in between as shown here.*

systems. Further details about the 1D lattice setup and the high-resolution imaging system can be found in [77].

Typically, we directly load atoms from the crossed trap to the lattice by slowly ramping up the lattice power while slowly turning off the crossed beams. The power settings for the different beams in this part of the sequence are shown in Fig. 3.4. The atoms are then distributed over tens of 2D lattice layers, in which they are free to move. Tunneling between the pancakes is suppressed. We then proceed with Feshbach association, just as in the crossed trap.

Later we will tune the polarizabilities of rotational states in the rovibronic ground state. Therefore, we implement precise polarization control using a polarizing beam splitter cube followed by a half-waveplate. They are installed just before the lattice beam enters the objective.

3.3 STIRAP Laser System

Making molecules consists of two steps: Associating Feshbach molecules and then transfering them to the ground state using a two-photon process called stimulated Raman adiabatic passage (STIRAP) [49]. The formation of $^{23}Na^{40}K$ ground state molecules will be discussed in detail in chapter 4. Here we will discuss the required two-color laser system.

In order to meet the adiabaticity requirements, both lasers need to be narrow in linewidth and low in noise. Therefore, we stabilize their frequencies to a common, ultra-stable reference cavity [78]. A blue 10 mW diode laser setup at 487 nm is sufficient to transfer molecules from the intermediate state to the ground state [55]. But the transition dipole moment for the other transition – from the Feshbach molecule to the intermediate state – is smaller. Therefore we replaced our initial red 10 mW diode laser system at 652 nm with a 100 mW dye laser system to achieve similar Rabi frequencies.

3.3.1 Reference Cavity

An ultra-stable cavity is used to lock the lasers with a linewidth of 1 kHz or less. It consists of two fused silica mirrors coated for 487 nm and 652 nm separated by a spacer made from ultra-low expansion (ULE) glass (all by Advanced Thin Films), which keeps the resonator length constant. In our case this spacer has the shape of a sphere, to the bores of which the mirrors are attached. We lock both the red and the blue laser system to this cavity using the Pound-Drever-Hall (PDH) locking technique [79]. The free spectral range of the cavity is 3.145 GHz and the Finesse for 487 nm (652 nm) is 30000 (188000). For more details on the cavity see [78].

First, the length of the cavity needs to be kept as constant as possible. Passive stability is achieved by using materials with as small as possible thermal expansion coefficients, such as ULE glass, and isolating the cavity from external disturbances by installing it in a small vacuum vessel and by minimizing the contact of the spacer to the vacuum vessel. In our setup from Stable Laser Systems, the sphere is secured in a fork-like mount by only two screws [80]. The vacuum vessel is then further actively temperature stabilized to the point where the temperature expansion coefficient of the spacer-mirror system is minimized [81].

But, secondly, the frequency of the stabilized lasers also depends on the specifics of the PDH lock. In PDH locking, sidebands are added to the laser frequency to distinguish the sign of the frequency derivation between laser and cavity. This is commonly achieved with electro-optical modulators (EOMs). These utilize birefringent crystals and are therefore sensitive to the polarization of the laser beam. The resulting phase

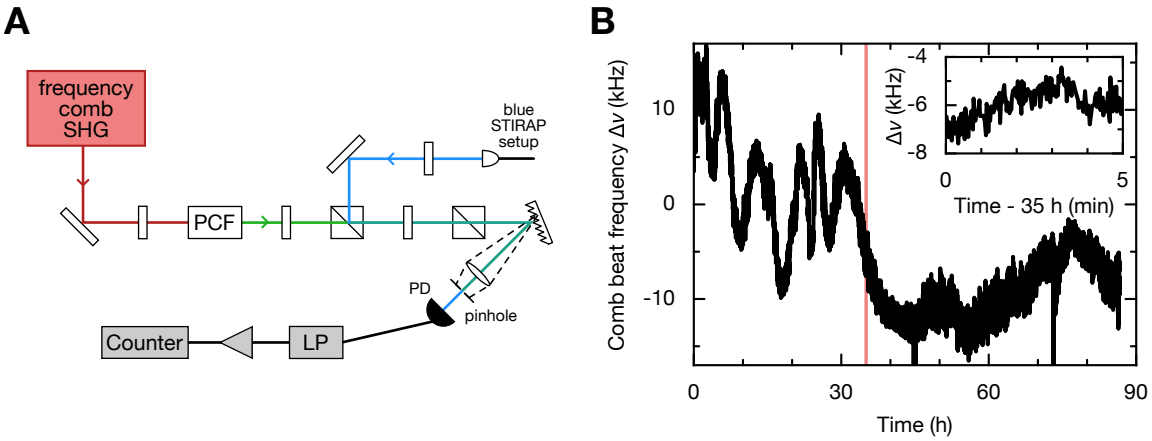

Figure 3.5: *(**A**) Setup to measure a frequency comb beat. The comb light spectrum, originally at 780 nm, is broadened in a photonic crystal fiber (PCF) to include 487 nm. Then a beat with the blue diode laser setup can be recorded. A grating and a pin-hole are used to single out the desired comb mode on the photo diode to obtain a good signal-to-noise ratio. After low-pass filtering and low noise amplification the beat frequency is recorded by a counter. (**B**) The frequency comb beat measured over several days. In the first 30 hours, regular lab work was performed next to the cavity. Afterwards, the lab work was stopped. The inset shows a 5 minute interval after 35 hours, marked red in the main figure.*

modulation of the laser light at the EOM causes an amplitude modulation at the cavity, which leads to a shift of the locking frequency. Therefore, we implement precise polarization control and the possibility to align the polarization and EOM crystal axes to minimize these effects.

To quantify the stability of the reference cavity, we measured the difference frequency of the blue laser and a frequency comb over several days. We used the frequency doubled output of our Menlo frequency comb. It operates at 1550 nm and has a repetition rate of 250 MHz, which is stabilized to 10 MHz synthesized from the Hänsch group's maser, which has an Allan deviation of 10^{-14} per hour. The comb light then travels through a photonic crystal fiber, in which the spectrum is broadened such that it includes 487 nm. To obtain a frequency comb beat with a good signal to noise-ratio, it is necessary to prevent all but the nearest comb mode from falling onto the beat photo diode. Figure 3.5 (A) shows a schematic of the setup we used. The time trace of the beat signal is displayed in Fig. 3.5 (B). We observe long time frequency drifts on the order of 20 kHz over almost 90 hours. During the first 35 hours, the lab was regularly operated and 10 kHz drifts occurred on a 5 hour time scale. Afterwards, regular lab operations was halted and the drifts reduced. On shorter timescales of several minutes, there is a 2 kHz fluctuation visible on the beat signal. This was caused by power drifts that changed the dissipated power in the cavity and hence its reso-

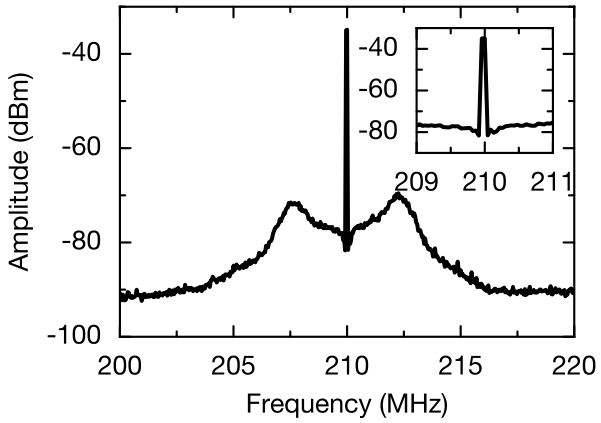

Figure 3.6: *Beat note power spectrum between the blue master and slave lasers in lock. This spectrum was recorded with a resolution bandwidth of 10 kHz and a video bandwidth of 30 Hz. The servo bumps of the lock appear at 2.5 MHz. The inset shows a zoom on the central peak.*

nance frequency. For the experiments conducted in this thesis we fixed that by careful polarization adjustment of both colors and by adding a power stabilization for the red light, see Fig. 3.7.

Since determining the linewidth of both lasers would require at least equally good reference lasers, we cannot easily determine the precise value. However, in an early stage the blue laser system was tuned to 487 nm, the subharmonic of the 243 nm ^{1}S to ^{2}S two-photon transition in Prof. Hänschs hydrogen lab, and a beat note with their 1 Hz linewidth laser was recorded [78]. From this measurement, a linewidth well below 1 kHz could be deduced.

3.3.2 Laser Locking Schemes

The ULE cavity is an excellent locking reference for frequencies that are multiples of its free spectral range. To obtain tunability in between these cavity modes, we use an offset lock: We stabilize one laser, the “master", to the reference cavity, while we lock another laser to this master with a frequency offset. Their difference frequency is measured on a fast photo diode, see Fig. 3.6 for a typical spectrum of this beat signal. Then it is mixed with a tunable local oscillator, whose frequency can be adjusted. In the case of the blue laser system, both lasers are home-built, identical diode lasers. It is shown in the top of Fig. 3.7. More details on the blue diode laser system can be found in [55].

Initially we used an identical red diode laser system: We locked a red diode laser to the ULE cavity and kept tunability via an offset lock with a second diode laser.

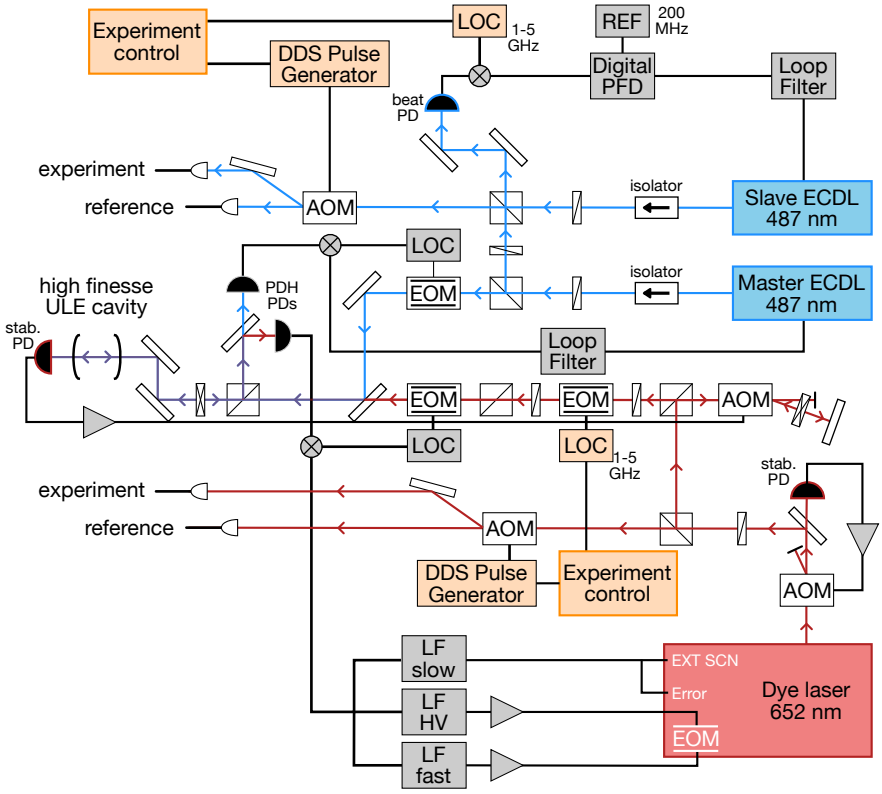

Figure 3.7: *The STIRAP laser system. In the upper part, the blue diode laser system is shown, in the lower part, the red dye laser setup. Both are locked to the ULE reference cavity with the Pound-Drever-Hall locking technique. In both cases, frequency tunability with respect to the cavity is ensured by a computer controlled 1-5 MHz local oscillator (LOC): The blue laser system is set up in master-slave configuration with an offset beat lock. In the dye laser system, a fiber EOM produces a sideband that is locked to the reference cavity. Note, that there is an output intensity stabilization and a cavity transmission intensity stabilization in the red laser system, since the output power of the dye laser can fluctuate. The STIRAP pulses are generated by DDS-controlled AOMs. The reference ports can be read out with a wavemeter or used for a stability measurement with our frequency comb.*

However, soon we replaced the diode slave laser with a narrow-linewidth dye laser, which provided more power and therefore coupling strength. We successfully used this diode master, dye slave setup for ground state molecule production as discussed in Chapter 4. During our attempts to produce as many ground state molecules as possible, we realized that an even simpler scheme could improve the production efficiency by reducing the red laser noise even further: A typical Coherent-899 ring dye laser spectrum is relatively clean due to the 1.5 m long laser cavity. If it is then locked to a diode master, in inherits the electronic noise pedestal of the diode laser. Therefore we replace the offset lock setup with a single dye laser setup. This setup is then used in the experiments described in Chapters 5 and 6.

In a Coherent-899 ring dye laser, originally a finesse $\mathcal{F} = 5$ external cavity is used to generate the locking error signal, which steers the active elements in the laser cavity - a piezo mirror, a galvo Brewster plate and the so-called thick Etalon. Under these conditions, the linewidth of the dye laser is 1 MHz [57].

To decrease this to 1 kHz, it is necessary to add a faster feedback branch to the original locking scheme. We proceed similar to what is described in [82] and introduce an intracavity EOM in the laser resonator, the two electrodes of which are controlled individually. For the fast lock we send a small portion of the dye laser output to the ULE reference cavity to generate another PDH error signal. In order to ensure dye laser tunability we do not use the carrier frequency directly, but a fiber-EOM generated sideband of the dye laser - the frequency of which we can adjust.

The threefold locking scheme consists of a slow, a high-voltage and a fast branch. For the slow branch, we keep the original error signal, but add the PDH part to it, see Fig, 3.7. Then the original Coherent control electronics supply the appropriate voltages for the previously mentioned original actuators in the laser that take care of the low frequency feedback on the order of a few kHz.

Secondly, a high-voltage feedback loop via one electrode of the intracavity EOM is implemented. A phase noise analysis of the the ordinarily locked dye laser implies that the absolute frequency change within a few ms is maximally on the order of 25 MHz [57]. Since a voltage change of 1 V at the EOM changes the frequency of the laser by 75 kHz - the $\lambda/10$ voltage of the EOM is 200 V and the free spectral range of the dye laser cavity is 150 MHz - we need at least 340 V at the EOM. The PDH error signal is sent through a PI-stage (we use a home-built fast lock box that is designed for intensity stabilization, and limit the integrator) and then to a home built HV amplifier capable of delivering up to 400 V. The high-voltage branch has a bandwidth of 800 kHz.

Finally, there is the fast branch that is introduced to the lock via the second electrode of the EOM. Here we use a Toptica-FALC module followed by the HVA-10M-

60-F voltage amplifier by femto. The fast branch then has a bandwidth of 10 MHz.

Although this locking scheme is challenging to set up, it is both robust and reliable, once the correct parameters for all three loops have been found. The dye laser system is the best option at 652 nm in terms of power and noise, despite the need for regular maintenance. This includes small realignment adjustments every other day and the exchange of the dye every one to three months.

In the STIRAP experiments discussed in Chapter 4 we will need precise control over pulse length τ and pulse shape of the two STIRAP lasers. We achieve this by programming one DDS each with the desired pulse shape (we use $\cos^2$-pulses). The DDS output is then amplified and used as the control for amplitude modulation of the respective final AOM. Since τ is on the order of 10 µs, the pulses are too short for active power stabilization. Therefore we pre-stabilize the pump and Stokes beam powers. This is sufficient, since due to the small pulse area thermal drifts in the AOM are not a problem throughout the pulse sequence. However, note that for the same reason it is best to optimize the fiber coupling to the experiment while the AOM amplitude is pulsed, not constant.

3.3.3 STIRAP Beam Alignment

Ultimately, the Rabi frequency of the STIRAP beams determines how fast and efficient the Feshbach molecules can be converted to ground state molecules. To make the most out of the available power, we match the STIRAP beam foci precisely to the Feshbach molecule cloud. Due to the elongated cloud shape, we use elliptical beams. The beam waist are $\omega_x = 105\,\mu\text{m}$ and $\omega_z = 26\,\mu\text{m}$. Now precise alignment of the beams is required to observe ground state transfer.

Both STIRAP beams are overlapped and sent to the atomic cloud, so that they propagate perpendicular to the magnetic field axis. We can thus realize parallel (π) or perpendicular ($\perp \equiv (\sigma^+ + \sigma^-)/\sqrt{2}$) polarization. To precisely align the beams, we employ two piezo-electric adjustable mirrors. We start with the red beam. For coarse alignment we use its dipole force: We adjust the beam to sit slightly underneath a cloud of sodium atoms that we then release from the trap. In a time-of-flight measurement some of the atoms will then be caught in the red beam. We then adjust the beam positions by catching as many atoms as possible. Fine alignment can then be performed by using the red beam to drive a transition between the Feshbach state (or an atomic mixture) and an excited state, once the transition frequency is known. The alignment is optimal when the loss rate of the transition is maximized.

Then we can coarse align the blue beam by simply overlapping it with the red beam. This we do with a dichroic mirror, which only affects the blue beam position. We have installed a flip mirror close to the glass cell that can project the two

beams onto a CCD camera. Finally, once the transition frequency to the ground state is known, fine alignment of the blue beam can be performed by optimizing the number of ground state molecules.

3.4 Electric Field Setup

Molecules such as $^{23}Na^{40}K$ are frequently referred to as *polar* because they posses a permanent electric dipole moment. However, at least in the rovibronic ground state, their dipole moment averages out to zero - unless they are polarized. One approach to do so is to apply strong, static dc electric fields to them. Thus the electric field setup is a key component of every polar molecules machine. The goal is to generate as large and as homogeneous DC electric fields as possible, since the larger the electric field strength, the larger the electric dipole moment induced in the molecule.

In the following I will therefore describe our electrode setup and the stable, high voltage sources we use to generate electric fields.

3.4.1 Electrodes Setup

When it comes to electrodes, there are several different options: Some experiments use two indium-tin-oxide coated electrode plates [21, 24, 25] or four rod electrodes [22, 23] outside of the vacuum system, some have coated intricate electrode structures onto the windows of their vacuum chamber [83] and some rely on in-vacuum rod electrodes [26, 33, 84].

To control direction, strength and gradient of the electric field along all axes we use a combination of four in-vacuum “main" rod electrodes and two auxiliary groups of four electrodes each, see Fig. 3.8 (A): The main electrodes consist of a stainless steel wire with a round cross section and a diameter of 2 mm. They are oriented along the x-direction and generate a near homogeneous electric field, either along the y- or the z-direction (see Fig. 3.3 for axes definitions). Note that the distance between the horizontal electrode pairs is 2.8 cm while the distance between the vertical pairs is slightly smaller, 2.6 cm.

Even though the rods are kept at a few millimeters distance from the glass by isolating spacers, we observe that the glass cell walls charge up over time when we apply DC electric fields. Once accumulated, we observed that these charges remain on the glass surfaces at least for several months – unless they are actively removed. To do so we installed three UV-LEDs at the corners of the cell that we turn on during the experimental cycle when there are no atoms yet in the science cell. This ensures that the unwanted charge distribution is stable from on experimental shot to the next.

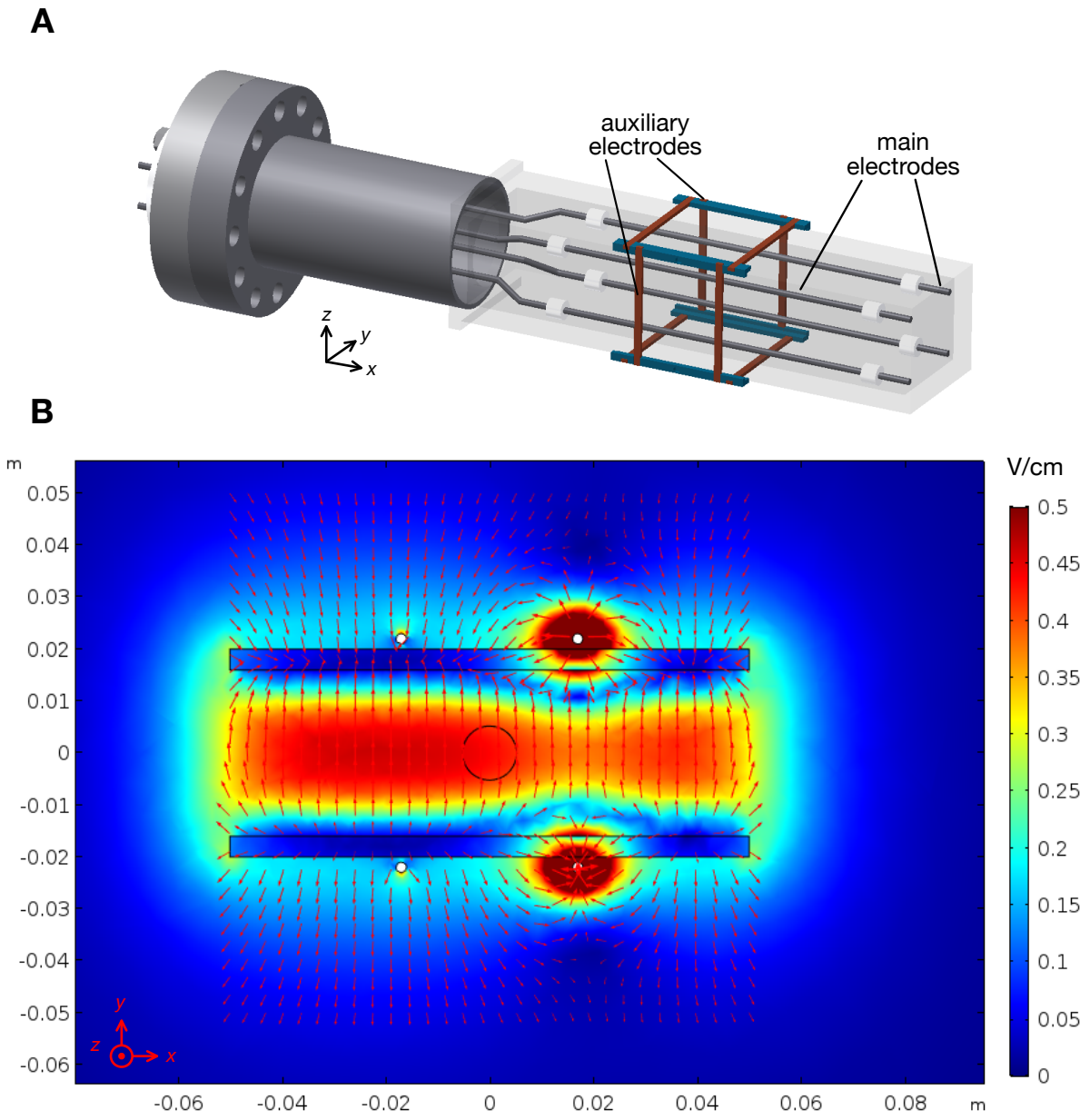

Figure 3.8: *(**A**) Model of main and auxiliary electrodes in and around the glass cell (light grey). Inside the glass cell, the main electrodes are visible (grey bars). They are isolated from the glass with ceramic spacers (white rings). The voltage supply for the main electrodes is connected via a feed through in the main chamber, to which the flange on the left is connected. Outside the science cell, two pairs of auxiliary electrodes are installed (red). These can be poled in quadrupole configuration to cancel unwanted gradient fields. (**B**) Simulation of the electric field with the full electrode configuration at the central horizontal cut through the science cell. The color denotes the electric field strength and the arrows indicate the field direction At the center of the circle, where the electric field is almost homogeneous, we create the molecules. In this image, the voltage on the main electrodes is ± 1 V and 0.5 V are applied to the auxiliary electrodes in quadrupole configuration. Please note that we applied larger voltages in most of the experiments described in this thesis.*

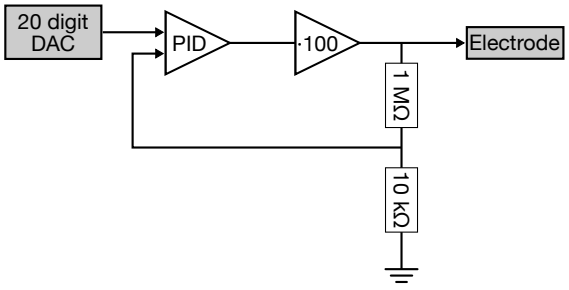

Figure 3.9: *HV setup for one main electrode. The control voltage of a precise DAC is amplified to generate up to 400 V at the electrode. To keep full flexibility for the electric field, we use four identical setups to control each main electrode individually.*

Still, in the very sensitive rotational Ramsey spectroscopy of ground state molecules, that will be discussed in Chapter 6, we observed dephasing due to electric gradient fields. This might be due to incomplete removal of charges by the UV-LEDs or inhomogeneities of the main electrodes. To cancel these we use the auxiliary electrodes. They are oriented along y- and z-axis and are set up in a quadrupole configuration. Thus they do not change the magnitude of the electric field at the position of the molecules to first order. We can also add quadrupole voltages to the main electrodes and thus compensate electric field gradients along all directions. Fig. 3.8 (B) shows the result of an electric field simulation using all electrodes.

3.4.2 Voltage Supplies

To test the main electrode setup we initially used one commercially available power supply of the company FuG per electrode pair. These were high-voltages supplies that could output up to 10 kV and were controlled with a common analog reference voltage. However, due to their noise specification of 10000 ppm and thermal drifts of the output voltage they are unsuitable to polarize molecules: This leads to DC Stark shifts of the molecular ground state that prevent reliable STIRAP, which leads to unstable molecule numbers. This is already a problem at small electric field values, but gets dramatically worse the more polar - and thus susceptible to electric fields - the molecules are. Therefore, we upgraded our electric field setup with less high-voltage, but extremely high precision voltage sources.

We use one home built, high precision voltage source with $\pm$400 V with an rms noise of 0.55 mV from 10 µHz to 15 kHz following [85] per main electrode. These voltage sources are individually controlled by high precision digital-to-analog converters (DACs), see Fig. 3.9. Since the auxiliary electrodes in quadrupole configuration do not change the DC electric field to first order, requirements for them are slightly less restrictive and we use voltage sources with an rms noise of 1 mV.

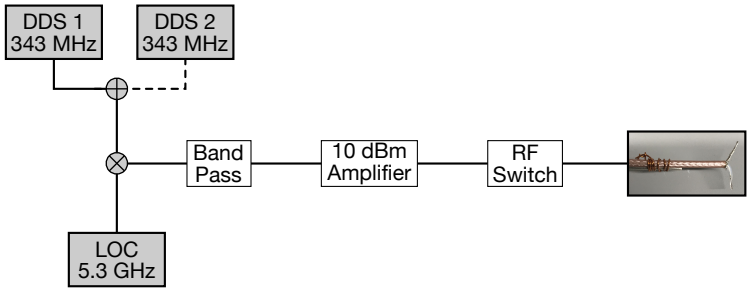

Figure 3.10: *Microwave setup for driving rotational transitions in ground state molecules. A fixed frequency local oscillator at 5.3 GHz can be mixed with one of two direct digital synthesizers (DDS) to reach the rotational transition frequency. Both DDS can be individually controlled by the experimental control. Thus we can also drive two-photon MW transitions between different hyperfine states.*

The most precise way to calibrate the electric field at the place of the molecules is measuring the DC Stark shift of the molecular rovibronic ground state using STIRAP spectroscopy. This relies on the value for the permanent electric dipole moment $d_0 = 2.72$ D of ^{23}Na^{40}K, which was determined in a heat-pipe experiment [60]. Since all four main electrodes can be controlled separately, many different electric field geometries can be realized. Due to the different spacing of the horizontal and vertical electrode pairs the conversion factor c from power supply voltage to electric field differs for the creation of a horizontal or vertical electric field. We find $c_{\mathrm{hor}} = 0.418\ \mathrm{cm}^{-1}$ and $c_{\mathrm{ver}} = 0.392\ \mathrm{cm}^{-1}$.

3.5 Molecular Microwave Setup

As we saw in Chapter 2, molecules possess many degrees of freedom that could be used in quantum simulation. The rotational one is particularly interesting, because it gives direct access to dipolar interactions and can easily be addressed with microwave (MW) radiation. The rotational transition frequency between levels with rotational quantum number J and $J+1$ is given by $2B_{\mathrm{rot}}J(J+1)$. B_{rot} is the rotational constant, which is 2.82 GHz in ^{23}Na^{40}K [31].

We use a simple, home built dipole antenna, see Fig. 3.10, that we mount close to the science cell. The orientation of the antenna with respect to the molecule axis determines, whether the MW radiation will be horizontally or vertically polarized. To control the MW frequency we use a direct digital synthesizer (DDS), that we add to a fixed frequency oscillator at 5.3 GHz. Driving two-photon transitions between different hyperfine states in the ground state requires two slightly different MW frequencies. Therefore, the setup contains a second DDS, that can be individually controlled.

Chapter 4

Ground State Molecules

The key technique in the creation of ultracold, polar $^{23}Na^{40}K$ molecules in their rovibronic ground state is a two-photon process called *stimulated Raman adiabatic passage* (STIRAP) [49]. In STIRAP, a special pulse sequence is used that enables highly efficient population transfer from an initial to a final state. It is a very general concept that is applicable in many three-level systems. In polar molecule production, it mediates the transition between the Feshbach state, the electronically excited, intermediate state manifold and the ground state manifold, which were introduced in Section 2.2. The complex molecular multi-level system goes beyond the original three-level system, but STIRAP can be generalized to such a scheme, as will be demonstrated in Section 4.1 with a toy model. We then test the validity of the model by comparing it to experimental results in Section 4.2. Finally, we explore the lifetime of the ground state molecules in Section 4.3. This chapter is based on the publication Ref. [26].

4.1 STIRAP Ground State Transfer

STIRAP is a coherent two-photon process, capable of adiabatically transferring population in a three-level system by employing a special pulse sequence. The concept has found applications in a wide range of systems, from atoms and molecules to waveguides and solid state systems, many of which are reviewed in [49, 50]. After introducing the working mechanism in a three-level system, I will show how to generalize the approach to a multi-level system as in $^{23}Na^{40}K$ molecules, e.g. with degenerate hyperfine levels in the excited state.

4.1.1 Three-Level System

A three-level system consists of three levels, $|1\rangle$, $|2\rangle$ and $|3\rangle$, and two coupling lasers, see Fig. 4.1 for an exemplary lambda-like scheme. The laser connecting $|1\rangle$ and $|2\rangle$ is called *pump* laser, while the one between $|2\rangle$ and $|3\rangle$ is called *Stokes* laser. Consequently, the transition Rabi frequencies are labeled Ω_P and Ω_S. The Hamiltonian of

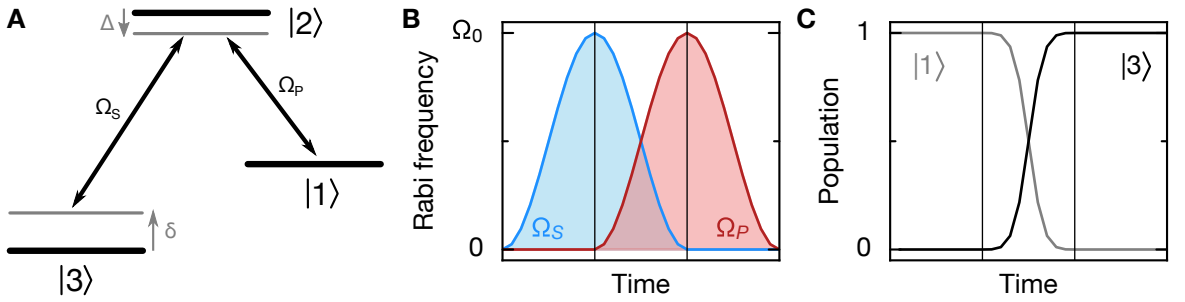

Figure 4.1: *STIRAP in a three-level system. (**A**) Three-level system that is coupled with two lasers with Rabi frequencies Ω_P (pump transition) and Ω_S (Stokes transition). The one- and two-photon detunings Δ and δ are indicated. Note, although a lambda-like scheme with one excited and two ground states is drawn, STIRAP also works in a ladder-like three-level system, as long as the two-photon resonance condition is fulfilled. (**B**) STIRAP sequence, in which the Stokes pulse precedes the pump pulse. Ω_0 denotes the peak Rabi frequency of the pulses. (**C**) Populations of initial and final states throughout the STIRAP process.*

the system is given in the rotating-wave approximation as

$$\mathcal{H}(t) = \frac{\hbar}{2}\begin{pmatrix} 0 & \Omega_P(t) & 0 \\ \Omega_P(t) & 2\Delta' & \Omega_S(t) \\ 0 & \Omega_S(t) & 2\delta' \end{pmatrix}, \tag{4.1}$$

where $\Delta' = 2\pi \cdot \Delta$ denotes the common one-photon detuning of both laser frequencies with respect to the intermediate state $|2\rangle$ and $\delta' = 2\pi \cdot \delta$ denotes the two-photon detuning of the two-photon transition between initial and final state. Successful population transfer requires two-photon resonance, $\delta = 0$. The eigenvalues of this Hamiltonian are then

$$|\Phi_+\rangle = \sin\theta \sin\phi\,|1\rangle + \cos\theta\,|2\rangle + \cos\theta \sin\theta\,|3\rangle\,, \tag{4.2}$$
$$|\Phi_-\rangle = \sin\theta \cos\phi\,|1\rangle - \sin\theta\,|2\rangle + \cos\theta \cos\theta\,|3\rangle\,, \tag{4.3}$$
$$|\Phi_0\rangle = \cos\theta\,|1\rangle - \sin\theta\,|3\rangle\,, \tag{4.4}$$

where the mixing angle θ and ϕ were defined as

$$\tan\theta = \Omega_P(t)/\Omega_S(t),$$
$$\tan(2\phi) = \Omega/\Delta',$$

and the effective Rabi frequency Ω is given as

$$\Omega = \sqrt{\Omega_P(t)^2 + \Omega_S(t)^2}. \tag{4.5}$$

One of the eigenstates, $|\Phi_0\rangle$, is special since it only contains initial and final, but not the intermediate state $|2\rangle$, which may be lossy. When the coupled system is in this state, thus no photons are emitted. Therefore, $|\Phi_0\rangle$ is frequently called a *dark state*.

This dark state has fascinating implications, e.g. in can be used to engineer the dispersion relation of light in a medium using electromagnetically induced transparency (EIT, [86]): EIT can make a medium completely transparent for an otherwise absorbed wavelength or allows to slow down and even stop light propagation [87].

However, it is also useful to transfer populations from $|1\rangle$ to $|3\rangle$ with extremely high efficiency. One can simply employ the dependence of $|\Phi_0\rangle$ on the Rabi frequencies. To obtain the starting condition $|\Phi_0\rangle = |1\rangle$, we require $\theta = 0$, so $\Omega_P/\Omega_S \to 0$ has to be fulfilled, requiring the pump beam to be off initially. In the final state, the opposite is true: $\Omega_P/\Omega_S \to \infty$ has to be fulfilled, so that $|\Phi_0\rangle = |3\rangle$, so that the Stokes beam must be off, finally.

Both these boundary conditions can be met with a special pulse sequence, in which the Stokes pulse precedes the pump pulse, while both pulses overlap for a time τ. For a STIRAP transfer with a smooth pulse shape, the following adiabaticity criterion for effective Rabi frequency Ω and STIRAP duration τ can be derived, that has been numerically verified [49]

$$\Omega\tau > 10. \tag{4.6}$$

Interestingly, the exact pulse shape for STIRAP is rather unimportant, as long as it is smooth and fulfills the boundary conditions.

4.1.2 Multi-Level System

STIRAP for polar molecule production was proposed in 2004 [47]. It can solve a critical problem in the creation of ultracold polar molecules: Feshbach molecules could be readily produced, but are not polar. And the rovibronic ground state, which possesses a large electric dipole moment in heteronuclear molecules, could not significantly be populated with the existing schemes relying on spontaneous emission. However, Feshbach molecules can simply be converted into ground state molecules using STIRAP. With this transfer approach, rovibronic ground state molecules were realized for the first time in 2008 [21]. It has now become the standard procedure for creating molecules at high phase-space density and has been succesfully applied for dipolar KRb [21], RbCs [22, 23], NaK [24, 26] and NaRb [25] molecules.

For STIRAP in molecules, the initial state is typically a Feshbach state, the final state is one of the hyperfine states in the rovibronic singlet ground state. Usually, there are several different Feshbach states or hyperfine states in the ground state that could be used. However, the biggest distinction between different routes to the ground state lies not in the initial or final states, but in the properties of the intermediate,

electronically excited state. Several criteria could be considered for the choice of this state:

- Does it have significant singlet-triplet mixing, so that initial and final state can be coupled to it?
- Are the Franck-Condon factors to the initial and final states large, so that large Rabi frequencies can be achieved on the transitions?
- And how much of the hyperfine structure of the state can be resolved?

Especially the last point is interesting and two different cases have been studied for the $^{23}Na^{40}K$ molecule. In the experiments at the Massachusetts Institute of Technology (MIT) [24], an intermediate state with partially resolved hyperfine structure [61] was used. Our group at the Max-Planck Institute of Quantum Optics (MPQ), however, chose an intermediate state with favorable singlet-triplet mixing and good transition matrix elements, as discussed in Section 2.2.2, which turned out to have a non-resolved hyperfine structure. At the time that the laser system was built the role of the hyperfine structure in STIRAP was neither considered nor understood. However, the better the resolution of the different hyperfine levels, the closer the system gets to the envisioned three-level system discussed in the previous section. But resolved hyperfine structure is not required for successful transfer of Feshbach molecules to the rovibronic ground state, as we could demonstrate in Ref. [26].

The molecular structure of the Feshbach, intermediate and ground states and manifolds that we use in molecule production has already been introduced in Chapter 2.2. We begin with $^{23}Na^{40}K$ Feshbach molecules, created close to the $m_F = -7/2$ Feshbach resonance at 88 G [64]. The intermediate state is the $|v_d = 5, J = \Omega = 1\rangle$ state associated with the $d^3\Pi$ potential and consists of three $m_J = 0, \pm 1$ Zeeman components with unresolved hyperfine structure. Here, v_d denotes the vibrational quantum number of a level of the $d^3\Pi$ potential, J refers to the total angular momentum of the molecule without nuclear spins and Ω is the projection of J onto the internuclear axis. The rovibronic ground state, finally, has a resolved hyperfine structure.

In the following, I will introduce the Hamiltonian model we developed to achieve a quantitative description of the adiabatic transfer in all required details. We explicitly consider the complex light coupling into the analysis, in addition to the molecular structure analysis done for different bialkali systems [61, 88]. Figure 4.2 is a graphical representation of the Hamiltonian. Note, that this multi-level, cross-coupled model is intimately related to the work of the Bergmann group on STIRAP in multilevel systems [89], but is specific to the alkali-alkali molecule formation.

We employ the nuclear spin decoupled molecular basis $\{|\mathcal{F}\rangle, |n, J, m_J, m_{Na}, m_K\rangle\}$, where $n \in \{\mathcal{E}, \mathcal{G}\}$. Note that the physical meaning of J, the total angular momentum

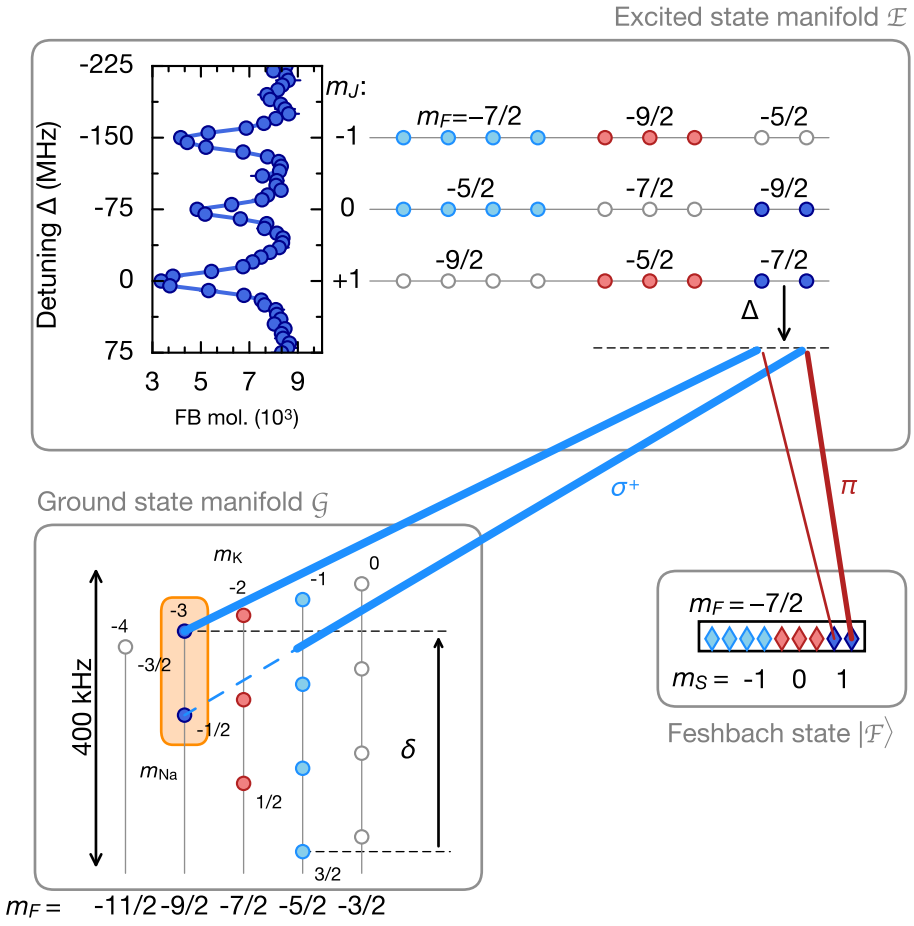

Figure 4.2: *Schematics of the multi-level STIRAP Hamiltonian. The experimental data on the upper left shows the spectrum of the excited state $v_d = 5$, $J = \Omega = 1$ at 85.5 G recorded with 45° polarization and starting with the $m_F = -7/2$ Feshbach molecules that can be created at this field (lines are a guide to the eye). Three Zeeman m_J-components are clearly visible, but no hyperfine structure is resolved. The individual hyperfine states of the excited and the ground state are indicated schematically by circles as well as the hyperfine components of the Feshbach state (diamonds). Symbols with the same total nuclear spin quantum number $m_I = m_{Na} + m_K$ ($-5/2$,$-7/2$,$-9/2$) have the same color (light blue, red, dark blue); white symbols refer to states that are not populated. Exemplary, shown by arrows, is the case of a π-polarized pump beam and a σ^+-polarized Stokes beam. In this case, only the two $m_F = -7/2$ components of $m_J = 1$ contribute to STIRAP. The strengths of the pump and Stokes transitions are different, as indicated by the thickness of the arrows. The one-photon detuning Δ and the two-photon detuning δ are also indicated. Note that the energy axis for the excited state (spectrum and schematic) is inverted for clarity. Adapted from [26].*

quantum number excluding nuclear spins, depends on n: For the Feshbach molecule, J is equal to the total electronic spin $S \in \{0,1\}$, while for the excited state $J = 1$ and in the ground state $J = 0$. In this basis the Hamiltonian is diagonal. Then, the matrix elements for pump and Stokes transitions in the rotating wave approximation are given by Eqs. 2.12 and 2.14 as

$$\begin{aligned}\langle \mathcal{F}|\mathbf{E}\cdot\hat{\mathbf{d}}|\mathcal{E},Jm_Jm_{\mathrm{Na}}m_{\mathrm{K}}\rangle &\propto E_P(t)\sum_{J'm'_Jm'_{Na}m'_Kq}\alpha_q(2J+1)^{-1/2} \\ &\times \langle J'm'_J1q|Jm_J\rangle \\ &\times \langle \psi_{\mathcal{F},J'm'_Jm'_{\mathrm{Na}}m'_{\mathrm{K}}}|\psi_{\mathcal{E},J}\rangle \\ &\times \langle m'_{\mathrm{Na}}|m_{\mathrm{Na}}\rangle\langle m'_{\mathrm{K}}|m_{\mathrm{K}}\rangle\,, \end{aligned} \tag{4.7}$$

$$\begin{aligned}\langle \mathcal{E},Jm_Jm_{\mathrm{Na}}m_{\mathrm{K}}|\,\mathbf{E}\cdot\hat{\mathbf{d}}\,|\mathcal{G},m'_{\mathrm{Na}}m'_{\mathrm{K}}\rangle &\propto E_S(t)\sum_q\beta_q\langle Jm_J1q|00\rangle \\ &\times \langle m_{\mathrm{Na}}|m'_{\mathrm{Na}}\rangle\langle m_{\mathrm{K}}|m'_{\mathrm{K}}\rangle\langle\psi_{\mathcal{E},1}|\psi_{\mathcal{G}}\rangle\,, \end{aligned} \tag{4.8}$$

where the STIRAP coupling field $\mathbf{E}(t)$ is defined following [69] as

$$\begin{aligned}\mathbf{E}(t) &= \mathbf{E}_P(t)\sin(\omega_P t+\phi_P(t)) \\ &\quad+\mathbf{E}_S(t)\sin(\omega_S t+\phi_S(t)) \\ \mathbf{E}_P(t) &= \mathbf{E}_{0,P}\sin\left(\frac{\pi}{2}\frac{t}{\tau}\right),\quad \mathbf{E}_S(t)=\mathbf{E}_{0,S}\cos\left(\frac{\pi}{2}\frac{t}{\tau}\right)\end{aligned} \tag{4.9}$$

where $\mathbf{E}_{0,x}$ is the amplitude vector, $\phi_x(t)$ a time dependent phase (noise) term and ω_x the carrier frequency. The index x distinguishes between either pump (P) or Stokes (S) field. τ is the coupling light pulse duration.

The Feshbach molecule with $m_F = 7/2$ and spin $S = 1$ has nine hyperfine substates, that are listed in Tab. 2.1. Since the nuclear spins factorize everywhere, we can reduce our nuclear basis to only these nine components,as shown in Fig. 4.2. While $\mathcal{G}$ is an angular momentum singlet ($J = 0$), $\mathcal{E}$ is a triplet ($J = 1$) and therefore the maximal size of the basis is $(1+3)\times 9+1 = 37$ states.

From Tab. 2.1, visualized in Fig. 2.5 (B), we see that the largest coupling matrix elements for the pump transition are those involving the $(J,m_J,m_{Na},m_K) = \{(1,0,1/2,-4),(1,1,-1/2,-4),(1,1,-3/2,-3)\}$ spin projections of $|\mathcal{F}\rangle$. If $\Delta = 0$, the dynamics will be dominated by couplings to $m_J = 1$ states in $\mathcal{E}$. With π polarization on the pump field, as will be realized in the experiments discussed in the next section, those are coming from the two $m_J = 1$ projections of $|\mathcal{F}\rangle$ which are indicated with dark blue diamonds in Fig. 4.2. Similarly, using σ^+ on the pump field (the ideal scenario), the nuclear spin projection $m_{Na} = 1/2, m_K = -4$ plays the largest role. In both cases, σ^+ polarization on the Stokes field is optimal.

In the following, we will compare this model to the experimental results.

4.2 Experimental Procedures and Results

Producing ground state polar molecules is a defining mile stone of any ultracold, polar molecule experiment. Achieving it was a team effort of many people over many years in our lab. During this time, we refined our understanding of the molecular structure to develop the multi-level model discussed before, but also our experimental procedures. Ultimately, only the experiment can confirm or challenge our understanding any physical theory. Therefore, this section is dedicated to the experimental tools and techniques and the results, that we obtained by using them.

4.2.1 Sequence

The starting point for the experiments discussed in the following is an ultracold mixture of bosonic ^{23}Na and fermionic ^{40}K atoms trapped in a crossed, far-detuned optical dipole trap (see Chapter 3.2). We prepare $\sim 1.3 \times 10^5$ atoms of each species with a temperature of 0.7 μK. The phase space density of the sample is about 0.5. For more details on the preparation of the mixture, see Chapter 3.1 for a summary and N. Buchheim's thesis [55] for all the details.

Figure 4.3 (A) depicts the key channels in molecule production. For Feshbach association, Sodium is prepared in the $|F,m_F\rangle = |1,1\rangle$ state and potassium in the $|9/2,-7/2\rangle$ state. Then we ramp up the magnetic field to 85.5 G, close to the interspecies Feshbach resonance located at 88 G in the $m_{F,Na} = 1, m_{F,K} = -9/2$ collision channel [64]. With a radio-frequency sweep we flip the potassium atoms into the $m_F = -9/2$ molecular bound state associated with the Feshbach resonance. The efficiency of this process is roughly 10 % and we typically create $\sim$1.1 $\times 10^4$ Feshbach molecules with a binding energy of 80 kHz. For more details on the sweeped Feshbach association, see Chapter 2.2.1.

For STIRAP, we use a 652 nm dye laser (pump transition) and 487 nm diode laser (Stokes transition). Both lasers are locked via their master lasers to the same ultrastable Fabry-Perot reference cavity and have sub-kHz linewidths. The details of the locking schemes can be found in Chapter 3.3. The STIRAP beams co-propagate in a plane perpendicular to the magnetic field axis. In this way we can realize parallel (π) or perpendicular ($\perp \equiv (\sigma^+ + \sigma^-)/\sqrt{2}$) polarization. To perform STIRAP, we use the pulses of Eq. (4.9). After the ground state transfer, we hold the molecules for 90 μs. In this time we remove remaining potassium atoms from the trap using a resonant light field. This has two advantages: First, it improves the lifetime of the molecules when they do not collide with background atoms and second, we obtain a background free STIRAP signal. To understand the latter it is useful to remember that for imaging we bring the ground state molecules back to the Feshbach state with a reversed STI-

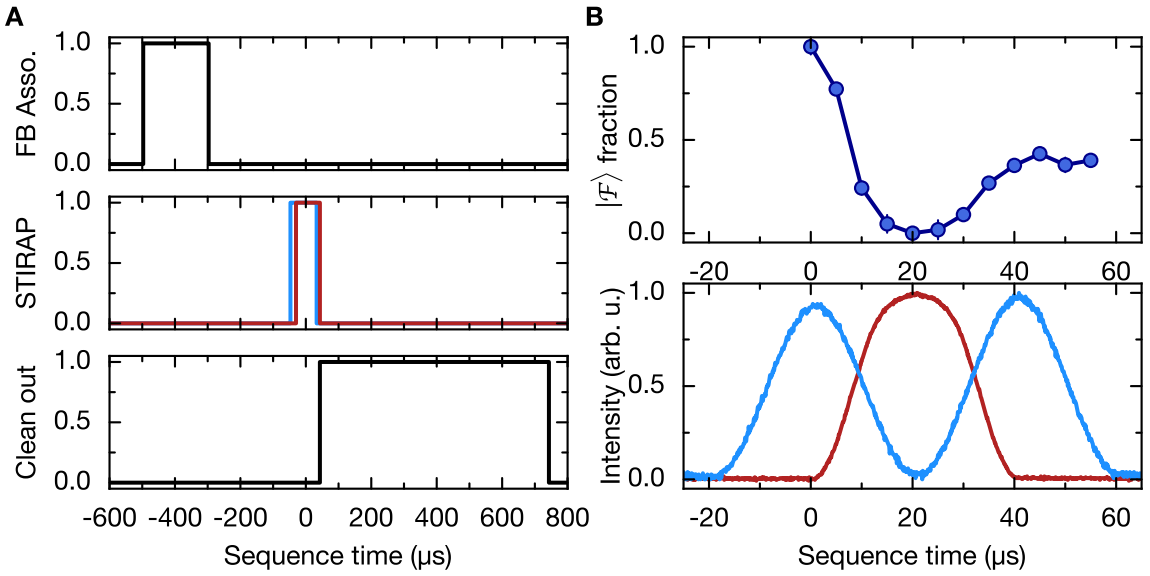

Figure 4.3: *STIRAP sequence. (**A**) Trigger timing of important channels in molecule production. From top to bottom: The RF pulse for Feshbach association, the pump (red) and Stokes (blue) STIRAP pulses and the resonant cleaning pulse for removing potassium atoms. (**B**) Top panel: Evolution of the Feshbach state population throughout a STIRAP process. Here, STIRAP is immediately reversed and no cleaning pulse was used. Bottom panel: Intensity of the pump (red) and Stokes (blue) STIRAP pulses as recorded by a photodiode.*

RAP sequence. This is because there are no cycling transitions for imaging directly involving the ground state. There we can take absorption images with an essentially unchanged cross-section compared to unbound atoms.

So although a full experimental cycle takes about half a minute, as depicted in Fig. 3.2, the part where we produce and experiment with ultracold, polar molecules can be as short as several 100 ms.

In order to confirm that STIRAP actually takes place, we stop at any point in time throughout the sequence and measure the population of the Feshbach state, see Fig. 4.3 (B). Once the “forward" STIRAP is complete, no Feshbach molecules can be observed, because all molecules are in the ground state. However, after the second, “backward" STIRAP, Feshbach molecules, that have been brought back from the ground state, can be detected again. Assuming, that the STIRAP efficiency η is the same in both directions, we obtain η^2 of the initial Feshbach molecules back. In the displayed measurement, $\eta = 63$ %. We also measured the STIRAP pulse shapes by recording their intensity on a photodiode. It is proportional to the square of the Rabi frequency at the place of the molecules. Note, that we recorded the two traces for

pump and Stokes pulses of Fig. 4.3 (B) individually, because we only have one photo diode that normally measures the sum of both pulses.

4.2.2 Rabi Frequency Calibration with EIT

To calibrate the peak Rabi frequencies of the STIRAP beams, we use EIT. As discussed in section 4.1, EIT is based on the same dark state as STIRAP. One difference is the strength of the two coupling lasers: While we aim for equal Rabi frequencies for STIRAP, in EIT the pump beam acts as a weak probe while the Stokes beam is strong. When we scan the pump laser frequency under these conditions, we obtain a typical EIT profile. In the three-level case, this profile is of the form [86]

$$N \propto \exp\left(-t\Omega_P^2 \frac{4\gamma\delta'^2}{|\Omega_S^2 + 2i\delta'(\gamma + 2i\Delta')|^2}\right), \tag{4.10}$$

where t is the EIT pulse duration and γ the excited state line width. Another difference between STIRAP and EIT is, that no smooth pulse shape is required. Thus we simply use square shaped pulses for EIT. However, it is still necessary for the Stokes pulse to precede the pump pulse. Otherwise, Feshbach molecules could be simply resonantly excited.

Figure 4.4 shows an experimentally recorded EIT spectrum (circles), where we kept the Stokes field resonant with the $|\mathcal{F}\rangle \rightarrow |\mathcal{E}, J = 1, m_J = 1\rangle$ transition. Also shown is a fit of Eq. 4.10 (red), where γ, Ω_P and Ω_S are free parameters. From this fit, we directly obtain the peak Stokes Rabi frequency $\Omega_{S,p} = 2\pi \times 8.4$ MHz for 10 mW of power, and $\gamma = 2\pi \times 20$ MHz. The peak pump Rabi frequency needs to be extrapolated from the small pulse amplitude for EIT to the full available pump power. For 100 mW of pump power, we thus expect $\Omega_{P,p} = 2\pi \times 2.6$ MHz. In this experiment, both STIRAP beams had spot sizes of roughly 18 µm. Since we currently do not have more power available on the pump transition, we reduce the Stokes power to match the Rabi frequencies for optimal STIRAP.

How can we use those Rabi frequencies in the multi-level model of section 4.1.2? Since the Stokes matrix elements do not depend on the nuclear spin (see Eq. 4.8) and the transparency peak is much wider than the ground state energy spread (see Fig. 4.2), we can directly use Ω_S as the peak Rabi frequency for all these matrix elements. For the pump transition, we adjust E_P in (4.7) such that

$$\sum_{m_{Na}, m_K} \left|\langle \mathcal{F}|\mathbf{E}\cdot\hat{\mathbf{d}}|\mathcal{E}, J = 1, m_J = 1, m_{Na} m_K\rangle\right|^2 /\hbar^2 = \Omega_P^2. \tag{4.11}$$

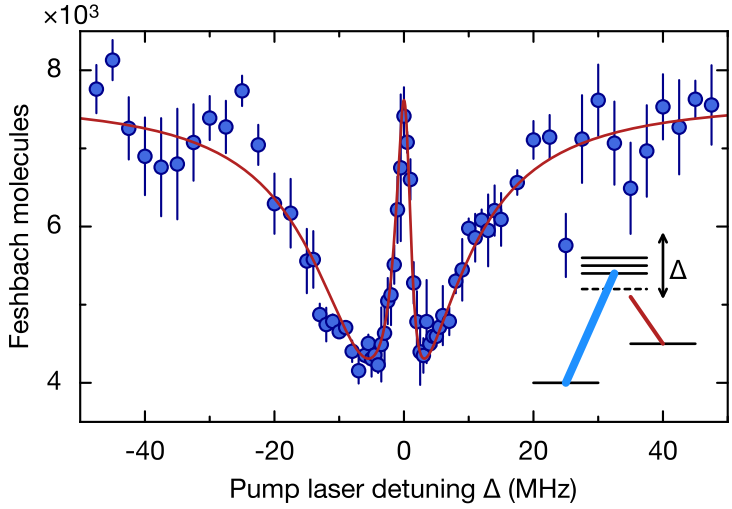

Figure 4.4: *EIT spectrum (circles) as measured in the experiment by scanning the pump laser detuning Δ while keeping the Stokes laser resonant with $m_J = 1$ component of the excited state, $\delta = \Delta$. Error bars denote standard deviations of several experimental runs. The line is a fit using Eq. (4.10). Adapted from [26].*

4.2.3 Ground State Spectra

To observe different HF states in $\mathcal{G}$, we scan the Stokes laser wavelength, effectively changing δ, the two-photon detuning. Ground state spectra recorded with different pump and Stokes beam polarizations are shown in Fig. 4.5.

First, we work with a $\perp$-polarized Stokes field and a π-polarized pump field. In this case, the nuclear spin states in the $m_S = 1$ subspace of $|\mathcal{F}\rangle$ (blue circles) are transferred to the ground state. The largest STIRAP efficiency η is obtained for the $|m_{\mathrm{Na}},m_{\mathrm{K}}\rangle = |{-1}/2,-4\rangle$ hyperfine state at $\delta = 200$ kHz, as expected from the pump transition overlap integrals summarized in Tab. 2.1.

Then, we change the pump beam polarization to $\perp$ as well, so that now pump and Stokes beam are both $\perp$ polarized. This is not ideal, as the total Rabi frequency is now divided between the σ^+ and σ^- branches of the Hamiltonian displayed in Fig. 4.2. Additionally, the σ^--component of the pump beam also couples to levels in the excited state, although with additional detunings due to the Zeeman splitting, which leads to additional loss. Therefore, it is not surprising that the total STIRAP efficiency is reduced in this polarization scheme. Still we can observe, that mainly the $|1/2,-4\rangle$ HF state gets populated, see Fig. 4.5 (red circles), as expected.

The simulated amplitude in both polarization schemes is qualitatively similar to

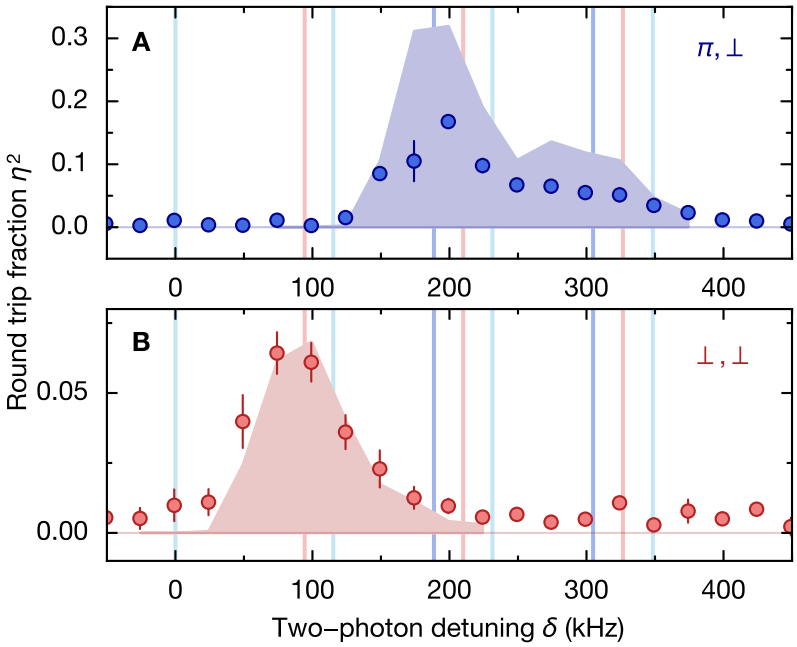

Figure 4.5: *Hyperfine spectra of the rovibronic groundstate. Blue (red) circles denote data recorded with $\pi(\perp)$-pump polarization in panel **A** (**B**), the Stokes beam is always $\perp$-polarized. Error bars, denoting standard error of the mean of several experimental runs, are mostly smaller than the symbol size. Vertical lines indicate the expected positions of the hyperfine levels with $m_F = -5/2$ (light blue), $-7/2$ (red) $-9/2$ (dark blue), same color convention as in Fig. 4.2. Simulation results for the two polarization scenarios are indicated by the shaded areas. The experimentally measured phase noise was included (see text for details). Both spectra were recorded at $\Delta = 100$ MHz and using 70 µs STIRAP pulse durations. The data of panel (A) is the same as in Fig. 2.6 (B).*

the experimental results. In the $\perp$ / $\perp$ scheme, it even accurately matches the experimental observation, but it is systematically to large in the π/ $\perp$ case. While we did not investigate this discrepancy in detail, possible reasons might be imperfections in the π-polarization of the pump laser, faster loss of molecules at higher densities (see section 4.3) or a mismatch between the experimentally achieved Feshbach molecule binding energy and the one used in the CC calculation.

In all these measurements, we have worked with a large one-photon detuning of $\Delta = 100$ MHz (pulse duration $\tau = 70$ µs) with respect to the $m_J = 1$ component of the excited state. This might be surprising, as previous STIRAP transfer for polar molecule production has been achieved with very small one-photon detunings. However, our situation is different due to the non-resolved hyperfine structure of the interme-

diate state. In the next section, we therefore experiment with one-photon detunings and pulse durations to find the best multi-level STIRAP pathway.

4.2.4 STIRAP Efficiency Over One-Photon Detuning

In the ideal three-level STIRAP, the one-photon detuning Δ does not play a role for the transfer efficiency, as long as the two-photon resonance condition $\delta = 0$ is fulfilled. In multi-level STIRAP, where degenerate components in the intermediate state are inevitably addressed with the pump beam, but for which $\delta = 0$ is not fulfilled, Δ is the key to success. This is because scattering from the unwanted components decreases as $1/\Delta^2$, while two-photon coupling only decreases as $1/\Delta$ and the latter can, to some extend, be compensated with longer pulse durations. Therefore, let us try STIRAP with large one-photon detunings Δ.

To optimize the STIRAP process experimentally, we investigate the transfer efficiency η to the $|^{-1}/_2, -4\rangle$ HF ground state, using the $\pi/\perp$-polarization scheme. While assuring two-photon resonance $\delta = 0$, we measure η for different one-photon detunings Δ. Also the pulse duration τ is optimized for each value of Δ. The results are shown in Fig. 4.6 (A) (blue circles). We find that the efficiency is 25% for one-photon resonant STIRAP, but rises up to ~40% for detunings larger than 20 MHz, where it then saturates.

Also shown is the result of the parameter free model calculation (dashed dark blue line) for optimal pulse duration, but neglecting noise. This ideal model predicts a significantly larger efficiency than the one observed in the experiment. However, when we include a realistic phase noise function $\phi_x(t)$ into the model, we can resolve this discrepancy: In order to do so, we apply a random $\phi_x(t)$ that reproduces the measured beat note radio-frequency spectrum between each STIRAP laser to their respective master laser. The phase noise power spectrum of Fig. 3.6 has a bandwidth of about 2.5 MHz and a magnitude that yields an rms amplitude $\phi_{x,\mathrm{rms}} = 400$ mrad. This noise function is multiplied by a factor $\sqrt{2}$, assuming the phase noise of the master laser to the cavity lock is the same as the phase noise of the slave laser to the master lock. Including the laser phase noise spectra into the model calculation leads to the solid dark blue line, that matches the data fairly well. By comparing the model calculations with and without phase noise, it can be seen that its influence on the molecule production is strongest close to resonance and becomes less prominent for larger Δ.

Fig. 4.6 (B) shows the optimal STIRAP pulse durations τ, both obtained from the experiment (circles) and the model including phase noise (solid line). Also in this case, the model describes accurately what we observe. At large Δ, experimentally optimal pulse durations are shorter. This indicates, that for the resulting reduced effective

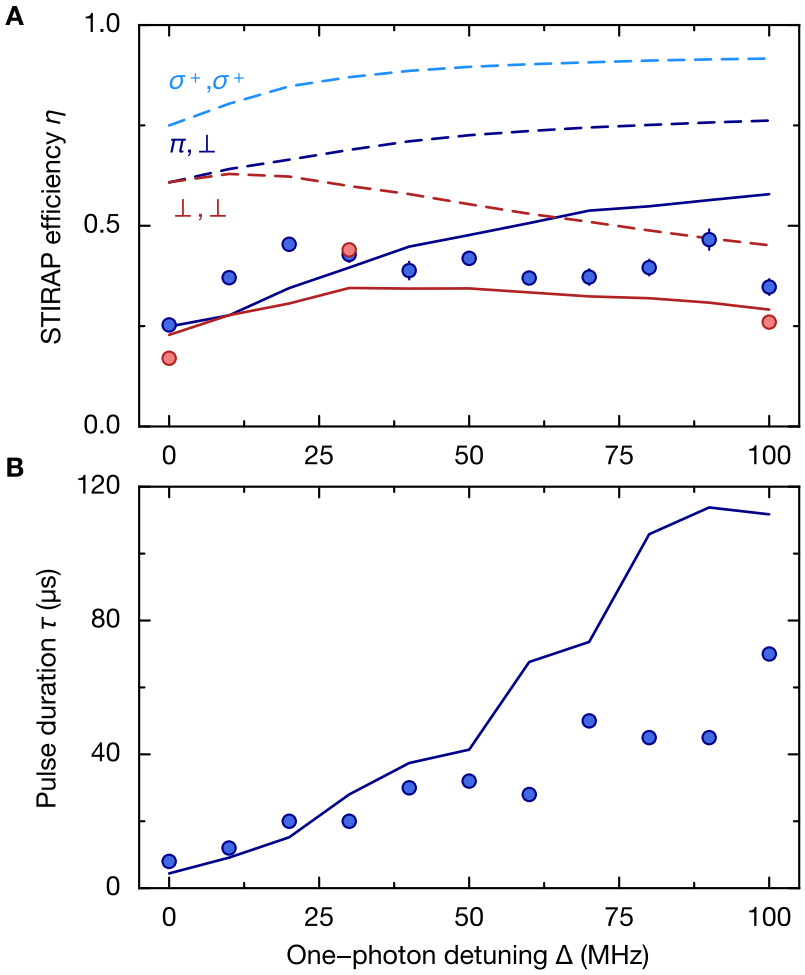

Figure 4.6: *STIRAP at different one-photon detunings. (**A**) The measured STIRAP efficiency (circles) increases initially and then saturates. Model results with phase noise (solid lines, averaged over 12 simulations) and without phase noise (dashed lines) are also shown. As before, color encodes the different polarization scenarios. Dark blue (red) denotes $\pi(\perp)$-pump polarization, the Stokes beam is always $\perp$-polarized. Light blue refers to the experimentally not realized case of σ^+ polarization for both pump and Stokes laser. (**B**) Optimal STIRAP duration τ as determined for each Δ for the $\pi/\perp$ situation. Data (circles) with model prediction including phase noise (solid line). Error bars denote the standard error of the mean and are mostly smaller than the symbol size.*

two-photon coupling and longer pulses other noise sources may become important, that have not been considered in the model.

This can also explain the larger predicted efficiencies at large Δ compared to the experimentally observed ones. However, both the observed efficiency and the ideal STIRAP pulse duration agree very well for small Δ.

We can also compare the HF spectra of Fig. 4.5 with our model: Using experimental parameters, including phase noise, the modeled spectra match. Only the amplitude for the $\pi/\ \perp$ case is systematically too large. However, this is most likely also due to the large detuning discrepancy, as the ground state spectra were recorded with $\Delta = 100$ MHz.

To further benchmark the accuracy of the model calculation, we also study ideal STIRAP parameters in the second polarization scenario, where pump and Stokes beam are both $\perp$ polarized for a few selected detunings. The corresponding efficiency measurements are indicated with the red circles in Fig. 4.6 (A). And also in this case, detuned STIRAP is favorable compared to resonant STIRAP. The agreement between experiment and model calculation is equally good as in the first polarization scheme.

There is one polarization scheme, that is superior to both schemes that we could try experimentally. It requires σ^+/σ^+ polarized pump/Stokes beams. Due to geometrical constraints in the experimental apparatus, this ideal scheme could not yet be implemented. But we can simulate it using the multi-level model, that we have now experimentally verified. The ideal scenario also addresses the $|1/2, -4\rangle$ ground state and, according to the simulation, should yield the highest transfer efficiencies (light blue line in Fig. 4.5 (A)). To obtain higher STIRAP efficiencies, it would therefore be very promising to consider sending the STIRAP beams also along the z-direction into the glass cell, when the next iteration of the z-lattice and high-resolution imaging setups are planned.

4.3 Lifetime of Ground State Molecules

With the STIRAP scheme outline above we can routinely produce quantum gases with about 5000 fermionic ground-state molecules. So what happens to the molecules in the crossed dipole trap after STIRAP? To find out, we observe the loss of molecules over time, as displayed in Fig. 4.7 (A). We find that a two-body loss model describes well what we observe. In such a model, the loss can be described in terms of the molecular density n as

$$\frac{dn}{dt} = -\beta n^2 \tag{4.12}$$

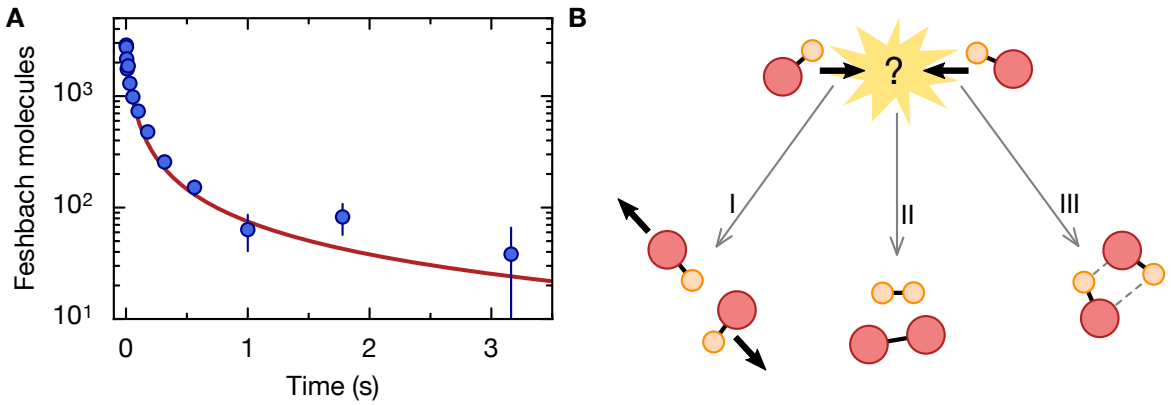

Figure 4.7: *(**A**) Loss of molecules in the crossed, far-detuned optical dipole trap. A two-body loss function (red) describes the observation best. The two-body loss coefficient is* $\beta = 7.3 \times 10^{-11}$ cm^3/s *at a temperature of 600 nK. (**B**) Several possible outcomes of two-body collisions. In an elastic collision (I), the molecules scatter, but remain intact. If an inelastic collisions (II and III) occurs, what happens depends on the molecule. For some molecules, a chemical reaction (II) is energetically favorable. For the other molecules, such as* $^{23}Na^{40}K$*, long-lived collision complexes may form (III).*

where β is the two-body loss coefficient [29]. To fit the molecular loss, we use

$$N(t) = \frac{N_0}{1 + n_0 \beta t}, \tag{4.13}$$

where N_0 and n_0 denote the initial molecule number and density.

The density in a 1D-harmonic trap along the x-direction can be calculated from the trapping potential $V(x) = m\omega^2 x^2/2$, where m denotes the mass of the molecule and ω is the trapping frequency. We can the calculate the density as

$$n(x) = N_0 \frac{\exp(-V(x)/k_B T)}{\int_{-\infty}^{\infty} \exp(-V(x)/k_B T) dx}, \tag{4.14}$$

where N_0 is the initial molecule number, k_B denotes Boltzmann's constant and T is the temperature of the molecular gas, which we determine in a time-of-flight expansion measurement of the gas as $T = 600$ nK. To obtain the peak density at the center of the cloud, we evaluate Eq. 4.14 at the center, $x = 0$, and obtain

$$n_0 = N_0 \frac{\sqrt{m}\omega}{\sqrt{2\pi T k_B}}. \tag{4.15}$$

Generalizing this to 3D gives

$$n_0 = N_0 \frac{\sqrt[3]{m}\omega_x\omega_y\omega_z}{\sqrt[3]{2\pi T k_B}}, \tag{4.16}$$

where ω_x, ω_y and ω_z denote the trapping frequencies along the x, y and z-direction. Using an average trapping frequency of $\bar{\omega} = 2\pi \times 202$ Hz we arrive at an initial molecular density of 5.2×10^{11} cm^{-3} for the data set in Fig. 4.7 (A). Thus, the two-body loss coefficient in this measurement is 7.3×10^{-11} cm^3/s.

Interestingly, this is about 5 times larger than $\beta = 1.5 \times 10^{-11}$ cm^3/s reported in [24], also for ^{23}Na^{40}K, but in the hyperfine ground state $|m_{\mathrm{Na}}, m_{\mathrm{K}}\rangle = |3/2, -4\rangle$. Whether this is due to the different hyperfine states used or due to errors in the density or temperature calibration remains to be checked.

So what happens, if two molecules collide? Three scenarios are illustrated in Fig. 4.7 (B). The first option is an elastic collision. For identical fermionic molecules with a sufficiently high p-wave barrier this is the most likely option. However, also inelastic processes can play a role. While reactions of the kind $2AB \rightarrow A^2B + B$ or $A + AB^2$ are energetically forbidden for singlet alkali-metal dimers near the potential minimum, reactions of the form $AB + AB \rightarrow A^2 + B^2$ are energetically favorable for a few molecules [90], among them ^{40}K^{87}Rb [91, 92]. In ^{23}Na^{40}K this reaction is, however, endothermic and can not occur at ultracold temperatures, so that ^{23}Na^{40}K is frequently referred to as a *chemically stable* molecule. Recently, however, more and more bi-alkaline polar molecule experiments published their loss measurements and it became apparent, that also the presumably stable molecules exhibit significant two-body losses, comparable to the one observed in the reactive molecules. Especially beautifully, this was demonstrated in ^{23}Na^{87}Rb [38]. In ^{23}Na^{87}Rb, the ground state is chemically stable, but the first excited rotational state is not. Although for Feshbach and thus non-polar molecules, all reactants and products could be measured [93]. Like that, the loss rates with and without reactive channels could be compared within the same experiment and were found to be essentially the same. Thus, there must be another inelastic two-body loss channel for the stable molecules. One idea is that long-lived complexes form. These complexes are, in the case of chemically stable molecules, not properly bound states: Instead, a collision of two molecules could be *sticky*, meaning that the two molecules are bound together only temporarily [94]. This temporal binding is due to the large density of states of the two-molecule collision and is long compared to typical experimental time scales.

Although these ideas seem plausible, what really happens remains so far unknown. Theoretically, it is very challenging to calculate spectra of complexes with as many as four atoms and without having any spectral information, hunting the complexes down experimentally seems almost impossible. Apart from shedding more light on these seemingly simple collisional processes, understanding this loss might also enable one to circumvent it. Then, long-imagined goals like observing dipolar crystallization [95] might come finally come true.

Meanwhile, however, one can also prevent this loss by confining the molecules

to the sites of an optical lattice. This approach also has the additional benefit of improving the Feshbach association fraction, the dominant source of loss of phase space density.

Chapter 5

Spin-Decoupled Magic Trapping

Among the many degrees of freedom that polar molecules posses, the rotational one is particularly appealing: Superpositions of rotational states can be readily addressed using microwave (MW) radiation and give rise to strong, long-range dipolar interactions. Due to their opposite parity, however, these states can have very different polarizabilities and thus experience very different trapping conditions in an optical dipole trap. The resulting dephasing of the superposition limits its usefulness for quantum simulation. To remedy this, a *magic* trap can be used, the concept of which will be introduced in Section 5.1. Section 5.2 contains our results in realizing a spin-decoupled magic trap using a magic polarization angle and a small dc electric field, which aids in the decoupling of the nuclear spins to get even closer to the ideal of identical trapping conditions for two rotational states in polar molecules. This chapter is based on publication [36].

5.1 A Magic Trap

In this section, we start with a brief look on the working mechanisms of dipole traps. We find that the exact trapping potential for any atom or molecule depends on the state it is in. Consequently, working with a superposition of two states, we want both states to have the same trapping potential to achieve optimal coherence times by preventing dephasing. We will see how these types of *magic* traps can be realized, before we finally look specifically at magic angle traps and nuclear spin decoupling for polar molecules.

5.1.1 The Dipole Force

Keeping an object of interest in a well defined position is usually a key requirement in any scientific study. In the case of quantum gases, this is usually achieved using far-detuned optical dipole traps, some specific realizations of which have been introduced already in Section 3.2. This class of dipole traps is so popular, because it allows any trap shape that is possible by superimposing arbitrarily many trap laser beams:

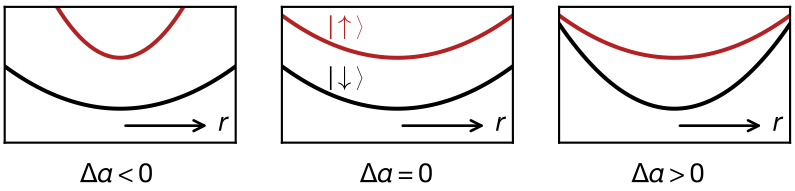

Figure 5.1: *Schematic of trapping potentials for two states, e.g. rotational ones, $|\downarrow\rangle$ (black) or $|\uparrow\rangle$ (red). If the differential polarizability $\Delta\alpha = \alpha_{|\downarrow\rangle} - \alpha_{|\uparrow\rangle} = 0$, a magic trap has been realized (central panel). The transition frequency between $|\downarrow\rangle$ and $|\uparrow\rangle$ then becomes independent of position. Normally, however, the potentials for the two states differ (left and right panels). Adapted from [36].*

From a simple single beam trap [96] as our transport trap to optical lattices in various geometries [5].

As their name suggests, these traps work due to the dipole force

$$\mathbf{F}_{\text{dip}} = \frac{1}{2}\alpha(\omega_L,\varepsilon)\nabla[|\mathbf{E}(\mathbf{r})|^2], \tag{5.1}$$

where α denotes the polarizability, which depends on the trap laser angular frequency ω_L and polarization ε. $|\mathbf{E}(\mathbf{r})|^2$ denotes the spatially varying trap intensity with $\mathbf{r}$ being the position. All optical traps in this thesis are generated by laser beams with a Gaussian intensity profile.

When we now create a superposition of two rotational states $|\uparrow\rangle$ and $|\downarrow\rangle$ of the molecules in our trap, their trapping potentials generally are not the same, see left and right panels of Fig. 5.1. If one now drove transitions between the two states, the excitation would quickly dephase: Since the transition frequency depends on the position of the moving molecule in the trap and because the excitation only has a certain linewidth, it can only be resonant with some part of the cloud at a time while being detuned for the other.

To prevent dephasing, we need *magic* trapping conditions, in which both states have the same polarizability (central panel). This can be achieved by tuning the trapping force by changing the polarizability α. Then the transition frequency between the states becomes independent of the position in the trap, r. Therefore state-insensitive, so-called magic trapping conditions for pairs of internal states are very valuable for precision measurements or quantum computation.

A beautiful example is the realization of a magic wavelength trap for an optical lattice clock of strontium [97]. In this case, two scalar electronic states with angular

momentum quantum number $J = 0$ could be employed, so that the polarizability only depends on the wavelength, but not on the polarizability.

In the next sections, we will look at ways to achieve magic trapping conditions for rotational states in polar molecules.

5.1.2 Magic Traps for Polar Molecules

Because of its large oscillating transition dipole moment, we want to create a magic trap for the superposition of the $J = 0$ and $J = 1$ rotational states in our ^{23}Na^{40}K molecules. Therefore, let us recall the Hamiltonian describing molecules in their rovibronic ground state, Eq. 2.15 in Section 2.3,

$$\mathcal{H} = \mathcal{H}_0 + \mathcal{H}_{ac} + \mathcal{H}_{\text{opt}} + \mathcal{H}_{hf}, \tag{5.2}$$

where $\mathcal{H}_0$ describes the molecule as a rigid rotor coupled to a dc electric field, $\mathcal{H}_{ac}$ describes the effect of a microwave field driving a rotational transition, $\mathcal{H}_{\text{opt}}$ is the trap light contribution and $\mathcal{H}_{hf}$ describes the hyperfine structure.

In our experiments, we prepare all molecules in one of the 36 hyperfine states. As shown in Fig. 2.8, this state in the $J = 0$ manifold can then be coupled to the first excited rotational manifold $|1,(0,\pm 1)\rangle$ via MW radiation with a frequency of $2B_{\text{rot}}/h \approx 5.6$ GHz [31], where B_{rot} denotes the rotational constant. However, due to the interactions and cross couplings in the above Hamiltonian hyperfine states in the excited state get mixed. The nuclear spins in the $J = 1$ manifold and the rotation predominantly couple via the nuclear electric quadrupole moment in $\mathcal{H}_{hf}$, while the trapping light field couples different m_J states in $\mathcal{H}_{\text{opt}}$ [33, 76].

Figure 5.2 (A) shows a theoretically calculated AC Stark map of the rotational excitation spectrum for the $|J,m_J,m_{I,\text{Na}},m_{I,\text{K}}\rangle = |0,0,-1/2,-4\rangle$ hyperfine state in ^{23}Na^{40}K, where the electric field strength is negligible. The strengths of the transitions are color coded. In order to model the energies of all relevant rotational hyperfine levels in various external field set-ups, we follow the formalism of Ref. [98] and references therein. We evaluate the effective Hamiltonian, which includes interactions from rotation, hyperfine, Zeeman, ac and dc Stark effects, in the zero-field rotational hyperfine basis with $J = 0$ to 3. It is then diagonalized to obtain the eigenenergies and eigenvectors at various external field settings. The same set of parameters to describe various interactions are used as in Ref. [98] except dynamic polarizabilities at 1550 nm derived from experimental results, see Section 5.2.3. Frank-Condon overlaps calculated from the eigenvectors are used as transition probabilities.

The dependence of the transition frequency ν on the light intensity I, the polariza-

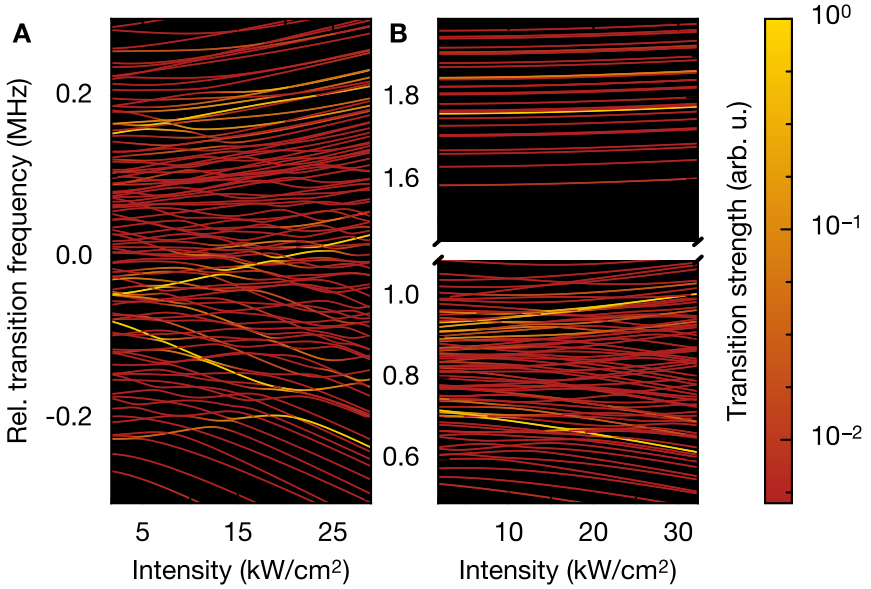

Figure 5.2: *Theoretically calculated ac-Stark maps of $^{23}Na^{40}K$ in a 1550 nm trap for the $J = 0 \rightarrow J = 1$ transition, where the $J = 0$ molecules were prepared in the $|m_{\mathrm{Na}},m_{\mathrm{K}}\rangle = |-1/2,-4\rangle$ state. The color of the lines encodes the transition strength down to values of 5×10^{-3}. For clarity, all transitions with lower strengths are colored in the same darkest nuance of red. (**A**) ac Stark map at negligible static electric field. A complex structure with many avoided crossings arises. (**B**) ac Stark map at $E = 101.3$ V/cm at the magic angle. The Stark shift separates the $m_J = 0$ component (top panel) from the $|m_J = 1|$ components (lower panel). The transitions of $m_J = 0$ become almost independent of the trap intensity.*

tion angle ϕ, and the electric field E can be approximated by

$$\Delta\nu = \nu - \nu_0 = \frac{1}{h}[\Delta\alpha(\phi)I + \beta(E,\phi)I^2 + \mathcal{O}(I^3)], \tag{5.3}$$

where ν_0 denotes a transition frequency at $I = 0$, $\Delta\alpha = \alpha_{|\downarrow\rangle} - \alpha_{|\uparrow\rangle}$ is the differential polarizability, and β is the hyperpolarizability of $J = 1$ as $\beta \approx 0$ for $J = 0$.

In Fig. 5.2, many hyperfine states and avoided crossings between them are visible. But even these can be used to realize a spin-independent trap, as has been shown in [33, 76] for $^{87}Rb^{133}Cs$ molecules: At the center of an avoided crossing, the slope of the transition frequency, which is, to first order, the differential polarizability $\Delta\alpha$, is zero. When the trap intensity was set to this value, the coherence time could be improved up to 0.75 ms [33].

Alternatively, one could modify $\Delta\alpha$ of Eq. 5.3 by changing the polarization of the rotational $J = 1$ state. Since, in contrast to the $J = 0$ state, the excited $J = 1$ is not

a scalar state, in principle both the wavelength and the polarization of the trap light can be used to create a magic trap. However, due to the many additional states in molecules compared to atoms, it is impossible to find magic wavelengths at large enough detunings for negligible off-resonant light coupling. However, adjusting the polarization of the trap laser is a good alternative [99]. If the excited rotational state is tuned to the same polarizability as the ground state, we call the angle between the polarization vector and the quantization axis a *magic angle*, θ_m. Typically, the magnetic or dc electric field direction is chosen as quantization axis. Since the polarizability is a rank-2 tensor, the magic angle is given by [99]

$$\cos^2 \theta_m = \frac{1}{3}, \tag{5.4}$$

where $\theta_m \approx 54^\circ$ follows. The first experiment realizing a magic angle trap [100] for ^{40}K^{87}Rb molecules, in which a quantization axis along the magnetic field direction was chosen, reported a 10-fold increase of coherence time to 1.5 ms, when the magic condition was fulfilled.

This coherence time is limited due to the strong mixing of the hyperfine levels, which prevent equal trapping potentials, even when the first-order differential light shift is cancelled [33, 99, 100]. Then, rotational states can still rapidly dephase in an inhomogeneous optical trap due to higher order terms. To leading order this is the hyperpolarizability β, which describes the intensity dependence of the molecular polarizability in Eq. 5.3. It originates from the coupling between rotation, nuclear spins and the trapping light field. In the next Section, we will see how this coupling can be reduced.

5.1.3 Nuclear Spin Decoupling

In order to avoid frequent state crossings, it is helpful to increase the energy difference between the states. This can be achieved with large magnetic [101] or electric fields [98], which have both been suggested to further simplify the polarizabilities of the involved states. Electric fields are particularly appealing, since polar molecule experiments usually already have electrodes in place for the polarization of the molecules. The Stark shift of the excited rotational state depends on $|m_J|$. Thus the only non-degenerate states in an external field are the sub-states with $m_J = 0$.

However, applying large electric fields of a few kV/cm is a challenging task: The larger the dc electric field, the larger the dipole moment of the molecule and, consequently, the larger the linear Stark shift due to field fluctuations. Therefore, the stability requirements on the electric field get harder and harder to fulfill. Luckily, the dc Stark shift dominates all other interactions already at tiny values – 60 V/cm in ^{23}Na^{40}K– which are readily available in the lab. Already at this electric field, nuclear

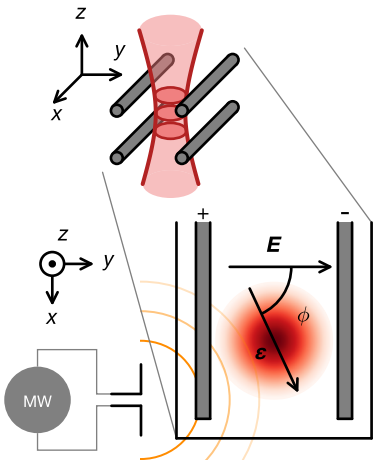

Figure 5.3: *Schematic of the experimental setup. Molecules are confined to several pancake traps (red) in the $x-y$-plane, formed by a 1D optical lattice along the z-axis with polarization vector ε. Four in-vacuum rod electrodes (grey bars) generate DC electric fields along the y-axis. The angle ϕ between $\boldsymbol{\epsilon}$ and $\boldsymbol{E}$ can be used to adjust the first order differential AC Stark shift between rotational states. A MW dipole antenna supplies the MW photons for the rotational transitions. Adapted from [36].*

spins and rotation uncouple for the $|J,m_J\rangle = |1,0\rangle$ states, thus simplifying the ac Stark map. Further, also the rotation is decoupled from the light field, so that the curvature of the transition frequencies reduces. Figure 5.2 (B) shows the theoretically calculated spectrum for $E = 101.3$ V/cm and at the magic angle. While avoided crossings are reduced all over the Stark map, there is not a single one left in the $m_J = 0$-component. Additionally, the transition strength is also conveniently concentrated into individual states.

5.2 Experimental Procedures and Results

In this section, we will first discuss the experimental setup that we then use to create and characterize our magic angle trap.

5.2.1 Setup

The experiments begin with the preparation of ultracold ^{23}Na^{40}K molecules in the rovibronic ground state at 300 nK. Initially, the molecules are in the $|J,m_J,m_{I,\mathrm{Na}},m_{I,\mathrm{K}}\rangle = |0,0,-1/2,-4\rangle$ hyperfine state which will be referred to as the ground state $|\downarrow\rangle$. Here, m_I denotes the projections of the nuclear spins $I_{\mathrm{Na}} = 3/2$ [102] and $I_{\mathrm{K}} = 4$ [103] onto the electric field axis. We make molecules similarly as outlined in Chapter 4, but instead of creating the molecules in the crossed dipole trap, we first load the atomic mixture to several pancake-shaped traps created by a one-dimensional (1D) lattice, see Fig. 5.3. The lattice is generated by a single, linearly polarized 1550 nm retro-reflected laser beam that propagates along the z axis. This is

also the direction of the 86 G magnetic field required for the subsequent Feshbach molecule association. The Feshbach molecules in the lattice planes are then transferred to the rovibronic ground state using STIRAP. The polarization of the lattice beam can be adjusted manually with a half-wave plate within an uncertainty of 0.5 degrees.

We apply a dc electric field along the y axis, so that we can adjust the magic angle between lattice polarization and electric field direction. The corresponding voltages are applied to four in-vacuum rod electrodes. Further, eight additional auxiliary electrodes compensate residual electric field gradients to below 0.5 V/cm^2, see Section 3.4 for details on the electric field setup. To drive the rotational transitions we further use a MW dipole antenna, that is mounted close to the glass cell.

5.2.2 ac Stark Maps

In our first experiment, we want to get a first-hand glance on the ac-Stark maps of the $J = 0 \rightarrow J = 1$ transition of Fig. 5.2. We therefore perform MW loss spectroscopy at two electric field strengths, see right panels in Fig. 5.4. To ensure identical starting conditions for all data points, the preparation of molecules is always performed at the same lattice intensity, which is then ramped quickly to the respective spectroscopy intensity shortly before the MW sweep (see Fig. 3.4). Afterwards the lattice is ramped back and the remaining $J = 0$ molecules are detected. The MW loss spectroscopy spectra were recorded as follows: In order to couple to states with different transition strengths while maintaining good spectral resolution, we swept the MW frequency across 10 kHz in 1.15 ms, symmetrically around the central transition frequency ν. We adjusted the MW power such that the Rabi frequency for the strongest transition was about 4.0 kHz. Whenever a reduction in $|\downarrow\rangle$ molecules is detected, it is assumed that a transition to $J = 1$ has occurred.

Figure 5.4 shows our experimental results (right panels) together with the the theoretically expected frequency and strengths for each MW transition (left panels). In this figure, only transitions with strengths larger than 0.5% are displayed for clarity in the left panels.

In the presence of an electric field $E = 101.3$ V/cm, see Fig. 5.4 (B), the $m_J = 0$ states separate from the nearly degenerate $m_J = \pm 1$ states due to the dc Stark splitting. Simultaneously, the polarization of the lattice beam is set to the magic angle with respect to the static field $\boldsymbol{E}$, thereby realizing a spin-decoupled magic trap.

Both with small or large electric field, the agreement between experiment and theory is excellent. In the following, we focus on $|\uparrow\rangle$, the hyperfine state of $J = 1$, $m_J = 0$ with the largest transition strength (indicated by the orange arrow in Fig. 5.4).

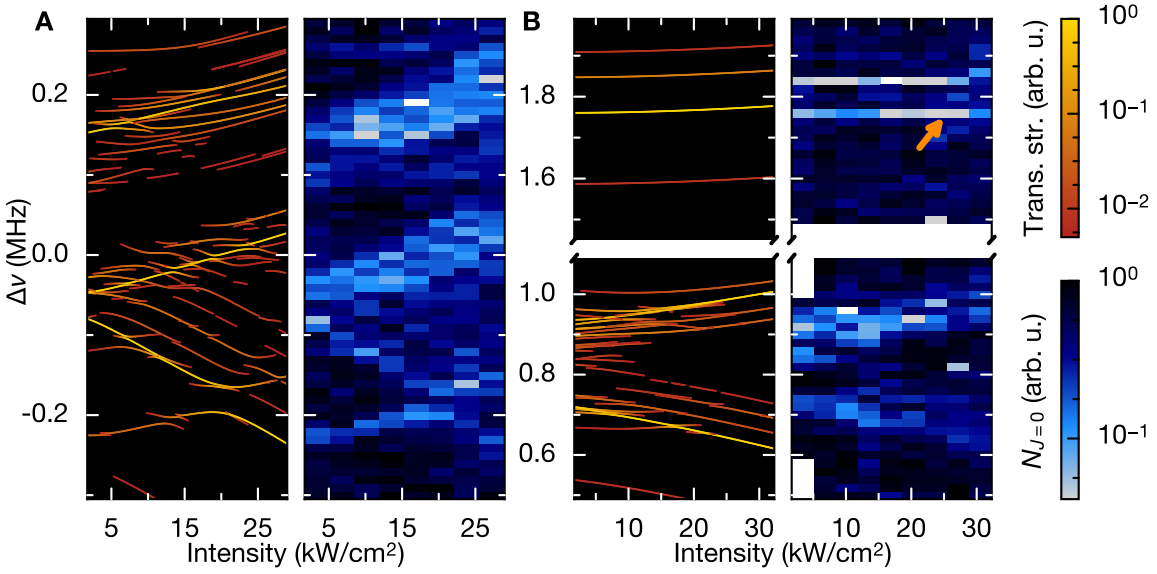

Figure 5.4: *AC Stark maps of the $J = 0$ to $J = 1$ transition manifold for two electric field strengths. (**A**) E =8.8 V/cm. Left panel: transition frequencies from $|\downarrow\rangle$ state to the $J = 1$ manifold for various light intensities. The normalized transition strengths are encoded by line color. Only transitions stronger than 0.5% are shown for clarity. Right panel: molecule loss spectroscopy. The molecule number remaining in $|\downarrow\rangle$ after a MW sweep is recorded (blue). (**B**) E =101.3 V/cm and under magic trapping condition. The $m_J = 0$ component (upper panel) is separated from the $m_J = \pm 1$ components (lower panel) by a DC Stark shift. Consequently the hyperfine structure of the $m_J = 0$ manifold is simplified to two strong lines. Their transition frequency is almost independent of intensity. The arrow denotes the $|\uparrow\rangle$ state that will be used in the following. Theoretical (experimental) data in both subfigures is normalized to the same maximal transition matrix element (detected atom number). Adapted from [36].*

5.2.3 Polarizability and Hyperpolarizability

Ground State Polarizability

Due to their narrow STIRAP linewidth, ground state molecules are an excellent probe to precisely determine their polarizability and thus to calibrate the lattice intensity. We first measure the ac Stark shift of the rotational ground state in terms of the lattice intensity I, as shown in Fig. 5.5 (**A**). The observed relationship between the STIRAP two-photon detuning δ and I is linear. To determine the maximum intensity of the lattice I_0, we further need the polarizability of the ground state, $\alpha_{|\downarrow\rangle}$.

We do that with parametric heating measurements [53, 76, 100, 104]. We modulate

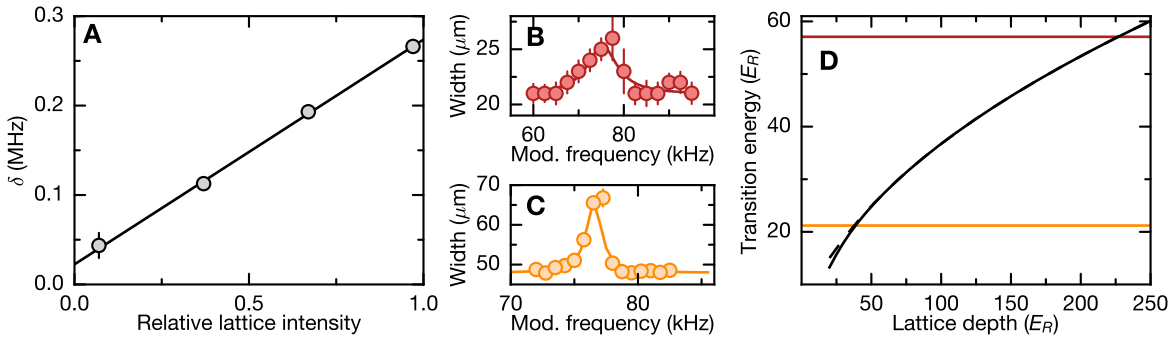

Figure 5.5: *Lattice intensity calibration. (**A**) Differential AC Stark shift between $|\downarrow\rangle$ and Feshbach molecular state measured as STIRAP two-photon detuning δ for different lattice intensities. Circles denote the center frequencies of Lorentzian fits to the spectra recorded at each intensity, error bars are derived from the covariance matrix of the fit. The line is a linear fit to the center frequencies. Parametric heating expansion measurement for $^{23}Na^{40}K$ molecules (**B**) and Na atoms (**C**). Lines in (**B**) and (**C**) are Lorentzian fits to the data. (**D**) Normalized transition frequency $f_{0\to2}$ as a function of the lattice depth when the quasi-momentum $q = 0$ (black solid line) and $q = \hbar k$ (black dashed line), where $\hbar k$ is the recoil momentum of the lattice. The red (orange) line denotes the measured transition frequency of the molecules (Na atoms).*

the lattice depths V_{lat} of molecules and sodium atoms, which are related via

$$\alpha_{|\downarrow\rangle} = \frac{V_{\text{lat}}^{\text{NaK}}}{V_{\text{lat}}^{\text{Na}}}\alpha_{\text{Na}}. \tag{5.5}$$

where the subscripts distinguish between atoms or molecules. The atomic polarizability $\alpha_{\text{Na}} = h \times 9.0$ Hz/(W/cm^2) [105] in a 1550 nm trap is known. The lattice intensity is typically modulated by 2.5% for 8 ms. Then the molecules (atoms) are released from the lattice and the cloud radius along z-direction is recorded, see Fig. 5.5 (**B**) and (**C**). Parametric heating occurs, when the modulation frequency is equal to the transition frequency from the ground band to the second excited band, $f_{0\to2}$. We numerically solve the band structure of the optical lattice and obtain $f_{0\to2}$ as a function of the lattice depth, as shown in 5.5 (**D**). From our measurements we obtain $f_{0\to2}^{\text{Na}} = 76.5(2)$ kHz and $f_{0\to2}^{\text{NaK}} = 75.2(8)$ kHz.

The corresponding lattice depth is 38.6(2) E_R^{Na} for sodium atoms and 226(4) E_R^{NaK} for ^{23}Na^{40}K molecules respectively, where $E_R^{\text{Na}} = h \times 3.612$ kHz and $E_R^{\text{NaK}} = h \times 1.319$ kHz are the recoil energies of sodium atoms and ^{23}Na^{40}K molecules respectively. We obtain $\alpha_{|\downarrow\rangle} = h \times 19.3(4)$ Hz/(W/cm^2), which agrees well with the theoretical *ab initio* value $\alpha_{|\downarrow\rangle}^{\text{theory}} = h \times 20.4$ Hz/(W/cm^2).

The differential Stark shift slope of $251(4)$ kHz$/I_0$ amounts to the effective polarizability α_{eff}, the difference between polarizabilities of the initial Feshbach molecular state $|FB\rangle$ and the rovibronic ground state $|\downarrow\rangle$, which is given by

$$\alpha_{\text{eff}} = \alpha_{FB} - \alpha_{|\downarrow\rangle} = \alpha_{\text{Na}} + \alpha_{\text{K}} - \alpha_{|\downarrow\rangle}. \tag{5.6}$$

The polarizability of Feshbach molecules α_{FB} is well approximated by the sum of the polarizabilities of the constituent sodium and potassium atoms, α_{Na} and α_{K}. Then we can calculate α_{eff} according to Eq. 5.6 and determine the maximum lattice intensity to be $I_0 = 34(2)$ kW/cm^2.

Excited State Polarizability and Hyperpolarizability

To characterize the magic angle for the $|\downarrow\rangle \rightarrow |\uparrow\rangle$ transition, we perform π-pulse loss spectroscopy at $E = 144.3$ V/cm, see Fig. 5.6. For each angle ϕ, we record rotational transition spectra for various intensities. We then extract the center frequencies ν with a Lorentzian fit. The results of these measurements are depicted in Fig. 5.6 (A). From the slopes we get the differential polarizabilities plotted in (B), which agree well with the theory (red line). The magic condition $\Delta\alpha = 0$ occurs for $\phi = 54.0(5)^\circ$.

We can now use the experimentally determined isotropic polarizability at 1550 nm, $\alpha_{\text{iso}} = (2\alpha_\perp + \alpha_\parallel)/3 = h \times 19.3$ Hz/(W/cm^2) to determine the dynamic perpendicular and parallel radial electronic polarizabilities, $\alpha_\perp$ and $\alpha_\parallel$. The polarizability difference $\Delta\alpha_{\text{ele}} = \alpha_\parallel - \alpha_\perp$ is obtained by fitting the experimental results of Fig. 5.6 (B) to $\Delta\alpha(\phi) = 2/15 \times (1 - 3\cos^2\phi)(\alpha_\parallel - \alpha_\perp)$. The fitted values are $\alpha_\perp = h \times 12$ Hz/(W/cm^2) and $\alpha_\parallel = h \times 34$ Hz/(W/cm^2).

Although the lines in panel (A) appear to be linear, they are in fact parabolic at a closer look, see panel (C). This is the hyperpolarizability described by β in Eq. 5.3. To determine β, we use a similar π-pulse spectroscopy, but with a higher frequency resolution. We work at the magic angle, $\phi = 54^\circ$, and again record transition spectra, this time for various electric fields. We extract β (blue circles) by fitting Eq. (5.3). As expected, it decreases with increasing electric field as the spin-decoupling improves.

If $d_0 E \ll B_{\text{rot}}$ and $d_0^2 E^2 / B_{\text{rot}}$ is much larger than $\Delta\alpha_{\text{ele}} I$ or the Zeeman splitting at $E = 0$, and away from any spectral crossings, β can be derived from the second order perturbation of the energy as

$$\beta(E,\phi) = \frac{4}{15}\sin^2(2\phi)\frac{\Delta\alpha_{\text{ele}}^2 B_{\text{rot}}}{d_0^2 E^2}, \tag{5.7}$$

The red line in Fig. 5.6 B shows the result of Eq. (5.7) for our parameters. Although experiment and theory qualitatively agree, the measured values are slightly smaller

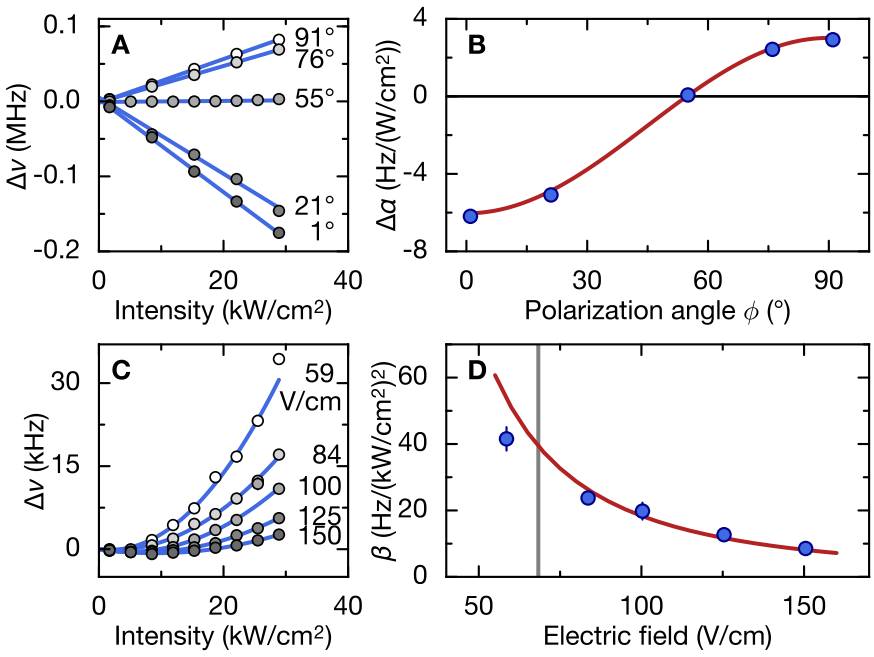

Figure 5.6: *Characterizing the spin-decoupled magic trap. Circles are measurements, red lines theory results and blue lines correspond to fits of the data to Eq. 5.3. All error bars were calculated from the covariance matrix of the respective fits and are partially smaller than the marker size. (**A**) AC Stark data at $E = 144.3$ V/cm to extract the differential polarizability, $\Delta\alpha$. (**B**) Differential polarizability $\Delta\alpha$ for various lattice polarization angles. At approximately 54° a magic trapping condition is fulfilled and the differential polarizability vanishes. (**C**) AC Stark data to extract the hyperpolarizability β for five electric field values in units of V/cm. (**D**) Hyperpolarizability β at the magic angle for various DC electric fields. The larger the electric field, the smaller the hyperpolarizability. For the measurements discussed in Chap. 6, we use the field strength indicated by the vertical black line.*

than the theoretical ones, especially for smaller values of E. This discrepancy might be due to the AC Stark shift from the MW itself or higher order light shifts that are not included in the simplified theoretical model.

Chapter 6

Interacting molecules

Exploring and employing the anisotropic dipole-dipole interactions between polar molecules is the ultimate reason why experimental setups such as the one discussed in Chapter 3 were built. The two methods for inducing dipolar interactions in a molecular gas – strong dc electric fields or rotational superpositions – were already discussed in Section 2.3. In this chapter, we study the coherence of rotational superpositions in the spin-decoupled magic trap that we established in Chapter 5. Methods and results of our Ramsey- and spin-echo spectroscopy are summarized in Section 6.1. We interpret the results in Section 6.2 using e. g. a moving-average cluster expansion (MACE) model. This chapter is based on publication Ref. [36].

6.1 Coherence of a Rotational Superposition

Creating rotational superpositions of molecules is a very appealing way to make a molecular gas interact via the dipole-dipole interaction. One reason is that using large dc electric fields in the kV/cm-range, the other method, is experimentally challenging. The higher the induced dipole moment becomes in the molecular gas, the larger the Stark shifts of the transitions and, consequently, the higher the electric field stability needs to be in order to ensure resonant transitions. Rotational superpositions, on the other hand, are conveniently prepared using microwave pulses. Furthermore, transition dipole moments are huge. In the case of the $|J,m_J\rangle = |0,0\rangle \rightarrow |1,1\rangle$ transition from the rotational ground to the first excited state, it is almost 60% of the permanent electric dipole moment.

However, a rotational superposition is only useful if it has a long enough coherence time. In the following, we will discuss how we measure rotational coherence using Ramsey- and spin-echo spectroscopy in the spin-decoupled magic trap of Chapter 5.

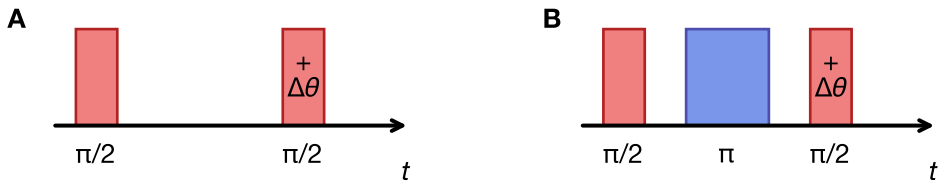

Figure 6.1: *Schematic of the pulse sequences for Ramsey (**A**) and spin-echo microwave spectroscopy (**B**). To obtain Ramsey fringes we scan the phase offset of the second $\pi/2$-pulse by $\Delta\theta$. For spin-echo, a π pulse in the middle of the evolution time t is added. Adapted from [36].*

6.1.1 Setup and Experimental Methods

The experimental setup for studying the rotational coherence is the same as in the previous chapter: We load the atomic mixture to many layers of a 1D lattice and proceed with molecule association there. To realize the spin-decoupled magic trap, we make use of a small dc electric field of $E = 68.3$ V/cm parallel to the lattice planes, which is large enough to decouple the $|\uparrow\rangle$ state and small enough to minimize inhomogeneous broadening or temporal noise of the dc Stark shift. Additionally, we adjust the polarization vector of the $I = 3.4$ kW/cm^2 lattice to the magic angle with respect to the electric field axis. A dipole antenna for the MW radiation is mounted closely to the glass cell. A sketch of this setup can be found in Fig. 5.3.

To study the rotational coherence in the spin-decoupled magic trap, we use Ramsey and spin-echo pulse sequences [106], see Fig. 6.1. We set the MW frequency ν to resonance and scan the relative phase $\Delta\theta$ between the first and second $\pi/2$ pulse at a fixed evolution time t to obtain Ramsey interference fringes. For spin-echo, we add a π-pulse in the middle of the evolution time. Each fringe can be described by

$$N_{|\downarrow\rangle}(\Delta\theta, t) = \frac{N(t)}{2}[1 - c(t)\cos(\Delta\theta + \theta_0)], \tag{6.1}$$

where $c(t)$ is the measured contrast, $N = N_{|\downarrow\rangle} + N_{|\uparrow\rangle}$ is the total molecule number and θ_0 is a phase offset due to small detunings of the MW, e. g. due to electric field changes.

To generate different molecular densities for the Ramsey- and spin-echo experiments, we vary the hold time between Feshbach molecule production and further experiments, which leads to loss due to inelastic collisions. This allows us to change the molecule number while keeping the cloud radius almost constant.

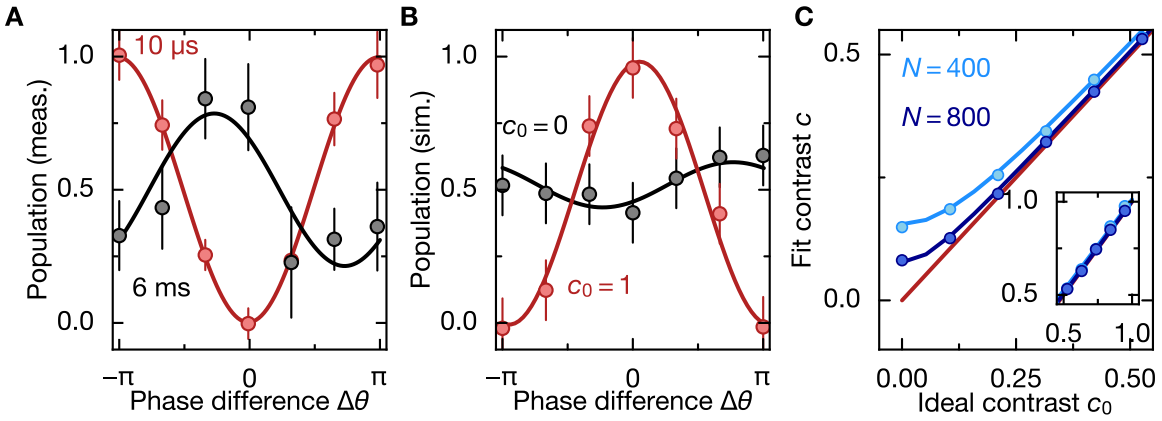

Figure 6.2: *Ramsey fringes and fitting bias considerations. (**A**) Two measured Ramsey fringes for different evolution times (circles), together with their fits (solid lines). Error bars denote the standard error of the mean over several experimental runs. (**B**). Simulated fringes for $N = 400$ molecules in presence of molecule number fluctuations. Circles denote the simulated population as a function of $\Delta\theta$, solid lines correspond to the respective fits. Error bars denote the standard error of the mean over several simulations. (**C**) Fitted contrast c as function of the actual contrast c_0 when N =400 (light blue) or 800 (dark blue). Solid lines in the same color are the corresponding contrasts given by Eq.* (6.3)*. The red line shows the measured contrast without noise. In all simulations we used $\Delta N = 98$, and $M_s = 35$, similar to what we observe in experiments. Above $c_0 = 0.5$, all three lines essentially agree (inset). Adapted from [36].*

6.1.2 Ramsey- and Spin-Echo Spectroscopy

To extract the coherence time, we measure the fringe contrast $c(t)$ for various evolution times t. Figure 6.2 (A) shows to Ramsey fringes recorded for $t = 10$ µs and $t = 6$ ms (circles). The initial phase of the Ramsey fringe is unknown and can drift slowly. Therefore, we let c be strictly positive in the fringe fitting with Eq. 6.1 to avoid phase ambiguities for small contrasts (lines). This, however, biases the coherence time when the fringe amplitude becomes comparable to the molecule number fluctuations [107].

To quantitatively understand this, we simulate Ramsey interference fringes in presence of molecule number fluctuations, see Fig. 6.2 (B). We add Gaussian noise with a standard deviation ΔN to the molecule number of an ideal sinusoidal fringe with contrast c_0 and use Eq. 6.1 to extract the resulting contrast. We repeat this simulation 300 times and obtain an average measured contrast c. We find that the contrast

bias Δc adds quadratically to the ideal contrast, see Fig. 6.2 (C) as

$$c = \sqrt{c_0^2 + \Delta c^2}, \tag{6.2}$$

where

$$\Delta c = \sqrt{\frac{a}{M_s}} \frac{2\Delta N}{N_{\text{tot}}}. \tag{6.3}$$

Here, M_s is the sampling size and $a = 3.5$ is an empirical parameter obtained from the simulations. In our experiments, $\Delta c \approx 10\%$, depending on the molecule number. Using Eq. 6.3, we estimate the bias Δc for each data point individually and exclude data taken after the smallest evolution time where $c < 1.5\Delta c$. The remaining contrast values are then fit with a Gaussian function of the form

$$c(t) = c_i \exp\left(-\left(\frac{t}{\tau}\right)^2\right), \tag{6.4}$$

where c_i is the initial contrast at the shortest evolution time and τ denotes the coherence time.

Another approach would be to subtract the contrast bias using Eq. (6.2) before the fitting. We found that in this case the coherence time is overestimated by less than 10%, even when the low contrast data is included. This is because the the small-contrast tails contribute less to the fitting of the Gaussian of Eq. (6.4) than the high contrast data. The detection offset of the molecule number is less than 20 molecules and thus negligible.

Figure 6.3 summarizes our Ramsey (A) and spin-echo (B) measurements for various molecule numbers (indicated in the upper right corners) and densities. The bias of each data point according to Eq. 6.3 is indicated by the dark grey shaded area, the light grey area denotes the bias cutoff. Red (blue) lines show the Gaussian fits of Eq. 6.4, that we use to extract the coherence times τ. Data points that are excluded from this fit are indicated by empty circles. The Ramsey coherence time, here defined as the $1/e$ time of the fit, amounts to 8.7(6) ms for a low molecule number $N_{\text{tot}} = 740(70)$, which is six times larger than previously achieved coherence times [33, 100]. Residual single particle dephasing could arise due to residual differential light shifts, electric field gradients, and shot-to-shot fluctuations of the electric field.

By adding a π pulse in the middle of the evolution, we obtain a spin-echo sequence [108]. The π-pulse reverses the dephasing accumulated during the first half of the time evolution by inverting the order of the precessing spins on the Bloch sphere, which do so at different speeds due to the dephasing. Thus, during the second half of the evolution time, the slowly varying contributions to the single particle dephasing can be canceled. This allows us to increase the coherence time to $\tau = 13(2)$ ms for low

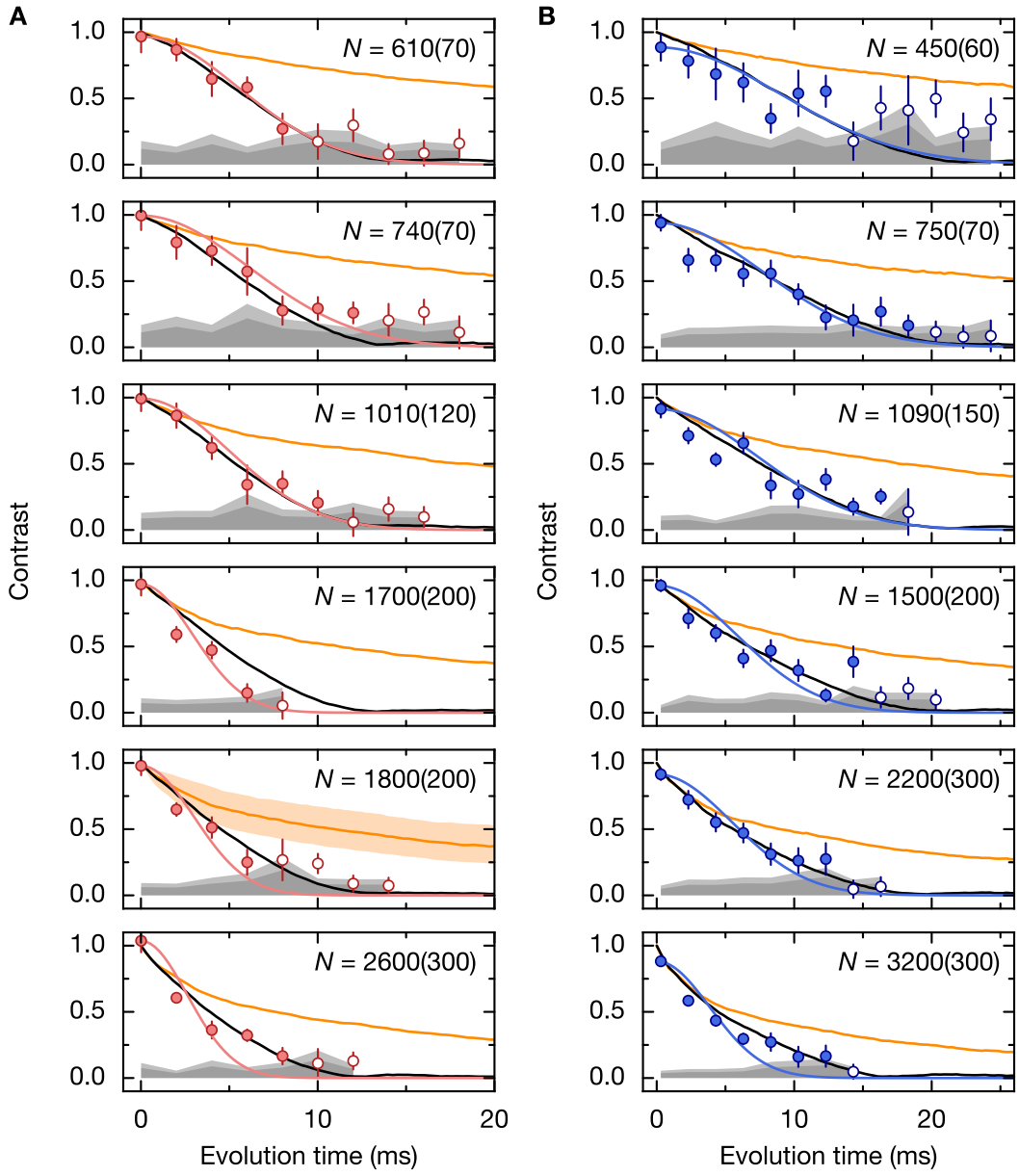

Figure 6.3: *Measuring and simulating rotational coherence. (**A**) Comparison of measurement (circles) and simulation (orange and black lines) of the Ramsey experiments. Numbers in the right corner denote the initial molecule number N (number error ΔN). Light red solid lines are Gaussian fits to extract the coherence time, black (orange) solid lines correspond to MACE simulations with (without) external field gradient $h \times 1.3(1)$ Hz/µm. The orange shaded region demonstrates the effect of a factor of two change in density in either direction on the simulation. Dark grey shaded regions indicate the bias of the data, the light grey regions the cutoff for the data (empty circles) that we chose to avoid fitting bias. (**B**) As in (A) but for the spin-echo experiments (blue). The external field gradient for the MACE simulation is $h \times 0.8(1)$ Hz/µm. Adapted from [36].*

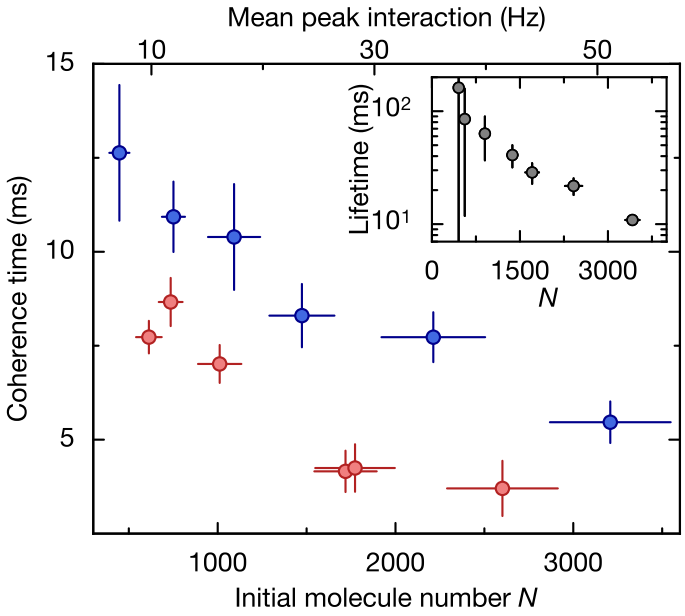

Figure 6.4: *Ramsey (red) and spin-echo (blue) coherence times for various molecular densities. A mean dipolar interaction strength at the center of the cloud is indicated on the secondary x axis. The coherence time is not limited by the $1/e$ lifetime of the rotational superposition, as shown in the inset. All error bars are calculated from the covariance matrix of the fits and denote one standard deviation. Adapted from [36].*

initial molecule numbers. Note that the molecules in this work are moving with the trapping period of $T_{\text{trap}} = 16$ ms in the horizontal planes, which are weakly confined by the 1D lattice. Spin echo fails to suppress or even enhances the single particle dephasing when the evolution time is close to the trapping period [109]. This explains why the maximum coherence time observed in our experiment remains below T_{trap}.

Furthermore, we find that the coherence time depends on the initial molecule number and thus on density, see Fig. 6.4. There could be several reasons for this. One explanation would be a loss of molecules. However, because these collisions are suppressed by the p-wave barrier, we measure an intrastate inelastic collision rate of below 3 Hz. Thus, interstate inelastic collisions dominate. But since these lead to equal loss of $|\downarrow\rangle$ and $|\uparrow\rangle$ molecules, they do not reduce the fringe contrast. Furthermore, this two-body loss occurs on much longer time scales than the decoherence, see inset of Fig. 6.4. Therefore, we assume that another reason is responsible for the density dependent decoherence in the system, namely the strong dipolar interaction present in the system.

6.2 Interpreting the Results

To test our hypothesis that the density dependent decoherence is due to the density-dependent dipole-dipole interaction, we set up a simple theoretical model based on the moving-average cluster expansion (MACE) method. Further, we estimate dephasing rates due to experimental imperfections.

6.2.1 Dipolar Interactions and MACE Model

We employ the moving-average cluster expansion (MACE) method [110] to qualitatively understand the decoherence of the molecular rotation. With the MACE, we can simulate the spin dynamics of randomly distributed molecules in bulk during the Ramsey or spin-echo interferometry. If we neglect loss and molecular motion, the system can be described by the following Hamiltonian

$$H = \sum_{i>j} \frac{U_{ij}}{2} (\hat{S}_i^+ \hat{S}_j^- + \text{h.c.}) + \sum_i \Delta(\boldsymbol{r}_i) \hat{S}_i^z, \tag{6.5}$$

where the first term describes the dipolar spin-exchange interaction and the second term the coupling to external fields. $\hat{S}_i^{\pm}$ and $\hat{S}_i^z$ are the spin-1/2 angular momentum operators of molecule i in position $\boldsymbol{r}_i$ and U_{ij} is the dipole-dipole interaction strength between molecules i and j, which is given as

$$U_{ij} = \frac{2d_{\uparrow\downarrow}^2}{(4\pi\varepsilon_0)} \frac{1 - 3\cos^2\Theta_{ij}}{(|\boldsymbol{r}_i - \boldsymbol{r}_j|^3)}, \tag{6.6}$$

where $d_{\uparrow\downarrow} = \sqrt{1/3} d_0$ is the transition dipole moment between $|\downarrow\rangle$ and $|\uparrow\rangle$ [72, 73], ε_0 is the vacuum permittivity, and Θ_{ij} is the angle between the vector connecting molecules i and j and the quantization axis, which we assume to be along the electric field direction. Finally, $\Delta(\boldsymbol{r}_i)$ describes a spatially dependent detuning of the microwave transition.

The mean value of the angular-independent part of U_{ij} of Eq. 6.6 sets an energy scale for the dipolar interaction, which can be calculated as

$$\langle U_d \rangle \approx \frac{2|d_{\uparrow\downarrow}^2|}{4\pi\varepsilon_0 l^3}, \tag{6.7}$$

where $l = n_0^{-1/3}$ is the average distance between molecules and n_0 is the peak molecular density. Note, that the lattice spacing 0.775 µm is much less than the average distance between molecules in our setup. Therefore, the density distribution of the

molecular gas can be approximated by

$$n(x,y,z) = n_0 \exp\left(-\frac{x^2}{\sigma_x^2} - \frac{y^2}{\sigma_y^2} - \frac{z^2}{\sigma_z^2}\right), \tag{6.8}$$

where the peak molecular density is

$$n_0 = \frac{N}{\pi^{3/2}\sigma_x\sigma_y\sigma_z}. \tag{6.9}$$

The $1/e$ radii $\sigma_x = \sigma_y = 27(4)$ µm and $\sigma_z = 11.5(6)$ µm of the molecular cloud are determined by *in situ* imaging. The peak density for the highest molecule number 3200(300) is $7(3) \times 10^{10}$ /cm^3 and the corresponding average distance is $2.4(3)$ µm. This results in a peak dipolar interaction of $\langle U_d \rangle = h \times 50(20)$ Hz, similar to the decoherence rate we observe at the highest molecule number. This dipolar energy scale is indicated on the secondary axis of Fig. 6.4.

For more thorough insights, we implement the Hamiltonian of Eq. 6.5 using the MACE [110]. We randomly distribute the molecules with a Gaussian probability distribution in tens of layers of the 1D-lattice with a spacing of 0.775 µm and assume, that they are spatially frozen. We use the experimentally determined cloud radii along x, y, and z direction in the simulation. According to the MACE idea, we divide all molecules into clusters, in our case each consists of four molecules, which are closest to each other and thus have the strongest dipolar interactions. Then we exactly solve the time evolution for each of the hundreds of clusters and sum up the expectation values of all spins to obtain the Ramsey signal.

If the external field is homogeneous and the second term of Hamiltonian 6.5 can be neglected, the decoherence is due to the random spread of dipolar interaction among the molecules. We expect the coherence time τ to be inversely proportional to the molecule number N_{mol} because the dipolar interaction is proportional to the molecular density. In this homogeneous MACE simulation the $1/e$ coherence time is about 12 ms with 3000 and 70 ms with 500 molecules, see orange lines in Fig. 6.3. In the Ramsey experiments displayed in (A), however, the coherence time is limited to about 8 ms, even for low molecule numbers of 600, when the dipolar interaction is negligible. Therefore, we attribute this to residual single particle dephasing, which will be discussed in the next section.

In order to qualitatively introduce this dephasing into the model, we implement a simple *effective* external field gradient along x-direction $\Delta = \Delta' x$ in the model. Please note, that this is a fictitious gradient, which, however, leads to simulation results that are comparable with our experimental findings. In the experiment, we make sure that no such gradient is present using the electric field control discussed in Section 3.4. In

the model, we also tried a parabolic external field, which, however, produces similar decoherence behavior in the simulation. For the sake of simplicity we therefore use the simple field gradient for now. To determine which magnitude to use in the simulation, we fit the MACE model to the experimental data with the lowest molecule number. We obtain $\Delta' = h \times 1.3(1)$ Hz/µm, which corresponds to a dephasing rate of $h \times 35(2)$ Hz. Using this exact effective dephasing, we can reproduce the Ramsey experiments with various molecule numbers in the simulation (black lines in Fig. 6.3 (A)). For the spin-echo experiments, see Fig. 6.3 (B), we again determine the effective external field gradient by fitting to a low molecule number data set. We obtain $\Delta' = h \times 0.8(1)$ Hz/µm, which corresponds to a dephasing rate of $h \times 21(2)$ Hz.

The excellent agreement of experiment and simulation indicates that dipolar interactions are the dominant source of the density-dependent decoherence. However, in the future a theoretical model tailored to the trap geometry discussed in this work could deepen the understanding of the system. It could shed light on how molecular loss, motion and contact interaction modify the spin dynamics in a bulk gas of polar molecules.

6.2.2 Causes of Single-Particle Dephasing

In addition to the density-dependent decoherence, also single-particle dephasing is important in the MACE model. This dephasing is due to transition frequency changes between $|\downarrow\rangle$ and $|\uparrow\rangle$. These consist of temporal fluctuations and spatial variations in the external potential across the molecular cloud and can be described by the MW detuning term $\Delta(\mathbf{r},t)$ of Eq. 6.5. We can expand it as

$$\Delta(\boldsymbol{r},t) = \Delta\alpha I(\boldsymbol{r}) + \beta I^2(\boldsymbol{r}) + \xi E(\boldsymbol{r},t)^2. \tag{6.10}$$

The first two terms are residual first-order and second-order differential light shifts from Eq. 5.7, that remain even in the magic trap configuration. We assume that the lattice beam has a Gaussian intensity profile and ignore the intensity variation along z-direction

$$I(\boldsymbol{r}) = I_{\text{peak}} \exp\left(-2\frac{x^2+y^2}{\omega_0^2}\right) \tag{6.11}$$

with beam waist $\omega_0 = 100\,\mu\text{m}$. The third term of Eq. 6.10 is the differential dc Stark shift, where according to [73]

$$\xi = \frac{4}{15}\frac{d_0^2}{B_{\text{rot}}} = h \times 177\,\frac{\text{Hz}}{(\text{V/cm})^2}. \tag{6.12}$$

The electric field E can be written as

$$E(\boldsymbol{r},t) \approx E_0(t) + \nabla E \cdot \boldsymbol{r} + \mathcal{O}(r^2), \tag{6.13}$$

source	value	dephasing rate
$\delta\alpha$	$h \times 0.05$ Hz/(W/cm^2)	$\gamma_{\mathrm{L}} = h\times 32$ Hz
β	$h \times 30$ Hz/(kW/cm^2)^2	
δE	0.5 mV/cm	$\gamma_{\mathrm{EN}} = h\times 12$ Hz
∇E	0.5 V/cm^2	$\gamma_{\mathrm{EG}} = h\times 38$ Hz

Table 6.1: *Maximal dephasing rates at 68.3 V/cm due to imperfect cancellation of local differential polarizability $\delta\alpha$ and residual hyperpolarizability β, and due to electric field noise and gradients, δE and ∇E.*

where $E_0(t)$ describes the temporal fluctuations and the second term captures the first-order inhomogeneity of E.

The inhomogeneity of $\Delta(\mathbf{r})$ leads to dephasing of rotational excitations and can be calculated from Eq. 6.10 by numerical integration. The experimentally observed dephasing γ thus can be divided into local and temporal contributions: γ_{L} due to residual differential light shifts, γ_{EG}, due to gradient electric fields, and γ_{EN} due to temporal fluctuations of E. The dephasing due to residual differential light shifts can be written as

$$\gamma_{\mathrm{L}} = \frac{\int n(\boldsymbol{r}) \left|\delta\alpha\Delta I(\boldsymbol{r}) + \beta\Delta I^2(\boldsymbol{r})\right| \boldsymbol{dr}}{\int n(\boldsymbol{r}) \boldsymbol{dr}}, \tag{6.14}$$

where the local differential polarizability is given as

$$\delta\alpha = h(\partial\nu/\partial I)|_{I=I_{\mathrm{peak}}} = \Delta\alpha + 2\beta I_{\mathrm{peak}}. \tag{6.15}$$

Here, $\Delta I(\boldsymbol{r}) = I(\boldsymbol{r}) - I_{\mathrm{peak}}$, and $n(\mathbf{r})$ is the molecular density described in Eq. 6.8. The dephasing rate due to gradient electric fields $|\nabla E|$, which we assume to be along x-direction for simplicity, is given as

$$\gamma_{\mathrm{EG}} = 2\xi\overline{E_0}|\nabla E|\sigma_x, \tag{6.16}$$

where $\overline{E_0}$ is the time averaged electric field in the center of the molecular cloud. The dephasing due to temporal electric field noise δE_0 is, finally,

$$\gamma_{\mathrm{EN}} = 2\xi\overline{E_0}\delta E_0. \tag{6.17}$$

The estimated maximal dephasing rates for these contributions are summarized in Tab. 6.1 together with their experimental origin.

The total effective dephasing rate can then be calculated as

$$\gamma = \sqrt{\gamma_{\mathrm{L}}^2 + \gamma_{\mathrm{EG}}^2 + 2\gamma_{\mathrm{EN}}^2} \tag{6.18}$$

and is related to the coherence time by $\tau \approx 2\hbar/\gamma$ which we verified by numerical simulation.

In the current setup, the dephasing rate γ is on the order of a few ten Hz. In the future, we hope to reduce the dephasing rate to a few Hz by implementing less noisy, more homogeneous dc electric fields as well as more precise laser polarization control.

Chapter 7

Summary and Outlook

During the work on this PhD, we developed a thorough understanding of the molecule production process using STIRAP. We learned, that a large one-photon detuning is advantageous for molecule production when dealing with unresolved hyperfine structure in the intermediate state. Other molecule experiments had so far not encountered this to such a degree. Secondly, also a precise knowledge of the initial Feshbach state is extremely helpful as it determines which hyperfine states can be populated at all and with which amplitudes. We found very good agreement with the coupled channels calculation of the Feshbach wavefunction, while the asymptotic bound state model we had used before had made completely different predictions. This allowed us to pick a suitable polarization scheme for the STIRAP as to reduce the amount of coupled levels. Only with this knowledge it became possible to routinely produce several thousands of ground state molecules with a STIRAP efficiency of about 50% on a shot-to-shot basis in the experimental setup.

Once the ground state molecule production was secured, we started to explore how to best polarize them. We induced dipole moments of 0.5 D using static electric fields, and even larger transition dipole moments using superpositions of the rotational ground and first excited states, that can be excited using microwaves. With spin-decoupled magic trapping we improved on the magic polarization angle trapping technique that had already been demonstrated in ^{40}K^{87}Rb [100] by adding a small dc electric field. This allowed us to bring down hyperpolarizability, the dependence of polarizability on intensity, which had been limiting the rotational coherence time in the previous experiment. The about one order of magnitude improved rotational coherence time in Ramsey- or spin-echo experiments allowed us to observe that it also depends on density. A moving-average cluster expansion model allowed us to verify that this is due to the strong dipolar interactions in the system.

With these two milestones reached, the experiment is in an excellent position for future experiments.

7.1 Technical Upgrades

Although we routinely create several 1000 ground state molecules with the current setup, there is room for improvement. First of all, the STIRAP efficiency could be increased. With the current scheme, it is 50%, slightly worse than the 75% reported by the $^{23}Na^{40}K$ experiment at Massachusetts Insitute of Technology (MIT) [24]. There are essentially two options: The first is to switch to the alternative route to the ground state demonstrated by the MIT group via a lower energy intermediate state with partially resolved hyperfine structure. However, this would require an entire new STIRAP laser system. I would therefore recommend to first try a different polarization scheme within our current route to the ground state. As we saw in the multilevel STIRAP-simulation in Chapter 4, using σ^+-polarization on both STIRAP beams would be very advantageous. Therefore, it would certainly pay off to find a way to realize this polarization scheme in future setup changes.

The STIRAP efficiency is only one bottle neck in producing a high phase-space density quantum gas. However, most phase-space density is already lost before the STIRAP sequence starts, because the efficiency for Feshbach molecule production is only 10%. The most promising way to change that is Feshbach association in a 3D optical lattice [40, 111]. Ideally, one would prepare lattice sites with exactly one atom of each species, so that the subsequent Feshbach association would be very efficient. Therefore, we have prepared a 3D optical lattice setup for our lab [112], which is currently being tested.

Further, we also already work on an improved high-voltage setup for dc polarizing the molecules and improving the spin-decoupling for rotational states in the magic trap. We will also have the possibility to apply the spin-decoupled magic trapping technique to the 3D lattice.

7.2 Future Experiments

With these new tools in place, several experiments can be performed. First, the molecule production can be improved in the lattice. The maximal molecule number that could be reached in the seminal experiments on $^{40}K^{87}Rb$ molecules in an optical lattice [113] was limited by to the small size of the unity-filling Mott insulator. Since the bosonic sodium in $^{23}Na^{40}K$ is significantly lighter than Rubidium, we expect this to be a less severe limitation in our system. Numerical calculations show, that a molecular filling factor of 0.4 should be feasible in our 3D optical lattice. In addition to providing ideal starting conditions for Feshbach association, a deep lattice is also helpful to increase the coupling strength on the pump transition. Since inelastic collisions be-

tween Feshbach molecules are prevented, it should become possible to go to deeper bound Feshbach states, which have higher Franck-Condon factors to the intermediate state.

Once higher molecule numbers can be reached, it also becomes feasible to think about evaporative cooling to further increase the phase-space density of the molecular gas. This, however, requires elastic collisions between molecules for thermalization. Therefore, the collisional two-body loss discussed in Section 4.3, that even non-reactive molecules suffer from, should be investigated further. It has been suggested to reduce the trap dimensionality and to use a static polarizing field perpendicular to the trap, so that the strong repulsion between molecules prevents collisions [75, 92, 114, 115]. Alternatively, dressing of the molecular rotation with blue detuned microwaves might also lead to a shielding effect [116].

But even in a deep lattice, in which tunnelling of the molecules in not possible, spin-models with long-range interactions can be studied [28] due to the dipolar spin-exchange interaction. One very exciting proposal is about a condensate of the rotational excitation [117, 118] in a 2D system. The coherence of a rotational excitation in this system, as measured e.g. by Ramsey spectroscopy, will depend on the filling. Below a critical filling of 0.15, the coherence is expected to reduce with the filling, while it will diverge at larger fillings. This is due to a conservation of energy and due to the relativistic dispersion of the spin-wave due to the long-range dipole-dipole interaction.

Bibliography

[1] M. H. Anderson, J. R. Ensher, M. R. Matthews, C. E. Wieman, and E. A. Cornell. *Observation of Bose-Einstein condensation in a dilute atomic vapor.* Science **269**, 198–201 (1995). (Cited on page **1**)

[2] C. C. Bradley, C. A. Sackett, J. J. Tollett, and R. G. Hulet. *Evidence of Bose-Einstein Condensation in an Atomic Gas with Attractive Interactions*. Phys. Rev. Lett. **75**, 1687–1690 (1995). (Cited on page **1**)

[3] K. B. Davis, M. O. Mewes, M. R. Andrews, N. J. van Druten, D. S. Durfee, D. M. Kurn, and W. Ketterle. *Bose-Einstein Condensation in a Gas of Sodium Atoms*. Phys. Rev. Lett. **75**, 3969–3973 (1995). (Cited on page **1**)

[4] B. DeMarco. *Onset of Fermi Degeneracy in a Trapped Atomic Gas*. Science **285**, 1703–1706 (1999). (Cited on page **1**)

[5] I. Bloch, J. Dalibard, and W. Zwerger. *Many-body physics with ultracold gases*. Rev. Mod. Phys. **80**, 885–964 (2008). (Cited on pages **1** and **62**)

[6] K. Viebahn, M. Sbroscia, E. Carter, J.-c. Yu, and U. Schneider. *Matter-Wave Diffraction from a Quasicrystalline Optical Lattice*. Phys. Rev. Lett. **122**, 110404 (2019). (Cited on page **1**)

[7] H. Ott. *Single atom detection in ultracold quantum gases: A review of current progress*. Reports Prog. Phys. **79** (2016). (Cited on page **1**)

[8] M. Boll, T. A. Hilker, G. Salomon, A. Omran, J. Nespolo, L. Pollet, I. Bloch, and C. Gross. *Spin- and density-resolved microscopy of antiferromagnetic correlations in Fermi-Hubbard chains*. Science **353**, 1257–1260 (2016). (Cited on page **1**)

[9] L. Santos, G. V. Shlyapnikov, and M. Lewenstein. *Roton-Maxon Spectrum and Stability of Trapped Dipolar Bose-Einstein Condensates*. Phys. Rev. Lett. **90**, 250403 (2003). (Cited on page **1**)

[10] L. Chomaz, R. M. W. van Bijnen, D. Petter, G. Faraoni, S. Baier, J. H. Becher, M. J. Mark, F. Wächtler, L. Santos, and F. Ferlaino. *Observation of roton mode population in a dipolar quantum gas*. Nat. Phys. **14**, 442–446 (2018). (Cited on page **1**)

[11] H. Kadau, M. Schmitt, M. Wenzel, C. Wink, T. Maier, I. Ferrier-Barbut, and T. Pfau. *Observing the Rosensweig instability of a quantum ferrofluid*. Nature **530**, 194–197 (2016). (Cited on page **1**)

[12] I. Ferrier-Barbut, H. Kadau, M. Schmitt, M. Wenzel, and T. Pfau. *Observation of Quantum Droplets in a Strongly Dipolar Bose Gas*. Phys. Rev. Lett. **116**, 215301 (2016). (Cited on page **1**)

[13] B. Capogrosso-Sansone, C. Trefzger, M. Lewenstein, P. Zoller, and G. Pupillo. *Quantum Phases of Cold Polar Molecules in 2D Optical Lattices*. Phys. Rev. Lett. **104**, 125301 (2010). (Cited on page **1**)

[14] D. Peter, S. Müller, S. Wessel, and H. P. Büchler. *Anomalous behavior of spin systems with dipolar interactions*. Phys. Rev. Lett. **109**, 025303 (2012). (Cited on page **1**)

[15] A. Griesmaier, J. Werner, S. Hensler, J. Stuhler, and T. Pfau. *Bose-Einstein Condensation of Chromium*. Phys. Rev. Lett. **94**, 160401 (2005). (Cited on page **1**)

[16] M. Lu, N. Q. Burdick, S. H. Youn, and B. L. Lev. *Strongly Dipolar Bose-Einstein Condensate of Dysprosium*. Phys. Rev. Lett. **107**, 190401 (2011). (Cited on page **1**)

[17] K. Aikawa, A. Frisch, M. Mark, S. Baier, A. Rietzler, R. Grimm, and F. Ferlaino. *Bose-Einstein Condensation of Erbium*. Phys. Rev. Lett. **108**, 210401 (2012). (Cited on page **1**)

[18] R. Löw, H. Weimer, J. Nipper, J. B. Balewski, B. Butscher, H. P. Büchler, and T. Pfau. *An experimental and theoretical guide to strongly interacting Rydberg gases*. J. Phys. B **45**, 113001 (2012). (Cited on page **1**)

[19] P. Schauß, M. Cheneau, M. Endres, T. Fukuhara, S. Hild, A. Omran, T. Pohl, C. Gross, S. Kuhr, and I. Bloch. *Observation of spatially ordered structures in a two-dimensional Rydberg gas*. Nature **491**, 87 (2012). (Cited on page **1**)

[20] H. Ritsch, P. Domokos, F. Brennecke, and T. Esslinger. *Cold atoms in cavity-generated dynamical optical potentials*. Rev. Mod. Phys. **85**, 553–601 (2013). (Cited on page **1**)

[21] K.-K. Ni, S. Ospelkaus, M. H. G. de Miranda, A. Pe'er, B. Neyenhuis, J. J. Zirbel, S. Kotochigova, P. S. Julienne, D. S. Jin, and J. Ye. *A High Phase-Space-Density Gas of Polar Molecules*. Science **322**, 231–235 (2008). (Cited on pages **1**, **2**, **38**, and **45**)

[22] T. Takekoshi, L. Reichsöllner, A. Schindewolf, J. M. Hutson, C. R. Le Sueur, O. Dulieu, F. Ferlaino, R. Grimm, and H.-C. Nägerl. *Ultracold Dense Samples of*

Dipolar RbCs Molecules in the Rovibrational and Hyperfine Ground State. Phys. Rev. Lett. **113**, 205301 (2014). (Cited on pages **1**, **2**, **21**, **38**, and **45**)

[23] P. K. Molony, P. D. Gregory, Z. Ji, B. Lu, M. P. Köppinger, C. R. Le Sueur, C. L. Blackley, J. M. Hutson, and S. L. Cornish. *Creation of Ultracold $^{87}Rb^{133}Cs$ Molecules in the Rovibrational Ground State*. Phys. Rev. Lett. **113**, 255301 (2014). (Cited on pages **1**, **2**, **21**, **38**, and **45**)

[24] J. W. Park, S. A. Will, and M. W. Zwierlein. *Ultracold Dipolar Gas of Fermionic $^{23}Na^{40}K$ Molecules in Their Absolute Ground State*. Phys. Rev. Lett. **114**, 205302 (2015). (Cited on pages **1**, **2**, **10**, **19**, **21**, **38**, **45**, **46**, **58**, and **86**)

[25] M. Guo, B. Zhu, B. Lu, X. Ye, F. Wang, R. Vexiau, N. Bouloufa-Maafa, G. Quéméner, O. Dulieu, and D. Wang. *Creation of an Ultracold Gas of Ground-State Dipolar $^{23}Na^{87}Rb$ Molecules*. Phys. Rev. Lett. **116**, 205303 (2016). (Cited on pages **1**, **2**, **21**, **38**, and **45**)

[26] F. Seeßelberg, N. Buchheim, Z.-K. Lu, T. Schneider, X.-Y. Luo, E. Tiemann, I. Bloch, and C. Gohle. *Modeling the adiabatic creation of ultracold polar $^{23}Na^{40}K$ molecules*. Phys. Rev. A **97**, 013405 (2018). (Cited on pages **1**, **2**, **8**, **10**, **17**, **21**, **38**, **43**, **45**, **46**, **47**, and **52**)

[27] A. Chotia, B. Neyenhuis, S. A. Moses, B. Yan, J. P. Covey, M. Foss-Feig, A. M. Rey, D. S. Jin, and J. Ye. *Long-lived dipolar molecules and Feshbach molecules in a 3D optical lattice*. Phys. Rev. Lett. **108**, 080405 (2012). (Cited on page **1**)

[28] B. Yan, S. A. Moses, B. Gadway, J. P. Covey, K. R. A. Hazzard, A. M. Rey, D. S. Jin, and J. Ye. *Observation of dipolar spin-exchange interactions with lattice-confined polar molecules*. Nature **501**, 521–525 (2013). (Cited on pages **1** and **87**)

[29] S. Ospelkaus, K.-K. Ni, G. Quéméner, B. Neyenhuis, D. Wang, M. H. G. de Miranda, J. L. Bohn, J. Ye, and D. S. Jin. *Controlling the Hyperfine State of Rovibronic Ground-State Polar Molecules*. Phys. Rev. Lett. **104**, 030402 (2010). (Cited on pages **1**, **22**, and **57**)

[30] P. D. Gregory, J. Aldegunde, J. M. Hutson, and S. L. Cornish. *Controlling the rotational and hyperfine state of ultracold $^{87}Rb^{133}Cs$ molecules*. Phys. Rev. A **94**, 041403 (2016). (Cited on page **1**)

[31] S. A. Will, J. W. Park, Z. Z. Yan, H. Loh, and M. W. Zwierlein. *Coherent Microwave Control of Ultracold $^{23}Na^{40}K$ Molecules*. Phys. Rev. Lett. **116**, 225306 (2016). (Cited on pages **1**, **20**, **21**, **22**, **41**, and **63**)

[32] M. Guo, X. Ye, J. He, G. Quéméner, and D. Wang. *High-resolution internal state control of ultracold $^{23}Na^{87}Rb$ molecules*. Phys. Rev. A **97**, 020501 (2018). (Cited on page **1**)

[33] J. A. Blackmore, L. Caldwell, P. D. Gregory, E. M. Bridge, R. Sawant, J. Aldegunde, J. Mur-Petit, D. Jaksch, J. M. Hutson, B. E. Sauer, M. R. Tarbutt, and S. L. Cornish. *Ultracold molecules for quantum simulation: rotational coherences in CaF and RbCs*. Quantum Sci. Technol. **4**, 014010 (2018). (Cited on pages **1**, **22**, **38**, **63**, **64**, **65**, and **76**)

[34] D. DeMille. *Quantum Computation with Trapped Polar Molecules*. Phys. Rev. Lett. **88**, 067901 (2002). (Cited on page **2**)

[35] J. W. Park, Z. Z. Yan, H. Loh, S. A. Will, and M. W. Zwierlein. *Second-scale nuclear spin coherence time of ultracold $^{23}Na^{40}K$ molecules*. Science **357**, 372–375 (2017). (Cited on page **2**)

[36] F. Seeßelberg, X.-Y. Luo, M. Li, R. Bause, S. Kotochigova, I. Bloch, and C. Gohle. *Extending Rotational Coherence of Interacting Polar Molecules in a Spin-Decoupled Magic Trap*. Phys. Rev. Lett. **121**, 253401 (2018). (Cited on pages **2**, **22**, **30**, **61**, **62**, **66**, **68**, **73**, **74**, **75**, **77**, and **78**)

[37] K.-K. Ni, S. Ospelkaus, D. Wang, G. Quéméner, B. Neyenhuis, M. H. G. de Miranda, J. L. Bohn, J. Ye, and D. S. Jin. *Dipolar collisions of polar molecules in the quantum regime.* Nature **464**, 1324–8 (2010). (Cited on page **2**)

[38] X. Ye, M. Guo, M. L. González-Martínez, G. Quéméner, and D. Wang. *Collisions of ultracold $^{23}Na^{87}Rb$ molecules with controlled chemical reactivities*. Sci. Adv. **4**, eaaq0083 (2018). (Cited on pages **2** and **58**)

[39] S. A. Moses, J. P. Covey, M. T. Miecnikowski, D. S. Jin, and J. Ye. *New frontiers for quantum gases of polar molecules*. Nat. Phys. **13**, 13–20 (2016). (Cited on page **2**)

[40] L. Reichsöllner, A. Schindewolf, T. Takekoshi, R. Grimm, and H.-C. Nägerl. *Quantum Engineering of a Low-Entropy Gas of Heteronuclear Bosonic Molecules in an Optical Lattice*. Phys. Rev. Lett. **118**, 073201 (2017). (Cited on pages **2** and **86**)

[41] L. Anderegg, L. W. Cheuk, Y. Bao, S. Burchesky, W. Ketterle, K.-K. Ni, and J. M. Doyle. *An Optical Tweezer Array of Ultracold Molecules*. arXiv. 1902.00497 (2019). (Cited on page **2**)

[42] L. De Marco, G. Valtolina, K. Matsuda, W. G. Tobias, J. P. Covey, and J. Ye. *A degenerate Fermi gas of polar molecules*. Science **363**, eaau7230 (2019). (Cited on page **2**)

[43] E. S. Shuman, J. F. Barry, and D. DeMille. *Laser cooling of a diatomic molecule*. Nature **467**, 820–823 (2010). (Cited on pages **2** and **9**)

[44] A. Prehn, M. Ibrügger, R. Glöckner, G. Rempe, and M. Zeppenfeld. *Optoelectrical Cooling of Polar Molecules to Submillikelvin Temperatures*. Phys. Rev. Lett. **116**, 063005 (2016). (Cited on pages **2** and **9**)

[45] L. Anderegg, B. L. Augenbraun, Y. Bao, S. Burchesky, L. W. Cheuk, W. Ketterle, and J. M. Doyle. *Laser cooling of optically trapped molecules*. Nat. Phys. **14**, 890–893 (2018). (Cited on pages **2** and **9**)

[46] A. L. Collopy, S. Ding, Y. Wu, I. A. Finneran, L. Anderegg, B. L. Augenbraun, J. M. Doyle, and J. Ye. *3D Magneto-Optical Trap of Yttrium Monoxide*. Phys. Rev. Lett. **121**, 213201 (2018). (Cited on pages **2** and **9**)

[47] W. C. Stwalley. *Efficient conversion of ultracold Feshbach-resonance-related polar molecules into ultracold ground state ($X\ ^1\Sigma^+$ $v = 0$, $J = 0$) molecules*. Eur. Phys. J. D **31**, 221–225 (2004). (Cited on pages **2** and **45**)

[48] R. Grimm, F. Ferlaino, and S. Knoop. *Ultracold Feshbach Molecules*. In *Cold Molecules: Theory, Experiment, Applications*, pages 1–30. CRC Press (2009). (Cited on pages **2** and **11**)

[49] K. Bergmann, H. Theuer, and B. W. Shore. *Coherent population transfer among quantum states of atoms and molecules*. Rev. Mod. Phys. **70**, 1003–1025 (1998). (Cited on pages **2**, **32**, **43**, and **45**)

[50] N. V. Vitanov, A. A. Rangelov, B. W. Shore, and K. Bergmann. *Stimulated Raman adiabatic passage in physics, chemistry, and beyond*. Rev. Mod. Phys. **89**, 015006 (2017). (Cited on pages **2** and **43**)

[51] S. Ospelkaus, A. Pe'er, K. K. Ni, J. J. Zirbel, B. Neyenhuis, S. Kotochigova, P. S. Julienne, J. Ye, and D. S. Jin. *Efficient state transfer in an ultracold dense gas of heteronuclear molecules*. Nat. Phys. **4**, 622–626 (2008). (Cited on page **2**)

[52] J. M. Sage, S. Sainis, T. Bergeman, and D. DeMille. *Optical Production of Ultracold Polar Molecules*. Phys. Rev. Lett. **94**, 203001 (2005). (Cited on page **2**)

[53] T. M. Rvachov, H. Son, A. T. Sommer, S. Ebadi, J. J. Park, M. W. Zwierlein, W. Ketterle, and A. O. Jamison. *Long-Lived Ultracold Molecules with Electric and Magnetic Dipole Moments*. Phys. Rev. Lett. **119**, 143001 (2017). (Cited on pages **2** and **68**)

[54] H. Yang, D.-C. Zhang, L. Liu, Y.-X. Liu, J. Nan, B. Zhao, and J.-W. Pan. *Observation of magnetically tunable Feshbach resonances in ultracold $^{23}Na^{40}K + {}^{40}K$ collisions*. Science **363**, 261–264 (2019). (Cited on page **2**)

[55] N. Buchheim. *Dual-species apparatus for creating a dipolar quantum gas of $^{23}Na^{40}K$ molecules*. PhD thesis, Ludwig-Maximilians-Universität (2015). (Cited on pages **2**, **8**, **11**, **12**, **14**, **15**, **17**, **25**, **26**, **27**, **30**, **32**, **34**, and **49**)

[56] Z. Lu. *Towards many body physics with ultracold NaK molecules*. PhD thesis, Ludwig-Maximilians-Universität (2016). (Cited on pages **2**, **11**, **12**, **15**, **17**, and **25**)

[57] F. Seeßelberg. *A Dye Laser System for NaK- Photoassociation Spectroscopy*. Master's thesis, Ludwig-Maximilians-Universität (2014). (Cited on pages **5**, **14**, and **36**)

[58] B. Bransden and C. Joachain. *Physics of Atoms and Molecules*. Prentice Hall (2003). (Cited on pages **5**, **6**, **8**, and **14**)

[59] M. Aymar and O. Dulieu. *Calculations of transition and permanent dipole moments of heteronuclear alkali dimers NaK, NaRb and NaCs*. Mol. Phys. **105**, 1733–1742 (2007). (Cited on pages **10** and **14**)

[60] A. Gerdes, O. Dulieu, H. Knöckel, and E. Tiemann. *Stark effect measurements on the NaK molecule*. Eur. Phys. J. D **65**, 105–111 (2011). (Cited on pages **9**, **21**, and **41**)

[61] J. W. Park, S. A. Will, and M. W. Zwierlein. *Two-photon pathway to ultracold ground state molecules of $^{23}Na^{40}K$*. New J. Phys. **17**, 075016 (2015). (Cited on pages **9**, **14**, **19**, and **46**)

[62] C. Chin, R. Grimm, P. Julienne, and E. Tiesinga. *Feshbach resonances in ultracold gases*. Rev. Mod. Phys. **82**, 1225–1286 (2010). (Cited on page **11**)

[63] C.-H. Wu, J. W. Park, P. Ahmadi, S. Will, and M. W. Zwierlein. *Ultracold Fermionic Feshbach Molecules of $^{23}Na^{40}K$*. Phys. Rev. Lett. **109**, 085301 (2012). (Cited on page **11**)

[64] J. W. Park, C. H. Wu, I. Santiago, T. G. Tiecke, S. Will, P. Ahmadi, and M. W. Zwierlein. *Quantum degenerate Bose-Fermi mixture of chemically different atomic species with widely tunable interactions*. Phys. Rev. A **85**, 051602 (2012). (Cited on pages **11**, **46**, and **49**)

[65] T. A. Schulze, T. Hartmann, K. K. Voges, M. W. Gempel, E. Tiemann, A. Zenesini, and S. Ospelkaus. *Feshbach spectroscopy and dual-species Bose-Einstein*

condensation of ^{23}Na-^{39}K mixtures. Phys. Rev. A **97**, 023623 (2018). (Cited on pages **11** and **25**)

[66] R. Pires, M. Repp, J. Ulmanis, E. D. Kuhnle, M. Weidemüller, T. G. Tiecke, C. H. Greene, B. P. Ruzic, J. L. Bohn, and E. Tiemann. *Analyzing Feshbach resonances: A ^{6}Li-^{133}Cs case study*. Phys. Rev. A **90**, 012710 (2014). (Cited on page **12**)

[67] N. Bouloufa-Maafa, R. Vexiau, and O. Dulieu. private communication. (Cited on page **14**)

[68] C. Townes and A. Schawlow. *Microwave Spectroscopy*. McGraw-Hill (1955). ISBN 048661798X. (Cited on pages **14** and **16**)

[69] L. P. Yatsenko, B. W. Shore, and K. Bergmann. *Detrimental consequences of small rapid laser fluctuations on stimulated Raman adiabatic passage*. Phys. Rev. A **89**, 013831 (2014). (Cited on pages **16** and **48**)

[70] M. Aymar and O. Dulieu. *Calculation of accurate permanent dipole moments of the lowest $^{1,3}\Sigma^{+}$ states of heteronuclear alkali dimers using extended basis sets*. J. Chem. Phys. **122**, 204302 (2005). (Cited on page **19**)

[71] A. V. Gorshkov, S. R. Manmana, G. Chen, J. Ye, E. Demler, M. D. Lukin, and A. M. Rey. *Tunable Superfluidity and Quantum Magnetism with Ultracold Polar Molecules*. Phys. Rev. Lett. **107**, 115301 (2011). (Cited on page **20**)

[72] A. V. Gorshkov, S. R. Manmana, G. Chen, E. Demler, M. D. Lukin, and A. M. Rey. *Quantum magnetism with polar alkali-metal dimers*. Phys. Rev. A **84**, 033619 (2011). (Cited on pages **20**, **22**, and **79**)

[73] A. Micheli, G. Pupillo, H. P. Büchler, and P. Zoller. *Cold polar molecules in two-dimensional traps: Tailoring interactions with external fields for novel quantum phases*. Phys. Rev. A **76**, 043604 (2007). (Cited on pages **20**, **22**, **79**, and **81**)

[74] W. Müller and W. Meyer. *Ground-state properties of alkali dimers and their cations (including the elements Li, Na, and K) from ab initio calculations with effective core polarization potentials*. J. Chem. Phys. **80**, 3311 (1984). (Cited on page **21**)

[75] M. Guo, X. Ye, J. He, M. L. González-Martínez, R. Vexiau, G. Quéméner, and D. Wang. *Dipolar Collisions of Ultracold Ground-State Bosonic Molecules*. Phys. Rev. X **8**, 041044 (2018). (Cited on pages **21** and **87**)

[76] P. D. Gregory, J. A. Blackmore, J. Aldegunde, J. M. Hutson, and S. L. Cornish. *ac Stark effect in ultracold polar $^{87}Rb^{133}Cs$ molecules*. Phys. Rev. A **96**, 021402 (2017). (Cited on pages **22**, **63**, **64**, and **68**)

[77] R. Bause. *A High-Resolution Absorption Imaging Setup for Ultracold Dipolar Molecules*. Master's thesis, Ludwig-Maximilians-Universität (2016). (Cited on page **31**)

[78] D. Amaro. *A Raman Laser System for Adiabatic Transfer of Polar Molecules*. Master's thesis, University of Coimbra (2013). (Cited on pages **32** and **34**)

[79] E. D. Black. *An introduction to Pound–Drever–Hall laser frequency stabilization*. Am. J. Phys. **69**, 79 (2001). (Cited on page **32**)

[80] D. R. Leibrandt, M. J. Thorpe, M. Notcutt, R. E. Drullinger, T. Rosenband, and J. C. Bergquist. *Spherical reference cavities for frequency stabilization of lasers in non-laboratory environments*. Opt. Express **19**, 3471 (2011). (Cited on page **32**)

[81] P. Budweiser. *Stabilitätsanalyse eines Ramanlasersystems*. Bachelor's thesis, Ludwig-Maximilians-Universität (2014). (Cited on page **32**)

[82] G. Kirchmair. *Frequency stabilization of a Titanium-Sapphire laser for precision spectroscopy on Calcium ions*. PhD thesis, Leopold Franzens University of Innsbruck (2006). (Cited on page **36**)

[83] M. W. Gempel, T. Hartmann, T. A. Schulze, K. K. Voges, A. Zenesini, and S. Ospelkaus. *Versatile electric fields for the manipulation of ultracold NaK molecules*. New J. Phys. **18**, 045017 (2016). (Cited on page **38**)

[84] M. Gröbner, P. Weinmann, F. Meinert, K. Lauber, E. Kirilov, and H.-C. Nägerl. *A new quantum gas apparatus for ultracold mixtures of K and Cs and KCs ground-state molecules*. J. Mod. Opt. **63**, 1829–1839 (2016). (Cited on page **38**)

[85] J. Shaw. *External Electric Fields: A New Tool for Controlling Ultracold Polar Molecules*. Bachelor's thesis, University of Colorado, Boulder (2015). (Cited on page **40**)

[86] M. Fleischhauer, A. Imamoglu, and J. Marangos. *Electromagnetically induced transparency: Optics in coherent media*. Rev. Mod. Phys. **77**, 633–673 (2005). (Cited on pages **45** and **51**)

[87] L. V. Hau, S. E. Harris, Z. Dutton, and C. H. Behroozi. *Light speed reduction to 17 metres per second in an ultracold atomic gas*. Nature **397**, 594–598 (1999). (Cited on page **45**)

[88] T. A. Schulze, I. I. Temelkov, M. W. Gempel, T. Hartmann, H. Knöckel, S. Ospelkaus, and E. Tiemann. *Multichannel modeling and two-photon coherent transfer paths in NaK*. Phys. Rev. A **88**, 023401 (2013). (Cited on page **46**)

[89] J. Martin, B. W. Shore, K. Bergmann, J. Martin, M. P. Fewell, and K. Bergmann. *Coherent population transfer in multilevel systems with magnetic sublevels. I. Numerical studies*. Phys. Rev. A **52**, 566–582 (1995). (Cited on page **46**)

[90] P. S. Żuchowski and J. M. Hutson. *Reactions of ultracold alkali-metal dimers*. Phys. Rev. A **81**, 060703 (2010). (Cited on page **58**)

[91] S. Ospelkaus, K.-K. Ni, D. Wang, M. H. G. de Miranda, B. Neyenhuis, G. Quemener, P. S. Julienne, J. L. Bohn, D. S. Jin, and J. Ye. *Quantum-State Controlled Chemical Reactions of Ultracold Potassium-Rubidium Molecules*. Science **327**, 853–857 (2010). (Cited on page **58**)

[92] M. H. G. de Miranda, A. Chotia, B. Neyenhuis, D. Wang, G. Quemener, S. Ospelkaus, J. L. Bohn, J. Ye, and D. S. Jin. *Controlling the quantum stereodynamics of ultracold bimolecular reactions*. Nat. Phys. **7**, 19 (2010). (Cited on pages **58** and **87**)

[93] J. Rui, H. Yang, L. Liu, D.-C. Zhang, Y.-X. Liu, J. Nan, Y.-A. Chen, B. Zhao, and J.-W. Pan. *Controlled state-to-state atom-exchange reaction in an ultracold atom–dimer mixture*. Nat. Phys. **13**, 699–703 (2017). (Cited on page **58**)

[94] M. Mayle, G. Quéméner, B. P. Ruzic, and J. L. Bohn. *Scattering of ultracold molecules in the highly resonant regime*. Phys. Rev. A **87**, 012709 (2013). (Cited on page **58**)

[95] G. Pupillo, A. Griessner, A. Micheli, M. Ortner, D. W. Wang, and P. Zoller. *Cold atoms and molecules in self-assembled dipolar lattices*. Phys. Rev. Lett. **100**, 2–5 (2008). (Cited on page **58**)

[96] R. Grimm, M. Weidemüller, and Y. B. Ovchinnikov. *Optical Dipole Traps for Neutral Atoms*. volume 42, pages 95–170. Academic Press (2000). ISBN 0120038420. (Cited on page **62**)

[97] J. Ye, H. J. Kimble, and H. Katori. *Quantum State Engineering and Precision Metrology Using State-Insensitive Light Traps*. Science **320**, 1734–1738 (2008). (Cited on page **62**)

[98] M. Li, A. Petrov, C. Makrides, E. Tiesinga, and S. Kotochigova. *Pendular trapping conditions for ultracold polar molecules enforced by external electric fields*. Phys. Rev. A **95**, 063422 (2017). (Cited on pages **63** and **65**)

[99] S. Kotochigova and D. DeMille. *Electric-field-dependent dynamic polarizability and state-insensitive conditions for optical trapping of diatomic polar molecules*. Phys. Rev. A **82**, 063421 (2010). (Cited on page **65**)

[100] B. Neyenhuis, B. Yan, S. A. Moses, J. P. Covey, A. Chotia, A. Petrov, S. Kotochigova, J. Ye, and D. S. Jin. *Anisotropic Polarizability of Ultracold Polar $^{40}K^{87}Rb$ Molecules*. Phys. Rev. Lett. **109**, 230403 (2012). (Cited on pages **65**, **68**, **76**, and **85**)

[101] Y. Deng and S. Yi. *Spinor Bose-Einstein condensates of rotating polar molecules*. Phys. Rev. A **92**, 033624 (2015). (Cited on page **65**)

[102] D. A. Steck. *Sodium D Line Data*. (Cited on page **66**)

[103] T. G. Tiecke. *Properties of Potassium*. (2011). (Cited on page **66**)

[104] S. Friebel, C. D'Andrea, J. Walz, M. Weitz, and T. W. Hänsch. *CO_2-laser optical lattice with cold rubidium atoms*. Phys. Rev. A **57**, R20–R23 (1998). (Cited on page **68**)

[105] H.-W. Li, S. Kar, and P. Jiang. *Calculations of dynamic dipole polarizabilities of Li and Na atoms in debye plasma using the model potential technique*. Int. J. Quantum Chem. **113**, 1493–1497 (2013). (Cited on page **69**)

[106] N. F. Ramsey. *A Molecular Beam Resonance Method with Separated Oscillating Fields*. Phys. Rev. **78**, 695–699 (1950). (Cited on page **74**)

[107] P. Händel. *Amplitude estimation using IEEE-STD-1057 three-parameter sine wave fit: Statistical distribution, bias and variance*. Measurement **43**, 766–770 (2010). (Cited on page **75**)

[108] E. L. Hahn. *Spin Echoes*. Phys. Rev. **80**, 580–594 (1950). (Cited on page **76**)

[109] A. P. Koller, J. Mundinger, M. L. Wall, and A. M. Rey. *Demagnetization dynamics of noninteracting trapped fermions*. Phys. Rev. A **92**, 033608 (2015). (Cited on page **78**)

[110] K. R. Hazzard, B. Gadway, M. Foss-Feig, B. Yan, S. A. Moses, J. P. Covey, N. Y. Yao, M. D. Lukin, J. Ye, D. S. Jin, and A. M. Rey. *Many-Body Dynamics of Dipolar Molecules in an Optical Lattice*. Phys. Rev. Lett. **113**, 195302 (2014). (Cited on pages **79** and **80**)

[111] C. Ospelkaus, S. Ospelkaus, L. Humbert, P. Ernst, K. Sengstock, and K. Bongs. *Ultracold heteronuclear molecules in a 3D optical lattice*. Phys. Rev. Lett. **97**, 120402 (2006). (Cited on page **86**)

[112] S. Eustice. *Ultracold NaK Molecules in a 3D Optical Lattice*. Master's thesis, Ludwig-Maximilians-Universität (2018). (Cited on page **86**)

[113] S. A. Moses, J. P. Covey, M. T. Miecnikowski, B. Yan, B. Gadway, J. Ye, and D. S. Jin. *Creation of a low-entropy quantum gas of polar molecules in an optical lattice*. Science **350**, 659–662 (2015). (Cited on page 86)

[114] H. P. Büchler, E. Demler, M. Lukin, A. Micheli, N. Prokof'ev, G. Pupillo, and P. Zoller. *Strongly correlated 2D quantum phases with cold polar molecules: Controlling the shape of the interaction potential*. Phys. Rev. Lett. **98**, 060404 (2007). (Cited on page 87)

[115] R. Vexiau, J.-M. Launay, and A. Simoni. *Quasi-1D ultracold rigid-rotor collisions: reactive and non-reactive cases*. arXiv. 1901.06164 (2019). (Cited on page 87)

[116] A. V. Gorshkov, P. Rabl, G. Pupillo, A. Micheli, P. Zoller, M. D. Lukin, and H. P. Büchler. *Suppression of inelastic collisions between polar molecules with a repulsive shield*. Phys. Rev. Lett. **101**, 073201 (2008). (Cited on page 87)

[117] M. P. Kwasigroch and N. R. Cooper. *Bose-Einstein condensation and many-body localization of rotational excitations of polar molecules following a microwave pulse*. Phys. Rev. A **90**, 021605 (2014). (Cited on page 87)

[118] M. P. Kwasigroch and N. R. Cooper. *Synchronization transition in dipole-coupled two-level systems with positional disorder*. Phys. Rev. A **96**, 053610 (2017). (Cited on page 87)

Danksagung

Meine Doktorarbeitszeit war ein Abenteuer, durch das mich viele Menschen begleitet haben. Bei ihnen möchte ich mich herzlich bedanken, denn erst durch sie wurde es zu einer unvergesslichen Erfahrung.

Allen voran - im übertragenen und wörtlichen Sinn, Letzteres besonders beim Wandern und Radfahren bei Gruppenausflügen - danke ich Immanuel Bloch. Vielen Dank für die Möglichkeit, diese Doktorarbeit anzufertigen! Diskussionen mit Dir haben den Fortgang des Experiments immer beflügelt, genauso wie die zahllosen Wissenschaftler, die Du einludst, die für unsere Gruppe oder das Institut Vorträge hielten und für Diskussionen bereit standen. Ich bin auch dankbar für die vielen spannenden Konferenzen, Workshops und Summer Schools, die ich besuchen und dadurch andere inspirierende Menschen und Orte kennen lernen konnte.

Ein großer Dank gebührt auch Christoph Gohle, dem Leiter des Polare Moleküle Labors bis zum Sommer 2018, der mir bis jetzt mit Rat und Tat zur Seite stand. Dein Spaß an der experimentellen Herausforderung sowie Deine Leidenschaft für jede noch so kleine Idee haben mich stets begeistert. Mit Deiner ruhigen Art und Engelsgeduld, aber auch Beharrlichkeit, hast Du mir viel beigebracht. I am also really glad that Xinyu, who joined our lab as a postdoc, took over Christoph's responsibilities as the Polar Molecules' group leader last summer. I firmly believe that you will lead our experiment into a great future with your ideas, diligence and passion! You were always a reliable, experienced colleague for me and your happiness and optimism helped me through the more difficult moments in my PhD journey.

Ich danke auch meinen ehemaligen Experimentkollegen, auf deren großartiger Vorarbeit diese Arbeit aufbaut: Tobias Schneider, der erster PostDoc des Experiments, hat mir zum Anfang meiner Doktorarbeitszeit geduldig vieles im Labor gezeigt. Von Deiner guten Organisation und Dokumentation von Kernstücken des Experiments zehren wir noch heute! Zhenkai Lu, the second PhD student of the experiment, impressively managed to not only be an experimentalist, but also a theorist throughout his PhD. Von Nikolaus Buchheim, dem ersten Doktorand und anschließend zweitem PostDoc des Experiment, habe ich gelernt, unsere „Maschine" zu bedienen. Du hast mir gezeigt, wie man Sequenzen programmiert und das Experiment wartet. Gemeinsam haben wir wahrscheinlich mindestens 50 durchgebrannte MOSFETs unseres Quadrupolspulen-Netzteils getauscht. Nikolaus, Zhenkai, Tobias and Christoph set

the incredible complex foundations for our double species machine. I find it extremely admirable that you never gave up, despite all the technical and physical challenges on our way to creating ground state molecules. Thanks for your support through to the writing of the first publication of our lab, although most of you had already left the institute at that point.

Zum Glück haben wir auch zwei fantastische neue Doktoranden, Roman Bause und Marcel Duda, bei denen das Experiment in besten Händen ist. Danke, Roman und Marcel, für Eure Beharrlichkeit, an genau unserem Experiment arbeiten zu wollen, für die tolle Arbeit, die ihr leistet, und für das Probelesen großer Teile dieser Arbeit.

Ich bedanke mich auch bei allen Kollegen anderer Experimente in der Gruppe, besonders bei Peter Schauß, Johannes Zeiher, Ahmed Omran, Katharina Kleinlein, Christian Schweizer, Luis Riegger und Nelson Darkwah Oppong, die nicht nur immer ein offenes Ohr für mich hatten, sondern irgendwie auch immer Zeit zum Kickern oder für TeX- und Python-Diskussionen fanden.

Danke Kristina Schuldt, Ildiko Kecskesi und Doreen Seidl! Ihr bewahrt unsere Gruppe nicht nur davor, im Chaos zu versinken, sondern organisiert auch noch die schönsten Veranstaltungen. Danke, dass ihr mich immer bestmöglich in jedweder Situation unterstützt habt!

Danke Anton Mayer, Karsten Förster und Olivia Mödl: Ohne Eure technische Unterstützung gäbe es keine polaren Moleküle. Ihr habt es immer geschafft, die verrücktesten und wahnsinnigsten unserer Anfragen in realisierbare CAD-Zeichnungen und Schaltpläne zu übersetzen, kaputte Gerätschaften, ohne die alles stillstehen würde, schnell zu reparieren und wertvolle Tipps zu allem vom Klempnern bis zum SMD Löten zu geben.

Außerdem bin ich sehr dankbar für die MPQ-Yogis, die sich jeden Mittwoch Mittag um Eva Neigenfind scharen. Ohne Euch hätte ich wohl nie herausgefunden, wie schön es ist, sich auf den Kopf zu stellen und die Welt ein Weilchen aus einer anderen Perspektive zu betrachten.

Vielen Dank auch Dir, Matthias Mader, meinem Institutskollegen aus der Laserspektroskopiegruppe. Danke für Deine wertvollen Ratschläge zur Verbesserung meines „alkaLiebe“ Science Slams und die vielen Auftrittsmöglichkeiten, die du mir eröffnet hast. Dank Dir konnte ich auch vielen Nicht-Wissenschaftlern unterhaltsam vom Moleküle-Machen berichten und meine Leidenschaft für unterhaltsame öffentliche Vorträge vertieft.

Ich danke meinen Kommilitoninnen seit dem ersten Tag, Julia Benedikter, Angela Burger und Isabella Graf. Unsere vielen Gespräche und die Erzählungen aus Euren Doktorarbeiten haben mir immer neue Perspektiven aufgezeigt.

Auch außerhalb der Wissenschaft hatte ich großartige Unterstützung durch meine Familie und Freunde. Ganz herzlich danke ich meinen Geschwistern Tilman, Friederike und Mareike, sowie meinen Eltern Sabine und Christoph Seeßelberg. Ihr habt mich immer unterstützt, mir gute Tipps gegeben und mir geholfen, wo ihr nur konntet, egal ob ihr gerade hier oder am anderen Ende der Welt wart. Ganz besonders möchte ich noch Heiner danken, der während diesem Abenteuer mein Mann wurde. Du hast mich selbst aus dem tiefsten Tief befreit, die schönsten Momente mit mir gefeiert oder hast mir einfach nur zugehört. Ich bin unendlich dankbar dafür und bin gespannt auf die nächsten Abenteuer, die das Leben für uns bereit hält.